Hysteresis Design of Magnetocaloric Materials-From Basic Mechanisms to Applications

Scheibel, Franziska; Gottschall, Tino; Taubel, Andreas et al.

(2018)

DOI: 10.1002/ente.201800264

Hysteresis Design of Magnetocaloric Materials—From Basic Mechanisms to Applications

Franziska Scheibel,*[a, b] Tino Gottschall,[a, c] Andreas Taubel,[a] Maximilian Fries,[a] Konstantin P. Skokov,[a] Alexandra Terwey,[b] Werner Keune,[b] Katharina Ollefs,[b] Heiko Wende,[b] Michael Farle,[b] Mehmet Acet,[b] Oliver Gutfleisch,[a] and Markus E. Gruner[b]

Magnetic refrigeration relies on a substantial entropy change in a magnetocaloric material when a magnetic field is applied. Such entropy changes are present at first-order magnetostructural transitions around a specific temperature at which the applied magnetic field induces a magnetostructural phase transition and causes a conventional or inverse magnetocaloric effect (MCE). First-order magnetostructural transitions show large effects, but involve transitional hysteresis, which is a loss source that hinders the reversibility of the adiabatic temperature change ΔT_{ad}. However, reversibility is required for the efficient operation of the heat pump. Thus, it is the mastering of that hysteresis that is the key challenge to advance magnetocaloric materials. We review the origin of the large MCE and of the hysteresis in the most promising first-order magnetocaloric materials such as Ni–Mn-based Heusler alloys, FeRh, $La(FeSi)_{13}$-based compounds, Mn_3GaC antiperovskites, and Fe_2P compounds. We discuss the microscopic contributions of the entropy change, the magnetic interactions, the effect of hysteresis on the reversible MCE, and the size- and time-dependence of the MCE at magnetostructural transitions.

1. Introduction

The model proposed by Isaak and van Vuuren in 2009 predicts that the worldwide energy demand of cooling devices will catch up with and soon outreach the demand of heating devices in the second half of this century.[1] This demonstrates clearly the demand of research on new cooling technologies for energy conservation and for the reduction of CO_2 and other greenhouse gas emissions. In this respect, magnetocaloric refrigeration technology is a promising alternative to conventional vapor-compression refrigeration due to its superior efficiency and the omittance of ozone depleting or hazardous chemicals and greenhouse gases.[2–5] Magnetic refrigeration is based on the magnetocaloric effect (MCE), which results in an emission or absorption of heat when a magnetocaloric material is exposed to a changing magnetic field. The process involves the transfer of entropy between the lattice and magnetic contributions to the total entropy, which remains constant under adiabatic conditions.[6] Brown demonstrated in 1976 the proof-of-concept for room-temperature magnetic refrigeration using Gd.[7] In 1997, Pecharsky and Gschneidner[8] observed a giant MCE in $Gd_5(Si_2Ge_2)$ near room temperature, which was a milestone in developing and designing magnetocaloric materials and prototype devices.[9–13] Magnetic refrigeration devices use a thermodynamic cycle consisting of four characteristic steps. In the first step, the magnetocaloric material undergoes an adiabatic, magnetic-field-induced transition, which leads to a temperature increase for a conventional magnetocaloric material. Next, the heat is transferred to the so-called hot reservoir of the device. In the third step, the adiabatic decrease of the magnetic field induces the reverse transition leading again to a temperature change. A sufficiently large reverse adiabatic temperature change enables heat transfer from the cold reservoir to the material (fourth step) and effectively reduces the temperature of the cold reservoir. The largest entropy and adiabatic temperature changes are observed in ma-

[a] Dr. F. Scheibel, Dr. T. Gottschall, A. Taubel, Dr. M. Fries, Dr. K. P. Skokov, Prof. Dr. O. Gutfleisch
Materials Science
Technische Universität Darmstadt
64287 Darmstadt (Germany)
E-mail: scheibel@fm.tu-darmstadt.de

[b] Dr. F. Scheibel, A. Terwey, Prof. Dr. W. Keune, Dr. K. Ollefs, Prof. Dr. H. Wende, Prof. Dr. M. Farle, Prof. Dr. M. Acet, Dr. M. E. Gruner
Faculty of Physics and Center for Nanointegration Duisburg-Essen (CENIDE)
University Duisburg-Essen
47057 Duisburg (Germany)

[c] Dr. T. Gottschall
Dresden High Magnetic Field Laboratory (HLD-EMFL)
Helmholtz-Zentrum Dresden-Rossendorf
01328 Dresden (Germany)

The ORCID identification number(s) for the author(s) of this article can be found under:
https://doi.org/10.1002/ente.201800264.

This publication is part of a Special Issue on "Ferroic Cooling". To view the complete issue, visit: http://dx.doi.org/10.1002/ente.v6.8.

terials undergoing first-order magnetostructural transitions, where substantial changes in the magnetic order and the lattice structure occur simultaneously.[8] In recent years, a number of promising magnetocaloric materials have been proposed and characterized with respect to the entropy change ΔS_T and the adiabatic temperature change ΔT_{ad}.[11] The drawback of the first-order magnetostructural transitions is, however, that they usually involve a transitional hysteresis. This is a significant source of efficiency losses that hinders the reversibility of the adiabatic temperature change, which is required for the efficient operation of the cooling cycle.[4,14–18] Therefore, hysteresis at first-order magnetostructural transitions is an issue that must be considered for developing useful magnetocaloric materials. So far, there are two common ways of dealing with hysteresis: either finding ways of eliminating it or keeping it as small as possible while maximizing the MCE, and thus accepting a certain amount of hysteresis-related losses. Either way, it is necessary to understand the causes of hysteresis and how they affect the functioning of magnetic refrigeration.

In this Review, we provide an overview of the properties of magnetostructural phase transitions with respect to the MCE. The transition takes place when the existing phase becomes energetically unfavorable compared to another phase, whereby the magnetic field of the refrigerator acts as a driving force stabilizing the high magnetization phase. The understanding of the transition process requires knowledge of the individual entropy contributions and entropy changes during the magnetostructural transition. This is the main theme of this Review, which presents studies under static and dynamic conditions at microscopic and mesoscopic scales. The results of the presented studies provide various approaches to understand the first-order transition and the origin of hysteresis. We set out to answer the following questions:

- Are there specific modifications of the electronic structure that link itinerant metamagnetism, large volume change and magnetoelastic contributions to the lattice entropy?
- How does disorder at the atomic length scale influence the magnetic properties?
- How does tailoring the phase transition towards a critical point between first- and second-order and the suppression of long-range ferromagnetic order influence thermal hysteresis and reversibility?
- Is it possible to improve the performance despite some remaining hysteresis by tailoring the microstructure?
- How does the size and shape of the grains of the material affect the magnetocaloric properties?
- How do stress and pressure modify the transition properties?
- Is it possible to distinguish the basic mechanisms for the nucleation of a first-order phase transformation and the phase boundary movement and to assess the time dependency of those two processes individually?
- How does the magnetocaloric effect depend on the magnetic-field sweep rate?
- How can this basic understanding be used to improve real devices?

Important magnetocaloric materials such as Ni–Mn-based Heusler alloys, FeRh, $La(Fe,Si)_{13}$-based compounds, Mn_3GaC antiperovskites, and Fe_2P-type compounds are presented in this Review.

Section 2 explains the correlation between the volume change, thermal hysteresis, and magnetic coupling. Furthermore, the microscopic contributions to the entropy change for promising, high-performance magnetocaloric materials are discussed. In Section 3, the magnetic interactions in magnetocaloric materials are studied with respect to thermal hysteresis. The effect of hysteresis on the reversible adiabatic temperature change is presented in Section 4 for different magnetocaloric materials. Sections 5 and 6 focus on the size-dependent and on dynamical effects of magnetocaloric materials with magnetostructural transitions. All phenomena are very important for the optimization of magnetocaloric materials in real cooling devices.

2. Disentangling the Microscopic Contributions to the Entropy Change

The magnetocaloric effect results in a temperature change ΔT_{ad}, upon altering an external parameter such as the applied magnetic field under adiabatic conditions, that is, without heat exchange with the surroundings. In first-order materials, ΔT_{ad} is limited by the shift dT_t/dH of the magnetostructural transition temperature T_t in a magnetic field H, or—if this shift is sufficiently large—by the heat capacity C_p of the material:[19–21]

$$\left|\Delta T_{ad}^{max}\right| = T \left|\Delta S_T^{max}\right| / C_p \quad (1)$$

Here, ΔS_T^{max} is the maximum isothermal entropy change. Their relation for a typical first-order material is shown in Figure 1 for two values of the magnetic field. Under reversible field cycling, the presence of thermal hysteresis reduces $|\Delta T_{ad}^{max}|$ further.[17] Without thermodynamic reversibility, free energy is acquired in a closed cycle, which will then be dissipated as heat to the surroundings and consequently reduces the efficiency of the refrigeration process.

The temperature T is the intensive thermodynamic variable forming a conjugate pair with the extensive quantity entropy. It must acquire the same value in the entire system under thermal equilibrium conditions. Therefore, to obtain a detailed understanding of the relevant microscopic prerequisites that characterize good magnetocaloric materials, it is more instructive to look at the extensive quantity related to the thermodynamic field T, which is the entropy S.

A quick reminder of the statistical definition of entropy shows immediately why it is so instructive. Entropy is proportional to the logarithm of the occupied phase space, which describes the number of possibilities for realizing a thermodynamic state. The degrees of freedom available to the system span the phase space, which are, for instance, dis-

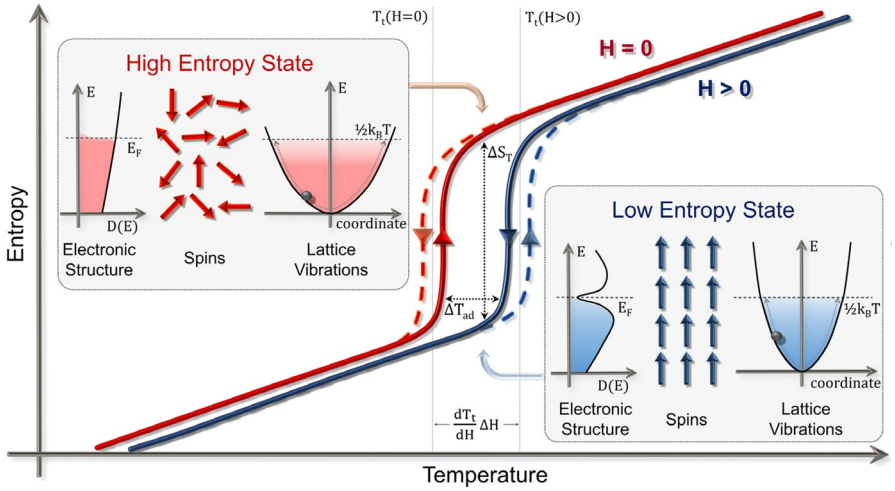

Figure 1. Schematic *T*–*S* diagram illustrating the magnetocaloric effect at a first-order transition. Application of a magnetic field *H* shifts the transformation temperature T_t to higher values. Applying the magnetic field isothermally in the intermediate temperature range between $T_t(H=0)$ and $T_t(H>0)$ leads to a decrease of ΔS_T in the total entropy, whereas an adiabatic field release decreases the temperature by ΔT_{ad}, which can be used for heat transport or cooling. Thermal hysteresis, indicated by the dashed lines, causes heat dissipation and reduces the maximum possible ΔT_{ad} in a cycling setup. The boxes depict basic characteristics of the respective high- and low-entropy states of the three relevant degrees of freedom. For the electronic entropy, these are, respectively, a high or low density of states at the Fermi level $D(E_F)$, for the magnetic entropy orientational disorder or order of the atomic moments, and for the lattice entropy, the presence of on-average softer or stiffer vibration.

placements and momenta connected to lattice vibrations. Therefore, if the microscopic variables can be considered independent of each other, S might simply be decomposed into the contributions from the relevant degrees of freedom,[19,22] usually denoted as electronic, magnetic, and lattice entropy:

$$S = S_{el} + S_{mag} + S_{lat} \tag{2}$$

At a field- or temperature-induced first-order transition, the Gibbs free energy in both phases must be in equilibrium and concomitant changes in all three partial contributions might add to the total entropy change ΔS_T.

In general, the contributions in Equation (2) cannot be considered independent and additional terms will occur.[19] However, we can estimate from this simplified model, to which extent each degree of freedom contributes to the magnetocaloric properties of a given material. This allows us to obtain a microscopic understanding of the magnetocaloric effect.

In the following we will review the individual contributions. At $T=0$, all electronic states up to the Femi level E_F are occupied (and empty above). At $T>0$, the electronic entropy S_{el} arises from the disorder in the occupation of the electronic bands in the solid due to thermal fluctuations. The corresponding expression involves the mixing of occupied and unoccupied states, weighted with the electronic density of states (DOS), $D(\varepsilon)$:

$$S_{el} = -k_B \int_{-\infty}^{\infty} D(\varepsilon)[(1-f(\varepsilon,T)\ln(1-f(\varepsilon,T)) + f(\varepsilon,T)\ln(f(\varepsilon,T))]\mathrm{d}\varepsilon \tag{3}$$

where $f(\varepsilon,T)=(\exp((\varepsilon-\mu)/k_BT)+1)^{-1}$ is the Fermi–Dirac distribution function, describing the probability that a state with energy ε is occupied at temperature T ($\mu \approx E_F$ is the chemical potential of the electrons). Therefore, the expression in the square brackets closely resembles the expression for the mixing entropy of a binary alloy. It is strongly peaked around E_F, thus, S_{el} is to a good approximation proportional to the DOS at the Fermi level, $D(E_F)$, and T:

$$S_{el} \approx \frac{\pi^2}{6} k_B D(E_F)\, T \tag{4}$$

Thus, we can expect considerable contributions from S_{el} to the magnetocaloric effect if strong features in the DOS right at E_F appear or disappear during a magnetostructural transition. This is for instance the case for $La(Fe_xSi_{1-x})_{13}$ or FeRh.[23] For second-order transitions, S_{el} can be considered to be unimportant. The density of states can be obtained from electronic structure calculations.[24–26] It can also be measured by photoemission spectroscopy (PES)[27] or absorption spectroscopy[28–31] for the occupied or unoccupied states, respectively, and by low-temperature calorimetry.[32] The lattice entropy S_{lat} is given by the velocity and amplitude of the atomic vibrations (phonons). The occupied phase space depends on the atomic volume but also on the elastic properties, as a softer material allows a larger amplitude. Both properties may change at a magnetostructural transition. This is expressed quantitatively in terms of the vibrational density of states (VDOS) $g(\varepsilon)$, which can be measured by inelastic neutron scattering[33,34] or nuclear resonant inelastic X-ray scattering.[23,25,35] VDOS and phonon dispersion relations have been calculated from first principles achieving ex-

cellent agreement with experimental data.[23,25,33,36–39] The expression for S_{lat} resembles S_{el}, where the expression in the parentheses takes into account the Bosonic character of the phonons through the Bose–Einstein distribution function $n(\varepsilon,T)=(\exp(\varepsilon/k_BT)-1)^{-1}$ for the occupation numbers, which becomes large for high T or small phonon energies ε:[22,40]

$$S_{lat} = 3\,k_B \int_0^\infty g(\varepsilon)[(1+n(\varepsilon,T))\ln(1+n(\varepsilon,T)) - n(\varepsilon,T)\ln(n(\varepsilon,T))]\,d\varepsilon \quad (5)$$

The change in lattice entropy can become the dominant contribution at first-order magnetostructural transitions, in particular in inverse magnetocaloric materials.[11,41] In metamagnetic Heusler alloys, where the low temperature phase is magnetically disordered, the significant caloric effect is essentially driven by the lattice degrees of freedom (see, e.g., Refs. [11,42,43]). Again, for second-order materials the contribution of the lattice to the transition can usually be neglected.

In magnetic materials, the electronic bands for spin-up and spin-down electrons are not occupied equally. This leads to a net magnetic moment at specific atomic sites. At very low temperatures, the magnetic moments associated with each site form a specific, for example, ferromagnetic order that minimizes the energy. Again, thermal fluctuations drive the magnetic moments out of their preferred orientation. This introduces disorder, which is reflected in an increased magnetic entropy S_{mag}.

At sufficiently low temperatures, close to the ordered state, the magnetic excitations are described by spin waves with certain wavelengths, propagation directions, and amplitudes. In analogy to phonons, one can express the entropy by an integral over the magnon density of states, which can be measured for example by neutron diffraction experiments. However, as the magnon–magnon interaction becomes relevant close to T_t, the single particle picture breaks down. Therefore, typical order–disorder transitions cannot be described in this way. These can only be assessed from theory (i.e., using a statistical model of magnetism such as the Heisenberg model), which can be parametrized empirically or from density functional theory (DFT) calculations.[44,45] For instance, considering a classical Heisenberg model (i.e., vector–spin model) one obtains in the mean-field approximation:[19]

$$S_{mag} = N_{mag}k_B\left[\ln\left(4\pi\frac{\sinh(x)}{x}\right) - x\coth(x) + 1\right] \quad (6)$$

with

$$x = \frac{\mu_0 m_0\,[\rho\eta_W M(T)+H]}{k_B T}$$

Here the parameter N_{mag} is the number of magnetic degrees of freedom, m_0 is the effective magnetic moment per magnetic degree of freedom, $M(T)$ the magnetization, ρ the density of the material, and η_W the molecular field constant. One has to bear in mind that Equation (6) can only give a first approximation for S_{mag}. For an accurate estimate, a statistical description beyond the mean-field approximation (e.g., by Monte Carlo methods) is needed to take into account the effect of spin fluctuations close to the transition temperature. Furthermore, the classical modeling breaks down at low temperatures, requiring a quantum mechanical description. Despite substantial numerical challenges, quantum Monte Carlo methods can be employed successfully in calculating the thermodynamic properties of realistic magnetic materials.[46,47] Another important complication is related to the simplification that localized spin models, such as the Heisenberg model used for deriving Equation (6), do not take into account the (partially) itinerant nature of magnetism, which we consider to be of particular importance in several magnetocaloric systems, as will be discussed further below. Deriving appropriate models describing these systems is thus an important open task for future research. Experimentally, ΔS_{mag} is usually estimated by subtracting all other entropy contributions from the total entropy change ΔS_T. Naturally, S_{mag} is deemed to be the most important entropy contribution for the magnetocaloric effect, as under normal circumstances only magnetic ordering is significantly affected by the application of a magnetic field. Assuming a magnetic field of 1 T and a magnetic moment of 1 μ_B this corresponds to 0.06 meV per spin, which is a very small energy as compared to the chemical potential of the electrons μ, which is for metals typically in the order of several eV. For second-order materials such as Gd, the magnetic entropy is the only relevant contribution.

In the literature, the magnetic entropy change is often used to denote the entropy change obtained after applying a magnetic field H,[48] measured, for instance, by calorimetry or by integrating $\partial M/\partial T$ over H.[49] However, this quantity is only equivalent with ΔS_{mag} in the case of second-order transitions.[15] In the case of a field-induced first-order transition, one rather obtains the total entropy change,[48] which includes the latent heat $T\Delta S_T$ involving all three contributions at constant field H plus a typically smaller magnetic-field-induced contribution from the final phase (e.g., Ref. [19]).

As we will discuss below, the three contributions to ΔS can have the same sign. This is the case for the magnetocaloric systems $La(Fe_xSi_{1-x})_{13}$ and FeRh.[23,25] However, one strictly cannot assume that the degrees of freedom are totally independent. For instance, the itinerant electron metamagnet $La(Fe_xSi_{1-x})_{13}$, is characterized by a competition of electronic states of Fe with different magnetic moments.[39,50–52] Due to this, magnetic disorder leads to an increased DOS at E_F, which improves the electronic screening of atomic displacements and thus softens the lattice.[53–55] The itinerant magnetism of Fe is also observed at the heart of the excellent caloric properties of MnFe(P,Si)-type materials.[56–59] In the following, we will discuss the impact of the specific microscopic degrees of freedom on the magnetocaloric properties for three classes of first-order materials, La–Fe–Si, Ni–Mn-based Heusler alloys, and FeRh.

2.1. $La(Fe_xSi_{1-x})_{13}$-based compounds

$La(Fe,Si)_{13}$-based compounds are prototypical materials with a conventional MCE and an isostructural first-order magnetic order–disorder transition. These materials exhibit a large MCE with an entropy change reaching values of 28 $J\,kg^{-1}\,K^{-1}$ and an adiabatic temperature change of up to 8 K in a magnetic field of 2 T.[24] After loading with hydrogen, the transition temperature can be finely tuned around ambient conditions (e.g., by substituting with Mn).[60,61] Together with the good availability of the elemental constituents, this makes $La(Fe,Si)_{13}$-based compounds one of the most interesting systems for refrigeration around room temperature.[4,17,21,62–64]

$La(Fe_xSi_{1-x})_{13}$ crystallizes in a rather complex cubic $NaZn_{13}$ ($Fm\bar{3}m$) structure with 112 atoms in the unit cell and two inequivalent Fe sites. Fe_I resides on 8b sites, located in the center of icosahedral cages formed by Fe^{II} on the 96i sites. These sites are shared with Si, which is required to stabilize the structure. La is positioned on the 8a sites[65–67] as depicted in Figure 2. For the composition $LaFe_{11.6}Si_{1.4}$, which we used for our experiments, the magnetostructural transition was observed to be approximately $T_t \approx 190$ K. In our samples we observed a narrow, but noticeable thermal hysteresis of 3 K.[25,35]

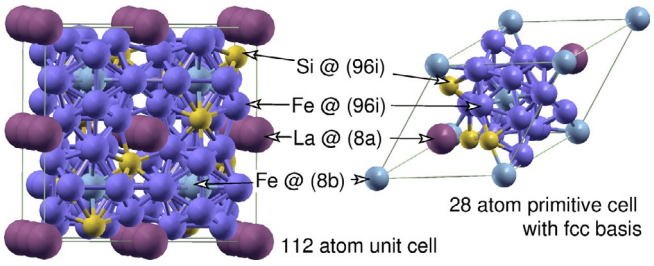

Figure 2. Unit cell (left) of $La(Fe_xSi_{1-x})_{13}$ with 112 atoms and with Cartesian basis compared to the primitive cell (right) with 28 atoms and fcc basis vectors. La (purple) occupies the 8a Wyckoff positions and Fe the 8b and 96i positions (bright and dark blue, respectively). Si is randomly distributed over the 96i sites (yellow). Both subfigures depict a partially ordered configuration for $LaFe_{11.5}Si_{1.5}$, which was used in the calculations as it retains rhombohedral symmetry. Figure adapted from Ref. [39] and Ref. [25], used with permission. Original Figure ©Wiley-VCH.

The transition from the ferromagnetic (FM) to the paramagnetic (PM) phase is accompanied by a significant volume decrease of $\approx 1\,\%$,[68] but the lattice symmetry remains the same. This leads to interface and volumetric stress during the transition, which is a potential cause of hysteresis. The large volume change is a consequence of the itinerant electron metamagnetism of La–Fe–Si.[50,69] It results from a competition of different magnetic states of Fe that are associated with different atomic volumes. Such states have been identified clearly in previous DFT calculations.[51,52] This is similar to Invar-type materials[70] such as $Fe_{65}Ni_{35}$ or Fe_3Pt, which also exhibit a free energy surface[71–73] with competing minima associated with different atomic volumes and magnetic moments, which are responsible for their marked thermal expansion anomalies.

According to the models described in the previous subsection, one would naturally expect that the decrease in volume should also lead to stiffer (higher frequency) phonons and consequently a decrease in entropy, which competes with the increase arising from magnetic disorder.[74,75] This is expressed in the conventional Grüneisen law, which links the volume change ΔV with the change in phonon energies ΔE:

$$\frac{\Delta E}{E} = -\bar{\gamma}\frac{\Delta V}{V} \tag{7}$$

In general, $\bar{\gamma}$ is a positive, material-specific constant, and we thus expect a blue-shift (increase) of the VDOS for $\Delta V < 0$, which corresponds to a smaller entropy according to Equation (5). Empirical calculations of the MCE of La–Fe–Si combine the conventional Grüneisen law with localized spin models to yield a good agreement with experiments.[74,76,77]

To obtain more detailed information on the subtle interplay of itinerant magnetism and lattice entropy we examined the VDOS at different temperatures above and below T_t. Using temperature-dependent nuclear resonant inelastic X-ray scattering (NRIXS) we measured the vibrational part of the entropy S_{lat}. At present, NRIXS measurements of the ^{57}Fe projected VDOS, $g(\varepsilon)$, have been performed at the Sector 3 beam line at the Advanced Photon Source at Argonne National Laboratory. By tuning the incident X-ray around the nuclear resonance of ^{57}Fe at 14.41 keV with a bandwidth as narrow as 1 meV,[78] the ^{57}Fe-projected VDOS can be extracted from the measured NRIXS spectra. The spectra were acquired in the PM state and in the FM state of a $LaFe_{11.6}Si_{1.4}$ powder sample, enriched with 10 % ^{57}Fe.

In addition, we performed complementary first-principles calculations of the vibrational density of states employing the VASP code.[79,80] The results of DFT calculations yield an element-resolved VDOS whereas the experiment only provides the ^{57}Fe-projected contribution. We chose the so-called direct method, in which the dynamical matrix of an extended system consisting of $2\times2\times2$ primitive cells is obtained by calculating the forces for all symmetry-inequivalent displacements of single ions. The Fourier transform and the subsequent eigenvalue problem were computed numerically with the PHON package.[81] All technical details can be found in Ref. [25,39]. The experimentally obtained VDOS is shown for both magnetic states in Figure 3. There are clear differences in the data above and below T_t. One of the most prominent feature is the suppression of the phonon peak at 28 meV in the PM state, which disappears directly above T_t. This phenomenon is a clear manifestation of the magnetoelastic coupling in this system. However, more important for the thermodynamic behavior is a concomitant red-shift of the entire VDOS. This behavior corresponds to a significant softening of the lattice and contradicts the conventional Grüneisen behavior expected from the volume change as expressed by Equation (7). Also the anomalous softening sets in directly above T_t.

A microscopic understanding of these effects can be obtained from electronic structure calculations. DFT is a $T=0$

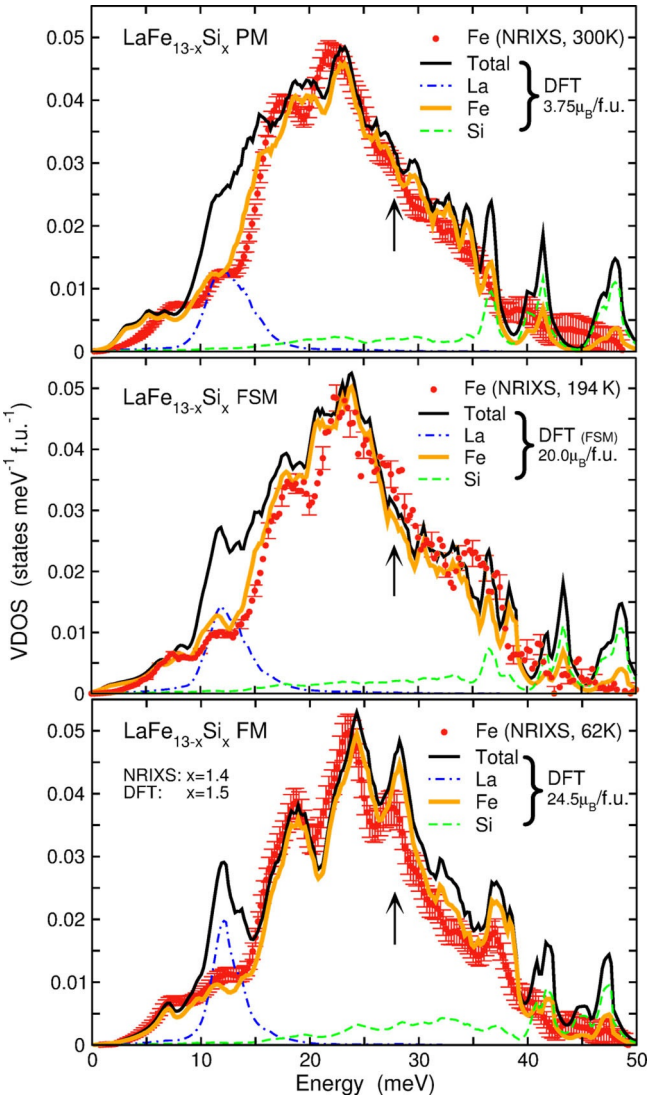

Figure 3. [57]Fe projected experimental VDOS (red circles with error bars) of $LaFe_{13-x}Si_x$ at three temperatures $T = 62$, 194, and 300 K with total (solid black lines) and element resolved DFT results (Fe: solid orange lines; Si: green dashed lines; La: blue dash-dotted lines). The bottom panel corresponds to the FM ground state. The top panel represents the PM phase characterized by spin disorder. The central panel represents a temperature closely above T_C. Here, the theoretical VDOS results from a ferromagnetic configuration (no spin disorder) with artificially reduced magnetic moments obtained within the FSM Scheme (see text). Figure adapted from Refs. [25, 39], used with permission. Original figures ©American Physical Society and Wiley-VCH.

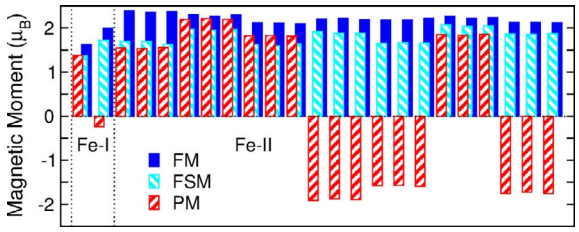

Figure 4. Fe magnetic moments of ordered (FM, blue), pseudo-disordered (PM, red) and ordered but longitudinally constrained (FSM, cyan) $LaFe_{11.5}Si_{1.5}$ calculated within the 28 atom primitive cell with rhombohedral symmetry. The individual site-resolved moments are grouped along the *x*-axis according to their Wyckoff position (data taken from Ref. [25, 39]).

theory, but for our purposes the different phases can be modeled by an ordered ("FM") configuration with the equilibrium magnetization of 24.5 μ_B per formula unit (f.u.) and a static pseudo-disordered configuration ("PM") with a small residual moment of 3.75 μ_B/f.u. to describe spin-disordered magnetic configurations found at elevated temperatures. The latter was obtained by constraining the total magnetization in the primitive cell successively to smaller values using the fixed spin-moment method,[82] which finally caused some of the collinear Fe-moments to flip around. The respective distribution of the Fe magnetic moments is depicted in Figure 4.

Apart from the presence of antiparallel moments, the absolute Fe moments are in the PM phase by almost 0.5 μ_B smaller than in the FM phase on average, which is a consequence of the partially itinerant character of the Fe moments. To distinguish between the consequences of spin disorder and itinerant magnetism we performed calculations of a FM configuration with artificially constrained magnetization (20 μ_B/f.u.). This leads to longitudinally constrained Fe moments, denoted in the following as "FSM" (fixed spin moment).

The Fe-projected vibrational density of states obtained from the ab initio calculations excellently matches the experimental data. This applies in particular for the FM phase (lower panel), where the agreement is almost quantitative. Both the FSM and PM configuration also yield very good agreement with the NRIXS data for $T > T_t$, including the disappearance of the peak at 28 meV and the red-shift of the entire VDOS. This proves that the characteristic changes in the VDOS are a direct consequence of the itinerant magnetism of Fe. The change of the Fe moments, in turn, is a consequence of the spin-disordered magnetic configurations found at elevated temperatures.

The entropy associated with the Fe-projected VDOS measured at various temperatures[25,35] according to Equation (5) is depicted in Figure 5. The red-shift in the VDOS observed at the magnetic order–disorder transition directly translates into an increase in lattice entropy alongside the magnetic entropy. The particularly fine resolution around T_t underlines the discontinuous nature of the changes in the elastic properties. The overall trend is confirmed by the DFT calculations, which in addition prove that the other elements do not provide a significant contribution to the entropy change.[25] Furthermore, the DFT calculations reveal that the electronic entropy also increases at the FM-to-PM transition (see Figure 5), and thus all contributions in Equation (2) have the same sign.

Though the absolute value of S_{el} is small compared to the other entropy contributions, the difference at T_t reaches notable values, which cannot be neglected. According to Equation (4), this is due to the significant increase of $D(E_F)$ in the PM compared to the FM phase. This can be traced back to the presence of a characteristic minimum in the electronic minority-spin DOS of the FM phase right at the Fermi

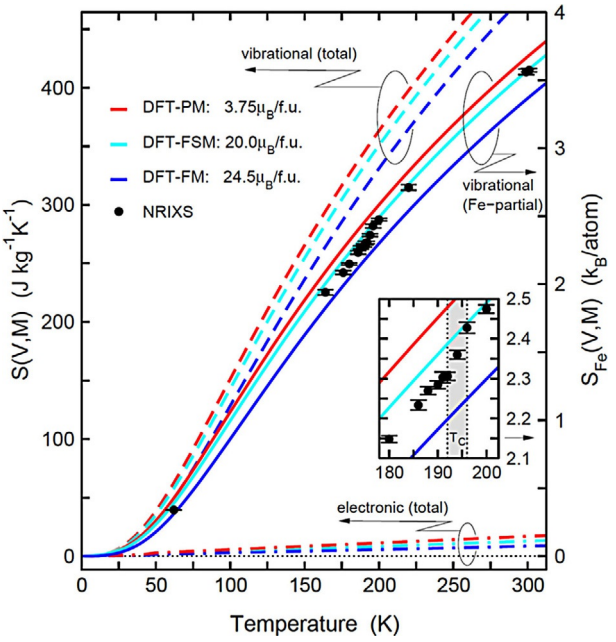

Figure 5. Total (left scale) and Fe contribution (right scale plus inset) to lattice and electronic entropy in the FM (blue lines) and PM phase (red lines) of La–Fe–Si. For a Si-content of $x = 1.5$ (DFT) the scales on both axes are equivalent. FSM denotes a configuration with constrained magnetization (FSM, cyan lines). The solid data points are obtained according to Equation (5) from the NRIXS VDOS $g(E)$, which has been corrected for a residual α-Fe contribution, at the respective experimental temperatures. Figure adapted from Ref. [25] with additional data from Ref. [25, 39], used with permission. Original figures ©American Physical Society.

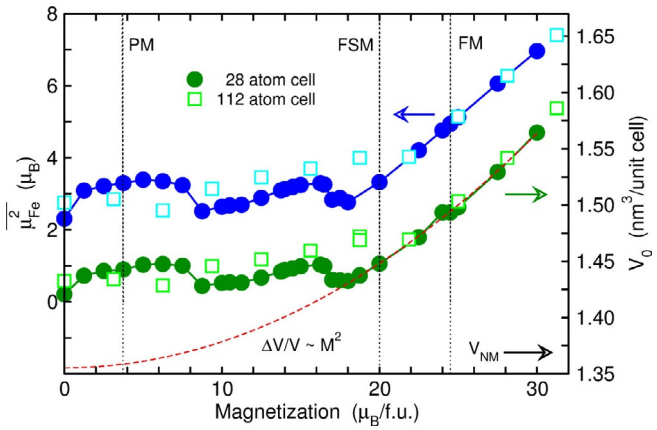

Figure 6. Optimized atomic volume V_0 (green circles and squares, right axis) and average square magnetic moment per site μ_{Fe}^2 (blue circles and cyan squares, left axis) as a function of constrained magnetization per formula unit calculated with the fixed spin moment procedure described in the text for two different simulation cells (open squares: 112 atoms unit cell, filled circles: 28 atoms primitive cell). The vertical lines denote the ferromagnetic (FM) ground state at $M = 24.5$ μ_B per formula unit (f.u.), the spin-configuration with $M = 3.75$ μ_B/f.u. used as model for the paramagnetic state (PM) and the ferromagnetic configuration with an artificially reduced moment of $M = 20$ μ_B/f.u. (FSM). The red dashed line in the center panel refers to a variation of the volume-magnetostriction $\omega \approx \Delta V/V$ which is expected to be proportional to the square of the magnetic moment. The arrow indicates the equilibrium volume of a non-spin-polarized (NM) state (data from Ref. [39]).

level,[25] which is shifted away and filled up due to the decreasing exchange splitting (reduced magnetic moment) caused by the spin disorder in the PM phase.[25,39]

The (dis-)appearance of marked features in the electronic DOS at the Fermi level also has also important consequences for the elastic properties of a material, as the presence of electron states at the highest occupied levels promotes the screening of perturbations arising from the displacement of the ions. This mechanism is discussed in the literature as adiabatic electron–phonon coupling and has been observed, for instance, in narrow-band-gap semiconductors and at phase transitions involving chemical ordering.[53–55] In La–Fe–Si, adiabatic electron–phonon coupling softens the PM phase despite the smaller volume compared to the FM phase and is thus the reason for the unexpected red-shift of the VDOS and the cooperative change of S_{lat} and S_{mag} at T_t. With $\Delta S_{lat,Fe} = 5$–7 J kg^{-1} K^{-1},[25,35] which we obtain from our NRIXS experiments, the change in the Fe projected vibrational entropy amounts to approximately 20–25 % of the total entropy change of 28 J kg^{-1} K^{-1} previously determined for this type of materials[24] and thus contributes to the superior magnetocaloric performance.

Although the huge volume change at T_t does not impair the favorable cooperation of all degrees of freedom in terms of the entropy change, it may lead to unfavorable volumetric stress or the formation of structural defects, which finally results in a broadened hysteresis and even disintegration of the material. Therefore, the origin of the volume change and its relation to the magnetocaloric effect is of primary interest. In the FM-ordered region, where the magnetization per cell M varies proportionally to the average magnetic moment per Fe atom μ_{Fe}, we also find that the relative volume change $\Delta V/V$ varies proportional to the square of M (Figure 6). This relation is part of the mean-field model description of Bean and Rodbell[83] and the Ginzburg–Landau models of volume magnetostriction.[72,84] For lower values of the magnetization $M < 20$ μ_B/f.u., the volume remains almost constant; thus we do not observe a characteristic variation of the volume V with M. The reason is that in this regime the Fe moments change their direction rather than their magnitude. We encounter a direct proportionality between the volume and the average square of the Fe-moments for all of our simulated configurations (Figure 6). This clearly shows that the change in magnitude of the absolute spin moment is responsible for the volume change at the transition, which results from the repopulation of the distinct magnetic states of Fe rather than fluctuations in the orientation of the spins, which determines $M(T)$ in localized spin. In the end, only two of the four distinct Fe states predicted by Kuz′min and Richter[51] turn out to be sufficiently close in energy to become thermodynamically relevant.[39]

The relation between magnetic order, magnitude of local Fe moments, and volume implies that one may reduce the volume change (and thus hysteresis) by avoiding a state with full ferromagnetic order, which allows the moment per atom to remain essentially constant. Figure 6 suggests that this is

effectively achieved by a comparatively small reduction in M of only 20 %, which can be accomplished by alloying with elements that couple antiferromagnetically, such as Mn.[26] However, as the volume change and softening of the lattice in the PM phase have the same origin, this strategy will sacrifice the beneficial contributions from ΔS_{el} and ΔS_{lat}. Nevertheless, a good compromise should be achieved by careful materials tuning.

In summary, La–Fe–Si owes its excellent magnetocaloric properties to the cooperative behavior of the magnetism, lattice, and electronic sub-systems. This also implies that the simple decomposition of the entropy in Equation (2) is not valid here, and additional coupling terms should be taken into account. Up to now a quantitative description of these contributions is still missing.

2.2. Ni–Mn–X(–Co) Heusler alloys

Heusler alloys of the Ni–Mn–X(–Co) (X = Al, Ga, In, Sb, Sn) family show a magnetostructural phase transition of first order. They experience, in contrast to La–Fe–Si alloys, an inverse magnetocaloric effect.[11,85–88] As a group of materials with a ferromagnetic shape memory effect, these Heusler systems show various technologically interesting properties such as a giant magnetoresistance, superelasticity, and also a magnetocaloric effect.[89,90] Ni–Mn–X(–Co) Heusler alloys undergo a martensitic phase transition from a cubic, high-temperature austenite phase to a tetragonal distorted or modulated monoclinic, low-temperature martensite phase. In the investigated Heusler compounds, the low-temperature martensite phase is PM above 200 K. On the contrary, the high-temperature austenite phase is FM and has a high magnetization. It implies that the magnetic ordering increases under heating and therefore the entropy change ΔS_{mag} must be negative. Instead, the entropy change related to the pure structural martensitic transition of the crystal lattice ΔS_{lat} is positive under heating. During the martensitic transition, one always observes the superposition of both ΔS_{mag} and ΔS_{lat}, but the lattice is dominant here. Kihara et al.[42] reported that the electronic contribution ΔS_{el} is negligibly small in Ni–Mn–In-based Heusler alloys. Therefore, one may consider that the magnetocaloric effect of the magnetostructural transition results mainly from changes in the entropy of the magnetic subsystem and the structural transformation of the lattice.

The martensitic transition temperature of Heusler alloys depends sensitively on the chemical composition. By fine-tuning the Mn/In ratio in $Ni_{50}Mn_{50-x}In_x$, the transition can be shifted over a large temperature interval. In Figure 7, the magnetization curves in 1 T of seven different compounds are plotted. The nominal composition was varied between $Ni_{50}Mn_{36}In_{14}$ with a transition of approximately 335 K and $Ni_{50}Mn_{35}In_{15}$, which transforms at 230 K. Consequently, a change of only 1 at % shifts the transition by approximately 100 K.[43] It was observed that the Curie temperature of the austenite is significantly less sensitive to the composition and hardly changes for the investigated compositions, which is in agreement with the literature.[91] This circumstance allows us

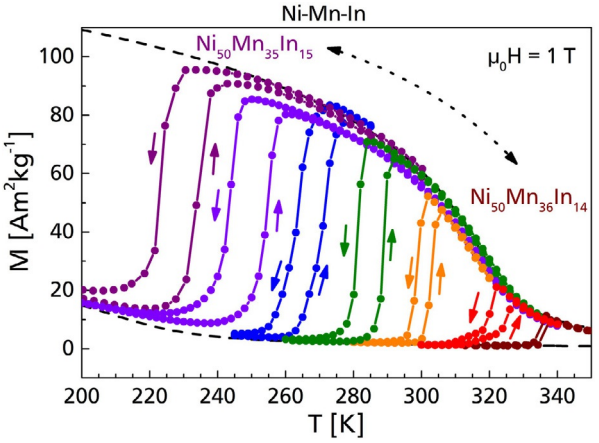

Figure 7. Comparison of the magnetic behaviors of various Ni–Mn–In samples in a magnetic field of 1 T. The dashed and the dotted lines are calculated curves of the saturation magnetization in 1 T of austenite and martensite. Figure adapted from Ref. [43], used with permission. Original Figure ©American Physical Society.

to describe the properties of the material family in a more general sense. Figure 7 suggests that the magnetization change during the martensitic transition is restricted to take place between the magnetization curves of pure martensite and austenite (black dashed curves). Based on this prerequisite, a more general description of the magnetocaloric properties will be derived.

As the variation of the chemical composition between the different alloys is small and we are sufficiently close to the Debye temperature, we assume in our phenomenological model that the difference in the lattice entropy ΔS_{lat} does not vary significantly in the temperature interval of interest is between 200 and 400 K. Above the austenitic Curie temperature T_t^A, the magnetic contribution to the entropy change is zero. We observed that the structural entropy change contribution ΔS_{lat} accounts for 46 $J\,kg^{-1}\,K^{-1}$ in the Ni–Mn–In and 55 $J\,kg^{-1}\,K^{-1}$ in the Ni–Mn–In–Co system.[43,92]

Based on this assumption, it can be concluded that the temperature dependence of the magnetocaloric effect is related to the contribution of the magnetic system S_{mag}, which we estimated in a mean-field Heisenberg model description according to Equation (6). The In atoms carry only a small induced magnetic moment and do not contribute to the magnetic entropy. In Ni_2MnGa, it was demonstrated that also the magnetic moment of Ni is induced.[93] Consequently, only the Mn and the Co moments were considered as magnetic degrees of freedom. In Equation (6), m_0 is calculated from the saturation magnetization at $T = 0$ K, determined from a $M(T)$ measurement at low temperature. The m_0 values for In Ni–Mn–In and Ni–Mn–In–Co were shown to be $4.38 \pm 0.1\ \mu_B$ and $4.02 \pm 0.08\ \mu_B$, respectively, by distributing the saturation magnetization to all magnetic degrees of freedom. The molecular field constant $\eta_W = 260$ is obtained in both systems from a fit to the model. Based on magnetization measurements of martensitic and austenitic samples in different magnetic fields H, $M(T)$ was simulated by using the approach of

Kuz′min,[10] which is illustrated in Figure 8a for 0 and 2 T for the Co-free system.

Figure 8b shows the magnetic entropies of both phases under 0 and 2 T, which are calculated by using the Heisenberg model from Equation (6). The small magnetization of

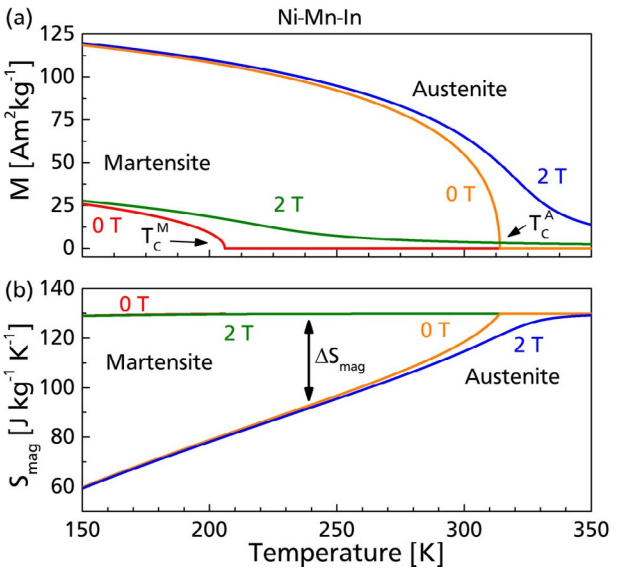

Figure 8. (a) Calculated magnetizations of martensite and austenite in 0 and 2 T. (b) Calculated magnetic entropy of the two phases as a function of temperature.

the martensite and especially its low Curie temperature T_C^M imply that the magnetic entropy of the martensite is already maximized above 200 K. This fact simplifies the determination of the magnetic contribution, which is the difference of the magnetic entropy of the two phases. For this reason, and assuming that the lattice contribution is constant, the temperature dependence of the entropy change of the transition is only related to the magnetization of the austenite phase:

$$\Delta S_t(T) = \Delta S_{lat} + \Delta S_{mag}^{A}(T) - S_{mag}^{M} \quad (8)$$

Many far-reaching consequences result from Equation (8). On the one hand, a large magnetization change depletes the available entropy change of the structural transition and is therefore parasitic. This increases until both contributions are equal and a transformation is no longer possible. On the other hand, a large magnetization change is essential to drive the magnetocaloric effect. This is because large isothermal entropy changes are only observable if the transition temperature can be shifted efficiently in a small magnetic field. But for this, the difference in the magnetization must be as large as possible. The contradiction that the change in magnetization is simultaneously both necessary and undesirable can be denoted as the "dilemma of inverse magnetocaloric materials".[43]

2.3 FeRh

From the above considerations, the question arises, whether the parasitic competition between the lattice and magnetic entropy is an unavoidable feature of inverse magnetocaloric materials. Indeed, exceptions are possible. As a magnetocaloric model system with one of the highest adiabatic temperature changes, FeRh provides essential insight into the dynamics of the magnetostructural phase transition.[3,11,94–96] In a narrow interval around the stoichiometric composition, FeRh forms an ordered B2 phase with a CsCl structure. The particular interest in this system results also from its unusual temperature-driven isostructural transition between a FM above $T_t \sim 350$ K and antiferromagnetic (AF) phase below.[97–100] This transition is accompanied by a large decrease in volume of ≈1 % and the complete loss of the Rh-moment in the G-type AF phase, which amounts to sizeable 1.0 μ_B in the FM state. The Fe moments, however, remain essentially constant across the transition with values of 3.2–3.3 μ_B. For a recent review on this system see Ref. [101]. Interestingly, due to the alternation of the Fe-moment on their simple-cubic sublattice in the G-type AF order, FeRh bears some resemblance to the $L2_1$ Heusler structure, if the differently oriented Fe-atoms were regarded as independent atomic species. First-principles studies predicted very recently an unstable mode in the AF phonon dispersion,[23,102,103] which could indicate the presence of another stable monoclinic or orthorhombic phase at very low temperatures.[23,103] At large tetragonal distortions, a competing tetragonal phase has also been predicted.[104] The presence of an unstable phonon mode in cubic FeRh bears similarity to the martensitic transformation in Ni–Mn-based Heusler compounds, where a soft phonon in the [110] direction in austenite[105–108] actively takes part in the transformation by supporting the formation of a favorable martensitic microstructure.[109–112] While non-cubic phases of ordered stoichiometric FeRh have not yet been reproduced experimentally, an orthorhombic phase has been stabilized in epitaxial films of disordered FeRh.[113]

FeRh has one of the highest adiabatic temperature changes of all known materials,[3,11,94–96,114,115] accompanied by a large entropy change observed at the transition.[116–119] Due to the large volume change, it is also accompanied by large elasto- and barocaloric effects.[120–122] Liu et al. reported a large reversible caloric effect in multi-stimulus magnetic–electric refrigeration cycle for an FeRh film grown epitaxially on $BaTiO_3$.[123]

To gather information on the lattice dynamics and vibrational thermodynamics, NRIXS measurements on B2-ordered FeRh thin films across the phase transition have been performed. The ^{57}Fe NRIXS experiments have been performed on FeRh thin film samples with the stoichiometries $Fe_{48}Rh_{52}$ and $Fe_{51}Rh_{49}$, both enriched with 95 % of ^{57}Fe. The samples were prepared by molecular beam epitaxy on MgO substrates with a thickness of 100 nm. The $Fe_{51}Rh_{49}$ sample undergoes no metamagnetic transition and is FM up to its Curie temperature, whereas $Fe_{48}Rh_{52}$ resides in a FM phase

at intermediate temperatures and becomes AF below $T=$ 380 K. The NRIXS experiments were performed at the beamline 3-ID at Argonne National Laboratory. The extracted ^{57}Fe-projected VDOS measured in the AF and FM states reveals four distinct peak positions as depicted in Figure 9.

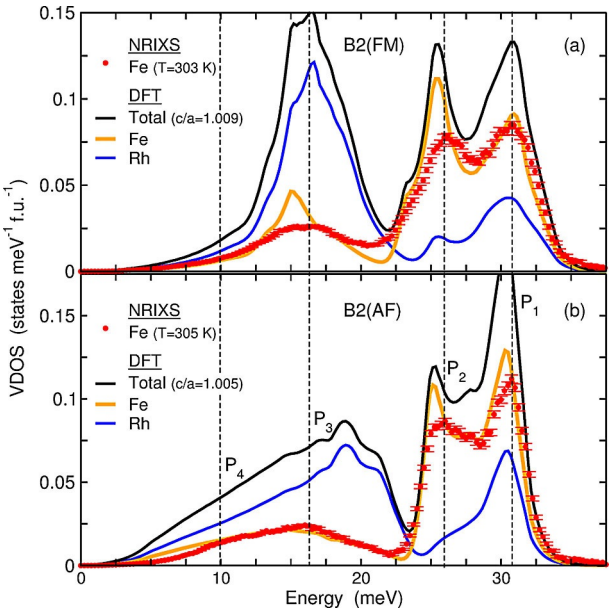

Figure 9. Experimental Fe projected VDOS (red) of (a) $Fe_{51}Rh_{49}$ (FM phase) and (b) $Fe_{48}Rh_{52}$ (AF phase) compared to the elementally resolved VDOS calculated by DFT for B2-structured FeRh. Figure adapted from Ref. [23].

The sample, which undergoes the metamagnetic transition ($Fe_{48}Rh_{52}$), shows the same behavior in the FM phase as the sample without a transition shown in Figure 9a.[23] There are four distinct phonon peaks visible: a sharp peak at high energies (P1) and a medium energy peak (P2) as well as two weakly pronounced and broadened low-energy peaks. Heating the sample starting from low temperatures results in significant changes of the shape of the VDOS. At 305 K, in the AF phase, the prominent phonon peak P1 first reduces its intensity, while P2 broadens, yet the shape of the VDOS remains the same.

In the FM state (Figure 9a), the shape of the phonon density of states is strongly affected by the magnetic ordering in the sample. As the transition from the AF to FM state is isostructural, similar to the previously discussed $La(Fe,Si)_{13}$ compounds, we would not expect large changes in the VDOS a priori. Indeed, the overall shape of the Fe-VDOS is much less affected compared to $La(Fe,Si)_{13}$. The change in magnetic order is accompanied by a reduction of the prominent phonon mode P1, which can be assigned together with P2 to transverse and longitudinal optical modes. A tiny reduction is also visible in the low-energy mode P4, which is an acoustic mode as well as P3. The small red-shift is in accordance with the structural thermal expansion upon heating. In addition to the experiments, complementary first-principles calculations have been performed to understand the coupling between the lattice dynamics and magnetism. The corresponding element-resolved DFT calculations show good agreement between the experimental data and theory. It shows, however, that the changes in the VDOS across the transition are substantial for Rh, which is not accessible to NRIXS, and we consequently expect Rh to play the dominant role with respect to the vibrational contribution to the entropy change. The magnetoelastic coupling corresponds here to the change in the magnetic state of Rh—whereas the Fe moments remain essentially localized. The comparison of the experimental VDOS at $T=64$ K with calculations of the predicted orthorhombic or monoclinic low-temperature phase also yields no indication for a further phase transition down to this temperature.[23]

In earlier years of this field, the metamagnetic transition has been ascribed to extraordinarily large differences in low-temperature specific heat between the AF and FM phases. Tu et al.[124] argued that a change in entropy of band electrons is solely responsible for the transition, but this view fails to explain the transition in the case of the admixture of 5% Ir to FeRh, where the relation of the specific heats becomes reversed.[116,125,126] A more recent attempt to disentangle the different contributions to the entropy change from experiments has been undertaken by Cooke et al.[127] based on their seminal measurements of the specific heat in FM and AF thin FeRh films. They concluded that the inverse transition is driven by the huge magnetic entropy, whereas the lattice entropy is counteracting, which is precisely the opposite picture of that for the Heusler systems discussed in Section 2.2. However, due to the lack of suitable alternatives, the decomposition of entropy and specific heat in the spirit of Equation (2) was based on a simple Debye model for the lattice degrees of freedom fitted to elastic constants, which might not be accurate enough for this purpose.

Previous first-principles studies concentrated on the electronic part and total energy due to magnetic excitations.[128,129] Encouraged by the good agreement of the Fe-projected VDOS between experiment and theory in both phases of FeRh, we therefore attempted a similar approach to that presented for La–Fe–Si in Section 2.1. Concerning the lattice degrees of freedom, we discovered significant changes in the Rh-projected VDOS with respect to the magnetic state and lattice distortions,[23] whereas only information related to Fe is available from NRIXS. This can be expected, as in FeRh the Fe-moments present a rather localized character, whereas the spin density distribution cancels at the Rh site in the AF phase[130] leading to a large change in the Rh moment. Therefore, for the following, we rely upon our thermodynamic data for cubic bulk FeRh obtained within the quasi-harmonic approximation from first-principles,[23,108] taking into account thermal expansion and the volume change at the transition. The respective lattice and electronic contributions to the entropy change are shown in Figure 10, together with ΔS_{mag} obtained from the magnon density of states calculated for both, AF and FM phases.[131] When approaching the Curie temperature, the single-particle picture breaks down and the presence of excited spin waves might alter the magnon density of states significantly (magnon–

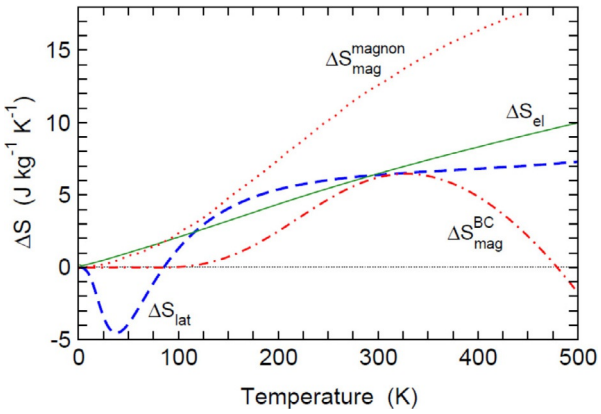

Figure 10. Disentangled entropy contributions ΔS_{mag} (thin green line) and ΔS_{lat} (blue dashed line) from our quasiharmonic calculations[23] in comparison with the entropy change obtained from two different magnetic models (red lines): (i) the difference of the entropy of magnon excitations as calculated from first-principles by Gu and Antropov[131] ΔG_{mag}^{magnon} (dotted line) and (ii) the respective entropy difference obtained from a Blume–Capel model ΔG_{mag}^{BC} [132] (dash-dotted line) considering spin-flip and longitudinal excitations. In the transition region, all entropy contributions act cooperatively (have the same sign) and are essentially of the same magnitude.

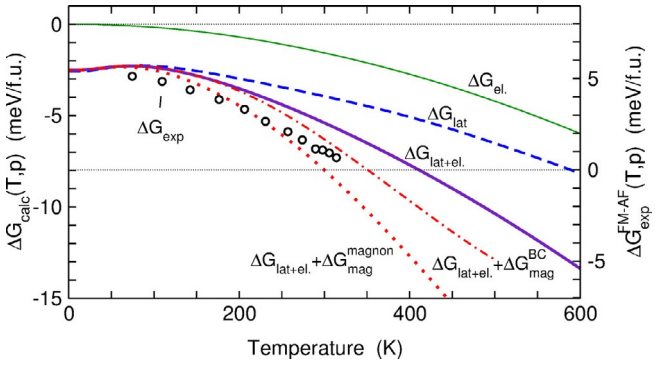

Figure 11. Decomposed Gibbs free energy obtained from our quasiharmonic calculations $\Delta G_{el.}$ (thin green line), ΔG_{lat} (blue dashed line), and ΔG_{lat+el} (thick purple line) in combination with the free energy contributions of two different magnetic models (red lines): (i) the difference of the free energy of magnon excitations as calculated from first-principles by Gu and Antropov[131] ΔG_{mag}^{magnon} (dotted line) and (ii) the respective free energy difference obtained from a Blume–Capel model ΔG_{mag}^{BC} [132] (dash-dotted line) considering spin-flip and longitudinal excitations. Both descriptions of magnetism lead to a reasonable agreement with the experimental data ΔG_{exp} of Ponomarev[135] (black circles, right axis). As the AF–FM energy difference turned out to be very sensitive to details of the technical setup,[23,102] defects, and deviation from stoichiometry,[136,137] the left and right axes are aligned such that the extrapolations of experimental and theoretical free energy differences coincide at $T=0$ (same scaling on both axes). Figure adapted from Ref. [23], used with permission. Original Figure ©American Physical Society.

magnon interaction). Therefore, we present as a complementary estimate ΔS_{mag} obtained from a phenomenologically parameterized spin-1 Ising (Blume–Capel) model,[132] which allows longitudinal and spin-flip excitations and was evaluated at finite temperatures by classical Monte Carlo simulations. The essence of Figure 10 is that although all contributions to the entropy change exhibit a different temperature dependence, they all acquire the same sign, similar to the conventional magnetocaloric La–Fe–Si with a comparable magnitude at the metamagnetic transition. In summary, we obtain $\Delta S_{el}+\Delta S_{lat}+\Delta S_{mag}^{BC}\approx 20\,J\,kg^{-1}\,K^{-1}$ which is close to the total entropy change reported from experiments, ranging from 12 to 19 $J\,kg^{-1}\,K^{-1}$.[94,96,116,121,133,134] Also, the temperature-dependent total free energy difference ΔG from ab initio thermodynamics in combination with both of the above mentioned magnetic models (see Figure 11) reproduces the experimental data of Ponomarev[135] and yields a reasonable estimate of the metamagnetic transition temperature, which further validates our analysis of the role of the particular degrees of freedom.

Rh is scarce and expensive. For this reason, this alloy does not qualify as a candidate for mass-market applications. But it demonstrates that an excellent performance can be achieved even with inverse magnetocaloric materials. One important reason is the ordered AF ground state, which can possess a lower entropy compared to the FM at the metamagnetic transition and allows for the cooperative action of all degrees of freedom as in $La(Fe,Si)_{13}$. Therefore, FeRh can serve as a design model for other classes of inverse magnetocaloric materials, in particular the Heusler alloys or Mn_3GaC-based antiperovskites. Here one may look out for systems with a stable AF or FM order over the entire stability range of the martensite by specifically shaping the magnetic interactions between the elements.

3. Magnetic Interactions in Magnetocaloric Materials

As there is no direct access to the magnetic part of the total entropy, it is important to take a closer look at the microscopic magnetic correlations in magnetocaloric materials. The magnetostructural phase transitions and thereby the behavior of the thermal hysteresis and hence the performance of these materials strongly depends on the magnetic interactions.

3.1. Ni–Mn–X(–Co) Heusler alloys

In the following we will demonstrate how element specific studies, ferromagnetic resonance, and bandstructure calculations can be used to achieve a microscopic understanding of the relevant interactions in Heusler systems on an atomic length scale. As introduced in Section 2, Heusler alloys undergo a phase transition from high-temperature austenite to a low-temperature martensite phase. The symmetry reduction during this martensitic phase transition strongly affects the magnetic correlations in the system by changing the interatomic distances and the magnetic exchange. While in the austenite phase interactions are predominately FM and lead to a high spontaneous magnetization, the interactions are more complex in the martensite.[91,138–142] To gather information on the magnetic coupling in the martensite phase, a combined approach of ferromagnetic resonance (FMR) and X-ray absorption near edge structure (XANES) as well as X-ray magnetic circular dichroism (XMCD) measurements was used.[143] X-ray absorption measurements were performed at

the ID12 beamline at the European Synchrotron Radiation Facility in Grenoble, France. The X-ray absorption spectra were recorded using a cryostat and an applied magnetic field of ±1.6 T in both structural phases. The results are shown in Figure 12. From the XANES at the K-edges of Mn, Co (not shown here), and Ni in the martensite (T = 150 K, black lines) and austenite (T = 305 K, red lines) phase, it is apparent that the magneto-structural phase transition strongly alters the local surroundings of all three elements. As the rising edge remains unchanged, a change in the local electronic surroundings can be neglected. From the XMCD signal, the orbital polarization can be extracted as it reflects the orbital component of the density of states of p- and d-like symmetry considering electric dipole and electric quadrupole transitions. In the high-temperature austenite phase, the XMCD spectra for all three elements show the same sign, indicating a parallel alignment. Hence, in the cubic austenite phase, we see FM behavior. After the phase transition in the low-temperature phase, the XMCD signal at the Mn K-edge vanishes, whereas Co and Ni exhibit a reduced XMCD signal and therefore a small magnetic moment in the tetragonal distorted martensite phase. Figure 13 depicts the FMR measurements in both of the magnetostructural phases. The FMR spectrum at low temperature (T = 5.2 K) in the martensite phase shows two defined resonances. The peak occurring at a low field value of 240 mT can be attributed to FM interactions within the sample, whereas the resonance with smaller intensity at 1200 mT can be attributed to AF interactions. The weak AF coupling leads to an increased spin frustration at very low temperatures. With increasing temperature, the FMR line intensity decreases until the line vanishes. This behavior can be interpreted in the following way: Below 50 K there is a mixed phase of AF and FM. Heating the sample through the phase transition changes the FMR spectra significantly. Only one resonance line is visible, which is shifted down to 130 mT with a very low intensity. This resonance field deviates from the paramagnetic value (dotted red line) and illustrates that FM interactions are present in this Ni–Mn–In–Co material, also in the martensite phase with low magnetization and they can be attributed to Ni (and Co).

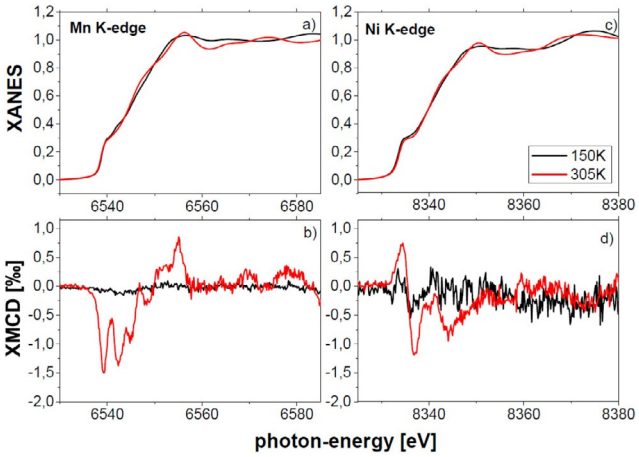

Figure 12. XANES (top) and XMCD (bottom) spectra for a $Ni_{45}Mn_{37}In_{13}Co_5$ powder sample measured at the Mn (a, b) and Ni (c, d) K-edge, in the martensite state at T_{exp} = 150 K (black) and in the austenite state at T_{exp} = 305 K (red). Figure adapted from Ref. [143], used with permission. Original Figure ©Wiley-VCH.

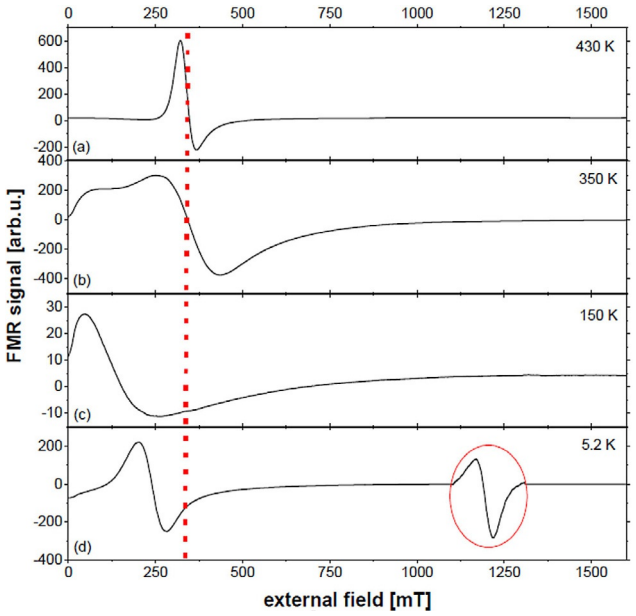

Figure 13. (a–d) FMR spectra of powder $Ni_{45}Mn_{37}In_{13}Co_5$ in the high-temperature austenite phase at 430 K (a) and 305 K (b) and in the low-temperature martensite phase at 150 K (c) and 5.2 K (d) taken in external field sweeps from 1.6 T to 0 T. The (red) dotted line in each spectrum represents the isotropic value and the signal at higher fields (red circle) is magnified by a factor of 100 for visualization. Figure adapted from Ref. [143], used with permission. Original Figure ©Wiley-VCH.

While it is difficult to disentangle a change in local magnetic moment from magnetic disorder or non-parallel alignment experimentally, element- and site-resolved magnetic exchange constants can be calculated from first principles, for instance by using the Korringa–Kohn–Rostoker (KKR) method in combination with the so-called Liechtenstein approach.[144] Implementations such as SPR-KKR[145,146] offer the possibility to treat off-stoichiometric compositions and disorder efficiently without large supercells in the framework of the coherent-potential approximation (CPA) (see, e.g., Ref. [147]). This is convenient as the experimental synthesis and annealing procedures involve in general off-stoichiometric compositions and partial chemical disorder.

Using KKR-CPA, the magnetic exchange constants for several Heusler compounds have been calculated over the years, with a particular focus on Ni–Mn–In and Ni–Mn–Ga-based systems.[44,148–154] Also quaternary systems as Ni–Mn–In–Co have been investigated.[155–159] The In- and Ga-based compounds are isoelectronic and show similar behaviors at the same compositions. Therefore, we will discuss in the following the exchange parameters of off-stoichiometric Heusler compounds, which we calculated recently for $Ni_{43}Co_9Mn_{27}Ga_{21}$[160] under the assumption of additional partial disorder between the X- and Y-sublattices in the $L2_1$ pro-

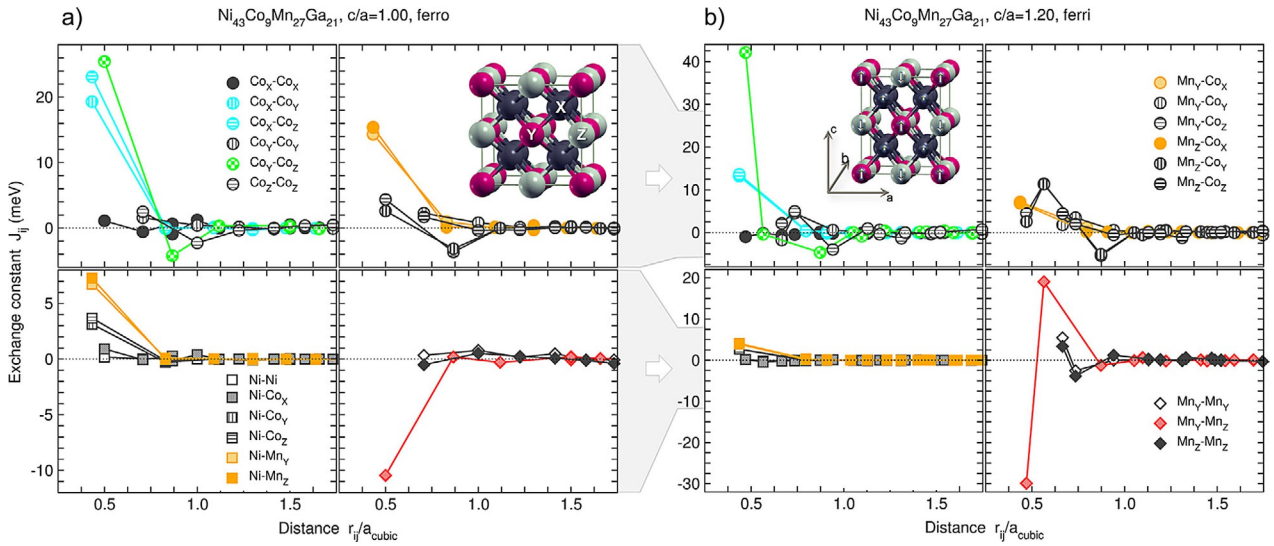

Figure 14. Calculated magnetic interaction parameters J_{ij} for a Heisenberg model of an off-stoichiometric $Ni_{43}Co_9Mn_{27}Ga_{21}$ Heusler compound in the cubic $L2_1$ austenite (a) and tetragonal $L1_0$ martensite phase (b) with $c/a = 1.2$. Both structures are subject to additional site disorder. The data points refer to particular exchange constants between different magnetic atoms *i* and *j* characterized by their distance r_{ij}, which is specified relative to the lattice constant of cubic austenite ($a_{cubic} = 5.80$ Å). Positive values denote ferromagnetic interactions, and negative values a preferred antiferromagnetic alignment of the interacting spins. Their values depend decisively on the site on which the elements are located. These are indicated by the indices according to the $L2_1$ Heusler formula unit X_2YZ, see inset in the upper right panel of (a): X is the preferred site of Ni and Co, Y of Mn, and Z of Ga and Mn. The exchange constants for austenite were calculated from a ferromagnetic reference and for martensite from a ferrimagnetic reference configuration, which is depicted in the upper left panel of (b), in accordance with the experimental findings. Particular interactions discussed in the text are highlighted by colors. Please note the change in scale on the ordinate between (a) and (b). Figure adapted from Ref. [160], used with permission. ©Institute of Physics.

totype structure X_2YZ, which are predominately occupied by Mn and Ga. In addition, the Co-rich composition, which forces Co to occupy Y- and Z-sites as well, leads to a variety of additional possibilities for the magnetic exchange interaction pairs present in the system.

All combinations are shown in Figure 14 (except for Ga, which has negligible magnetic contributions), plotted as a function of the interatomic distance between the interacting atoms.

In agreement with previous reports,[44,153,154,161] we observe significant short-ranged FM interactions between neighboring Ni and Mn atoms in the austenite phase (Figure 14a, lower left panel). These are mainly responsible for the prevailing FM order in the austenite. Due to the decrease of the induced moment of Ni, they are significantly reduced in the martensite (Figure 14b, lower left panel) which contributes to the early breakdown of magnetic order in this phase. In contrast, according to predictions based on the generalized Bethe–Slater curve,[140,162,163] interactions between nearest-neighbor Mn_Y–Mn_Z pairs support an AF arrangement already in the austenite (lower right panel in Figure 14a), competing with the indirect FM coupling over the Ni-sites in the martensite, which is in perfect agreement with previous studies.[44,155,156] In the tetragonal case, this interaction splits up according to the reduced symmetry, exhibiting an extreme directional dependence with values of approximately +19 meV along the elongated *c*-axis in contrast to −30 meV along the *a*- and *b*-axes.

Adding Co to the system essentially stabilizes the FM character of the spin configuration in the cubic austenite. The majority of Co atoms located on the Ni-site establishes FM interaction with Mn (upper right panel of Figure 14a), which is larger than the Mn–Ni exchange. Considerable interactions are also found among the Co atoms on all sites and with Ni, whereas Ni–Ni interactions are negligible. Similar mechanisms stabilizing FM order have already been pointed out in other first-principles studies of quaternary Ni–Mn–(Al, Ga, In)–Co Heusler alloys.[155–158,164] In the martensite phase, the interactions involving Co_X show a very similar reduction upon the transition to martensite compared to Ni, which is also located on the X-sites. Excess Co atoms on the Y- and Z-sites, however, follow a similar pattern to Mn after the transition. Here, the Co_Y–Co_Z interaction splits up into a small AF interaction of −0.4 meV along the *c*-axis versus an intriguingly large FM contribution of +42 meV along *a* and *b*. Thus a small fraction of Co atoms on the X- and Y-sites, which is likely to be present due to incomplete order, might induce a considerable perturbation of any non-ferromagnetic spin distribution.

This shows that the magnetic properties are not solely determined by the mere composition of the system—as captured by the valence electron ration *e*/*a*—but also essentially by the distinct lattice sites on which the elements are residing. To some extent this can be controlled by partial disorder and by forcing excess Co to the Y- and Z-sites. As discussed in Ref. [160], the same is true for Mn forced to the X-sites (for instance by adjusting the composition as in $Ni_{45}Mn_{32}Ni_{23}$). In this case, Mn partially acquires the similar minority spin density of states to that of Ni, exhibiting a predominately itinerant behavior, whereas Co atoms placed in

the same configurational environment as the Mn atoms also acquire magnetic properties similar to Mn. Therefore, we conclude that compositional disorder is a fundamental factor for the magnetic behavior of a Ni–Mn-based Heusler system, which can alter the magnetic behavior in a fashion that is not entirely straightforward. This is particularly the case for Co-doped metamagnetic Heusler alloys, which are of primary interest for magnetocaloric applications.

3.2. Mn_3GaC-based antiperovskites

Mn-based antiperovskites with the general formula Mn_3AX, (A: Al, Zn, Ga, Ge, Sn, In) and (X: C, N, B), show a large variety of magnetic ordering configurations and magnetostructural transitions with narrow hysteresis properties.[165–170] These materials crystallize in the Pm3m space group with cubic symmetry. Mn is located at the face-centered positions, the A atoms reside on the cube corners and the X atoms occupy the octahedral sites at the cube center. Mn_3GaC has been particularly investigated due to its narrow hysteresis at the first-order transition. It undergoes a first-order AF to FM transition at 167 K, which is accompanied by a volume contraction of about 0.5 % without a detectable change in the crystal structure.[166,169] Mn_3GaC exhibits an inverse MCE in the vicinity of the first-order transition. At 250 K, Mn_3GaC shows a second-order FM-to-PM transition with a conventional MCE. Figure 15a shows the temperature-dependent magnetization under an external field of 50 mT for zero-field-cooled (ZFC) and field-cooled (FC) measurements. Applying a magnetic field stabilizes the FM phase and shifts the first-order transition towards lower temperatures. The large shift ($-4.4\,K\,T^{-1}$) of the transition and the narrow thermal hysteresis (4 K) enable a full transformation from the AF to the FM state even in 2 T and lead to a large magnetic entropy change ($\Delta S_T = 15\,J\,kg^{-1}\,K^{-1}$).[41,168,171] The narrow thermal hysteresis can be further reduced by substituting C by N, whereas the hysteresis disappears for $Mn_3GaC_{0.85}N_{0.15}$.[167,172] The temperature dependence of the magnetization of $Mn_3GaC_{0.85}N_{0.15}$ is shown in Figure 15b. At 185 K, the first- and second-order transitions coincide and the alloy transforms from an AF state to an enhanced paramagnetic state (EPM) without long-range FM ordering. Applying an external magnetic field leads, as for Mn_3GaC, to a shift of the transition temperature towards lower temperatures.[172] Neutron depolarization studies of Mn_3GaC and $Mn_3GaC_{0.85}N_{0.15}$ provide information on the presence of long-range FM ordering and the presence of FM domains.[173] Therefore, the flipping ratio R_f of the transmitted neutrons is measured. R_f is calculated by the ratio of the spin-up to spin-down neutrons. For zero net magnetization of the sample R_f is not affected, whereas the presence of FM domains, however, leads to a torque of the neutron spin which results in a drop of R_f. Figure 15c,d shows R_f of the Mn_3GaC and $Mn_3GaC_{0.85}N_{0.15}$ sample as a function of temperature. In the AF state below 167 K, Mn_3GaC shows a constant R_f. Above the first-order transition, the sample is in a FM state and a drop in R_f is observed. At 250 K, Mn_3GaC undergoes the second-order FM-to-PM transition and R_f increases rapidly due to the absence of FM domains. For $Mn_3GaC_{0.85}N_{0.15}$, a constant R_f is observed over the entire temperature range. This shows that no FM domains are developed at the transition temperature although a tendency towards FM ordering is observed by the increase of $M(T)$ in the vicinity of the transition. To determine the magnetic coupling in the vicinity of the first-order transition in more detail, neutron polarization analyses have been performed.[173] The measurements show a presence of FM correlations at high temperatures in both samples. However, no long-range FM ordering was observed in $Mn_3GaC_{0.85}N_{0.15}$. The MCE in $Mn_3GaC_{0.85}N_{0.15}$ is most probably related to induced ferromagnetism by applying a magnetic field. However, the absence of thermal hysteresis raises the question of the extent to which the presence of FM domains contributes to the hysteresis. In this case, coinciding first- and second-order transition in materials with inverse MCE can offer a possibility to minimize or even eliminate the hysteresis.

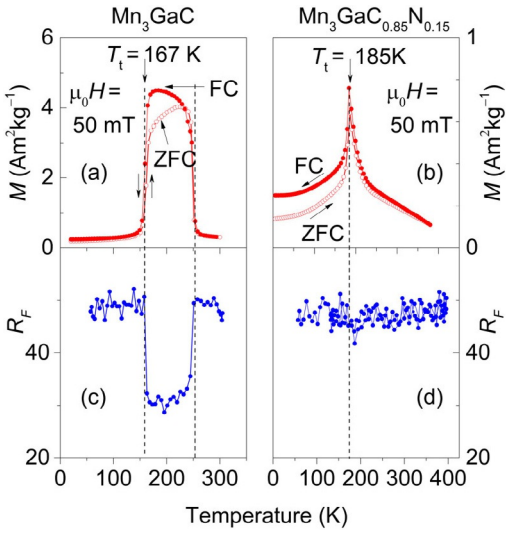

Figure 15. Temperature-dependent magnetization of (a) Mn_3GaC and (c) $Mn_3GaC_{0.85}N_{0.15}$ at 50 mT. The temperature dependence of the flipping ratio R_f of the transmitted neutrons is shown for (b) Mn_3GaC and (d) $Mn_3GaC_{0.85}N_{0.15}$. Figure adapted from Ref. [173], used with permission. Original Figure ©IOP PUBLISHING, LTD.

4. Effect of Hysteresis on the MCE around Magnetostructural Transitions

After the detailed analysis of the thermodynamic and magnetic fundamentals, which are important for magnetocaloric materials to understand the thermal hysteresis, we now focus in the following sections on studies about application-related properties as well as the role of thermal hysteresis and microstructure in dynamical experiments. Therefore, we will discuss possible discrepancies between the entropy diagram determined under equilibrium conditions and the properties ΔS_T and ΔT_{ad} determined from field-cycling experiments.

To develop the magnetocaloric material systems that are presented in this article towards efficient cooling under real

conditions, the materials have to be evaluated in terms of their adiabatic temperature change under cyclic magnetic fields. As the economic and ecological impacts of the permanent magnet needed to drive the MCE form a crucial issue,[63,174] it should be considered that the active magnetocaloric regenerator for a caloric cooling device is optimized for field frequencies of at least 1–10 Hz.[12] In particular, the material's shape is of great importance for efficient heat exchange with the fluid. Therefore, the dependence of the magnetostructural phase transition on the grain or particle size is investigated, as well as the influence of the field-sweep rate of the applied magnetic field on ΔT_{ad}, which yields information on the kinetics of the MCE. The influence of the microstructure on the thermal hysteresis and magnetic field cycling under non-equilibrium conditions is particularly discussed to evaluate the reversible ΔT_{ad} under application-relevant conditions for different material systems.

In this section, we investigate the influence of thermal hysteresis on the MCE for cyclic field applications. We start by introducing the effect of thermal hysteresis in the material system La–Fe–Si on both the entropy and adiabatic temperature change, before moving over to further material systems.

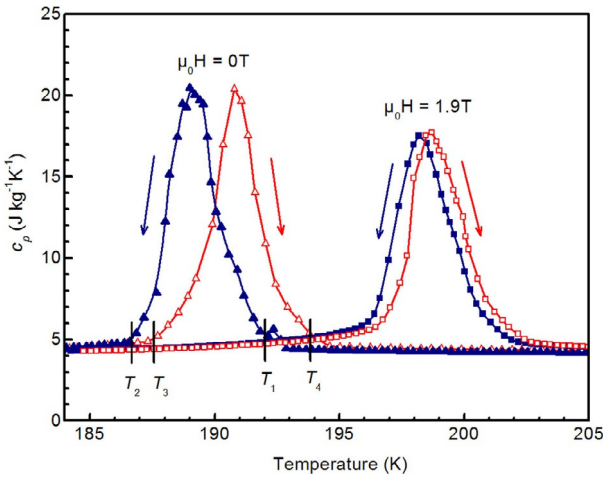

Figure 16. Temperature- and field-dependent specific heat capacity c_p of $LaFe_{11.6}Si_{1.4}$ both in an applied magnetic field of 1.9 T and with no field application. The closed symbols correspond to values measured upon cooling, whereas the open symbols correspond to the heating protocol. Figure adapted from Ref. [177], used with permission. Original Figure ©Elsevier.

4.1. $La(Fe_xSi_{1-x})_{13}$-based compounds

Because of their promising magnetocaloric properties, La–Fe–Si alloys are one of the most studied material systems for the development of active regenerator beds for cyclically operated magnetocaloric devices.[15,17,21,24,175,176] We will focus in the following on the discussion about the reversibility of the MCE by considering the $S(T)$ diagram and the underlying heat capacity data determined for the compound $LaFe_{11.6}Si_{1.4}$.[177]

In Figure 16, c_p measurements under 0 and 1.9 T are shown for both heating and cooling protocols with sharp peaks at the first-order phase transitions. The metastability of the phase transition at $\mu_0 H = 0$ T results in a distinct temperature width of the transition indicated by T_1–T_2 (for cooling) and T_4–T_3 (for heating) as explained in Figure 16. The transition is shifted to higher temperatures in the case of an applied field of 1.9 T, which leads to a reduction of the thermal hysteresis.[24] We used the c_p data shown in Figure 16 to construct the temperature-dependent total entropy curves shown in Figure 17a,b for the heating and cooling curves, respectively.[177] Therefore, we used the following equation and chose $T_{ref} = 185$ K, because below this temperature the entropy is almost independent of the magnetic field H:

$$S(T)_H = \int_{T_{ref}}^{T} \frac{c_{p,H}(T)}{T} dT + S(T_{ref})_H \quad (9)$$

The data in Figure 17 demonstrate the direct influence of thermal hysteresis both on the entropy change ΔS_T (panel b) and adiabatic temperature change ΔT_{ad} (panel a). Additionally, Figure 17 shows that the transition occurs not in a jump-like fashion, as expected for a first-order transition, and instead the FM and PM phases coexist over a finite tempera-

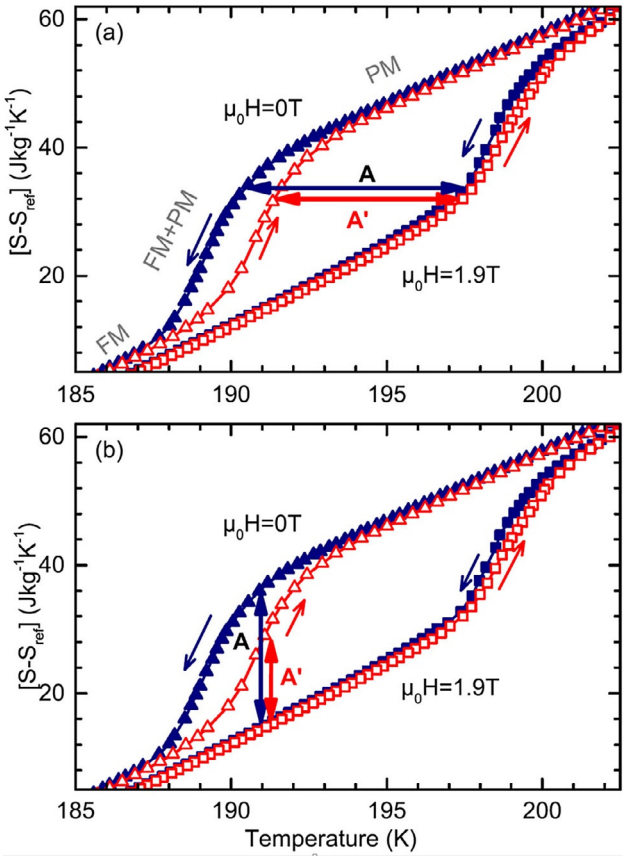

Figure 17. The calculated metastable $S(T)$ diagrams of $LaFe_{11.6}Si_{1.4}$ close to the first-order phase transition. The closed symbols correspond to values measured upon cooling, whereas open symbols correspond to the heating protocol. The adiabatic temperature change ΔT_{ad} is represented in panel (a) whereas the isothermal entropy change ΔS_T is represented in panel (b). Figure adapted from Ref. [177], used with permission. Original Figure ©Elsevier.

ture interval. Intriguingly, the finite temperature range of the transition cannot be linked to a chemical inhomogeneity of the material that results in a distribution of T_t. However, the large volume difference between the coexisting phases may exert stress on transforming grains, which may in turn shift their T_t, according to the large inverse barocaloric effect observed in this system.[178] In addition, the presence of metastable magnetic states of Fe, which are close in energy, as proposed earlier from theory,[51,52] may foster a smoother transition. Recent DFT calculations suggest, that the dependence of the energy on magnetization becomes rather flat after magnetic disorder has set in.[39,52] The mechanism of thermal hysteresis in the case of $LaFe_{11.6}Si_{1.4}$ is expected to be closely related to the volume expansion of this compound at the transition temperature T_t,[3] as discussed above in Section 2.

In the case of zero-field cooling, the sample transforms from a PM to FM phase along the $S(T)$ diagram, accompanied by latent heat, as shown in Figure 17a, b. A similar case can be observed in zero-field heating with a first-order phase transition. The curves obtained from the heating and cooling protocol define the hysteresis width of approximately 1.6 K. In the case of an applied field, the transition shifts by approximately 4.2 $K T^{-1}$ as shown by the curves measured in 1.9 T in Figure 17a, b.

The adiabatic temperature change can be directly determined by the horizontal arrows in the $S(T)$ diagram shown in Figure 17a and the isothermal entropy change by the vertical arrows as shown in Figure 17b. The effect of thermal hysteresis becomes directly obvious from this presentation. Due to the fact that the first-order phase transition can be driven by a magnetic field or temperature, the end point of the horizontal line indicating ΔT_{ad} will always lie on the cooling branch of the entropy curve when a magnetic field is applied, as illustrated by arrow A in Figure 17a. The arrow does not finish on the entropy curve corresponding to the heating of the sample because this corresponds to the reverse temperature-driven first-order phase transition. Upon field removal, the arrow ends on the heating entropy curve for zero-field application, thereby reducing ΔT_{ad}. Therefore, under cycling in a magnetic field the arrows in the $S(T)$ diagram will be bound by the entropy curve for heating under zero field and by the cooling curve under an applied magnetic field (arrow A′) leading to a reduced temperature change for the second as well as for all consecutive magnetization and demagnetization cycles compared to the first cycle.

The discussion is similar for the isothermal entropy change ΔS_T. In this case, the magnitude can be determined from the vertical lines in the $S(T)$ diagram in Figure 17b. On the first cycle, the isothermal entropy change ΔS_T (indicated by arrow A) is higher than in the consecutive cycles (arrow A′).

The temperature-dependent ΔT_{ad} is shown in Figure 18 for multiple cooling and heating cycles. The first cooling and heating cycles correspond to arrows A and A′ in Figure 17a. For the first cycle, an adiabatic temperature change of approximately 7 K at 190.5 K was observed under a field change of 1.9 T. Upon heating, the sample in the first cycle

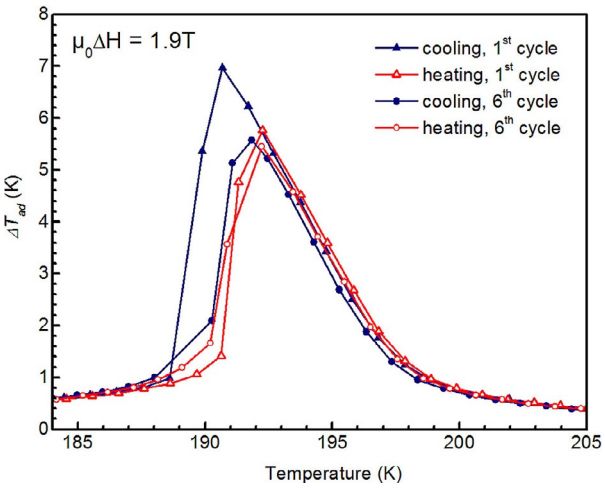

Figure 18. The adiabatic temperature change ΔT_{ad} measured upon cooling (closed symbols) and heating (open symbols) in a field change of 1.9 T for the first field application cycle and the cyclic values measured on the 6th cycle. Figure adapted from Ref. [177], used with permission. Original Figure ©Elsevier.

exhibits a temperature change of 5.8 K at a peak temperature of 192.2 K with a hysteresis width of 2.2 K. After field cycling, the hysteresis drops nearly to zero and a cyclic value of the adiabatic temperature change for all consecutive heating and cooling cycles was observed, as indicated by the sixth cooling cycle in Figure 18 of 5.6 K at 192 K. These values agree well with the values obtained indirectly by the $S(T)$ diagram in Figure 17a leading to a reduction of the obtainable adiabatic temperature change by 20% due to thermal hysteresis.

4.2. Ni–Mn–X(–Co) Heusler alloys

Following the previous detailed description of the fundamental thermodynamic background of the reversibility for cyclic field applications in a magnetocaloric system, we now discuss the influence of thermal hysteresis for the family of Ni–Mn–X(–Co) Heusler compounds. They are characterized by a thermal hysteresis of 5–20 K, depending on the Heusler system, further substitutions, and the micro- and crystal structure that results from the composition.[179] Therefore, the hysteresis is considerably larger than for the La–Fe–Si material system and highly diminishes the reversible magnetocaloric effect in these alloys.[16,180–184] Even though large adiabatic temperature changes of up to −8 K can be obtained for Ni–Mn–In–Co under a magnetic field of 2 T for the first field application, the reversible effect is considerably smaller.[185] Due to a significant field sensitivity that shifts the phase transition down to lower temperatures by $-8\,K\,T^{-1}$ for the compound $Ni_{45.7}Mn_{36.6}In_{13.5}Co_{4.2}$ in Figure 19a, applying a magnetic field of only 2 T under isothermal conditions causes a complete transformation. However, higher fields would be necessary to complete the back transition as well and transform the material back to its original state by decreasing the field back to zero. Therefore, the directly measured adiabatic

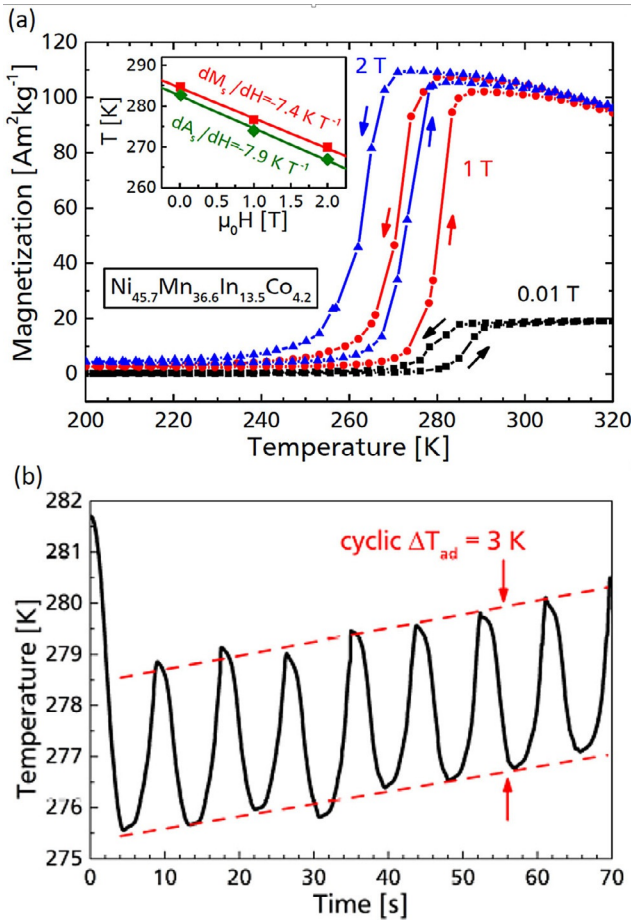

Figure 19. (a) Magnetization curves depending on the temperature of the $Ni_{45.7}Mn_{36.6}In_{13.5}Co_{4.2}$ Heusler alloy in different magnetic fields up to 2 T. The shifts of starting temperatures for martensite (M_s) and austenite phase formation (A_s) depending on the applied magnetic field are shown in the inset. (b) Adiabatic temperature change of this sample upon cyclic application of a magnetic field of 1.9 T. Figure adapted from Ref. [185], used with permission. Original Figure ©AIP Publishing.

temperature change under a cyclic magnetic field of 2 T is reduced to 3 K due to thermal hysteresis (Figure 19b), which corresponds to an irreversibility ratio of 62.5%.

An even more drastic reduction of the reversible magnetocaloric effect under cycling exists for Ni–Mn–Sn(–Co) Heusler alloys. The compounds with little or no amount of Co are characterized by a larger thermal hysteresis and lower field sensitivity of the phase transition compared to the Ni–Mn–In compounds.[86,138] Therefore, the magnetocaloric signal of the second field cycle is often overlaid by heating due to the conventional MCE near the Curie temperature of the austenite phase, and the material does not show any reversibility by direct ΔT_{ad} measurements for $Ni_{50}Mn_{36}Sn_{13}Co_1$,[182] $Ni_{48.6}Mn_{34.9}Sn_{16.5}$,[16] and $Ni_{51.2}Mn_{35.1}Sn_{13.7}$.[186] However, compounds with an increased amount of Co substitution show a smaller thermal hysteresis, which leads to a reversible ΔT_{ad} of −1.2 K compared to −2.5 K (50% reversibility) for the first field cycle for $Ni_{45.7}Mn_{37.9}Sn_{11.5}Co_{4.9}$.[186] Detailed investigations of the influence of thermal hysteresis on the reversibility of the magnetostructural phase transition predict that magnetic fields of 9–12 T are necessary to induce a fully reversible MCE for the Ni–Mn–Sn–Co system.[187–189]

During a cyclic process with lower magnetic fields, the material cannot overcome the thermal hysteresis completely and the characteristic temperature dependence of magnetization, which represents the fractions of austenite and martensite during the transition, is described by minor loops inside the thermal hysteresis area. These minor loops are highly dependent on the size and shape of the complete thermal hysteresis loops for the different Heusler alloys.[16] The understanding of the transformation processes in minor loops can be a step forward to enhance the cyclic MCE in Heusler alloys. In analogy to the La–Fe–Si alloys, an entropy diagram can be constructed from direct calorimetric measurements and heat capacity data of Ni–Mn–In–Co.[190] The resulting $S(T)$ diagram is shown in Figure 20 for zero magnetic field and a field of 2 T, respectively, for the first field application as well as for the reversible MCE.

The data for the total entropy fit very well with the values for isothermal entropy change and adiabatic temperature change determined experimentally, as depicted in Figure 20a. However, the directly measured reversible effect in Figure 20b is larger than expected from the area between the entropy data under 0 T and cooling as well as the 2 T curve under heating. Even for compounds that do not show any reversibility in the $S(T)$ diagram, a reversible adiabatic temperature change can be measured.[191] This finding is explained

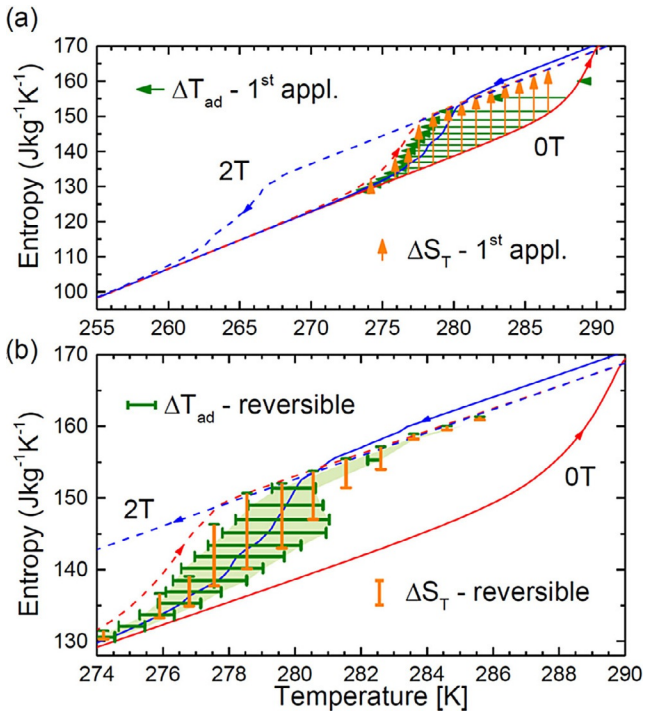

Figure 20. Entropy vs. temperature diagram for $Ni_{45.7}Mn_{36.6}In_{13.5}Co_{4.2}$ Heusler alloy in 0 and 2 T with arrows that depict the directly measured adiabatic temperature change (horizontal) and isothermal entropy change (vertical) for a field change of 2 T for the first field application (a) and further cycles (b). Figure adapted from Ref. [190], used with permission. Original Figure ©AIP Publishing.

by the special characteristics of the minor loops and demonstrates that the actual cyclic effect cannot be predicted by isofield experiments only. As the calorimetric measurements represent a quasi-static method, the actual properties from fast field cycling experiments are not reproduced accordingly, although this is in principle possible for calorimetric measurements with limited field-sweep rates.[191,192] The evaluation of minor loops starting at temperatures where a mixed state of martensite and austenite is present in the sample shows that the thermal hysteresis is reduced significantly. It follows that the energy barrier for the formation of a new martensite phase is reduced compared to a pure austenitic starting state. As martensitic areas are already present in the sample, they act as nuclei for the formation of new martensite and reduce the energy barrier that is needed for phase nucleation.[190] From the application point of view, this gives the perspective of enhancing the achievable reversible temperature change by designing minor loops of hysteresis with optimal starting conditions and similar fractions of austenite and martensite present. This state favors phase-boundary motion instead of energy-intensive nucleation processes, thereby enabling a microstructurally tuned cyclic MCE that is larger than predicted from thermodynamic $S(T)$ diagrams.[190,191]

In addition, it has been shown that the approaching speed towards the measurement temperature also plays an important role for the reversibility of the MCE.[191] High approaching speeds favor a magnetic-field-induced phase transition when starting in the pure martensitic state. Residual stress in the martensite can occur from the fast approaching rate of the temperature. This effect moves the sample away from equilibrium conditions and the austenite formation is favored. Therefore, the thermal hysteresis is reduced by the pressure arising from the internal microstructure of the martensite, which is comparable to the modification of the effective thermal hysteresis by using external hydrostatic pressure in a multicaloric cooling cycle, as proposed in Ref. [11]. Due to the microstructural stress dependence of the martensitic phase transition in Heusler alloys, external mechanical modifications can also influence the transition. It has been shown for instance that the thermal hysteresis can be reduced on a local scale by nanoindentations. Creating elastic stray fields from regions of plastic deformation leads to a reduction of the nucleation barrier and thus to stress-induced martensitic nuclei formation at higher temperatures than would be expected for a stress-free state.[193]

4.3. Mn_3GaC-based antiperovskites

In the following, we will discuss magnetocaloric compounds of the Mn_3GaC and Mn_3GaN family concerning reversibility issues that result from the occurrence of thermal hysteresis. As already introduced in Section 3, in these antiperovskites a narrow thermal hysteresis is observed that leads to a large MCE with high reversibility. Furthermore, the thermal hysteresis can be eliminated by tuning the magnetostructural phase transition to make the first- and second-order transitions coincide. As examples, we will focus here on the compounds Mn_3GaC and $Mn_3Ga(C_{0.85}N_{0.15})$. For the case of Mn_3GaC, the compound orders ferromagnetically at a $T_C = 250$ K and undergoes an isostructural phase transition to the AF state at $T_t = 165$ K, as depicted in Figure 21 a. The transition temperature is shifted towards lower temperatures at a rate of $-4.4\ \mathrm{K\,T^{-1}}$ upon applying a magnetic field.

Therefore, it experiences an inverse MCE in a comparable way to the Heusler alloys. Both T_t and T_c can be tuned by various elemental substitutions on the Mn or Ga sites[168–170] as well as by external pressure.[194,195]

Direct measurements of the adiabatic temperature change under a magnetic field of 3 T show an MCE of up to −3.1 K for the first field application.[41] In accordance to the previously discussed systems, this value is reduced upon further field applications and the material is cycled within minor loops of hysteresis. However, the narrow thermal hysteresis and the significant magnetic field sensitivity of the phase transition lead to a cyclic temperature change of −2.8 K as shown in Figure 21 b.[41] Therefore, this material represents a system where the working minor loops are close to a full transformation. The irreversibility of the adiabatic tempera-

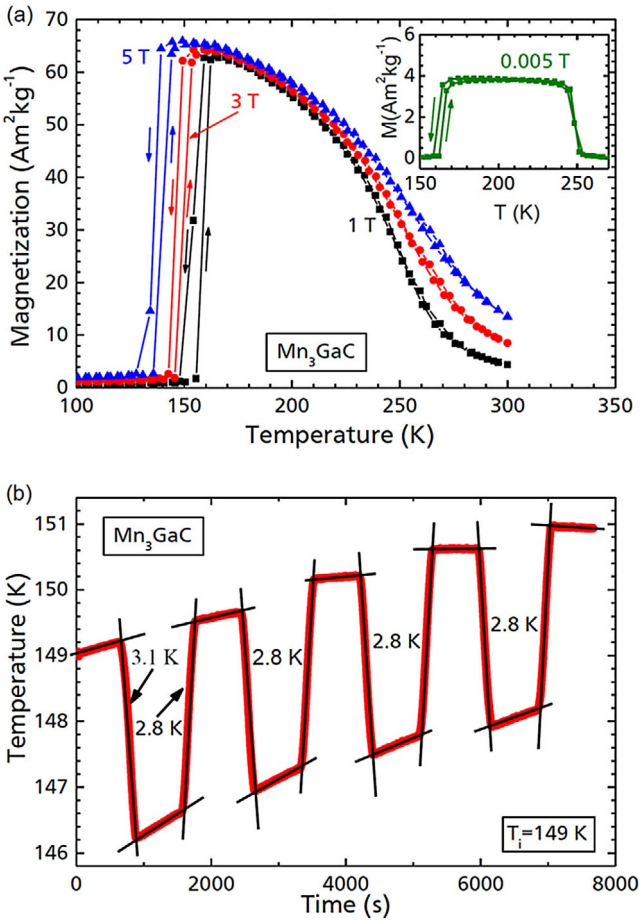

Figure 21. (a) Magnetization curves depending on temperature for Mn_3GaC antiperovskite in different magnetic fields up to 5 T. (b) Evolution of the reversible adiabatic temperature change for first field application and further field cycles in a magnetic field of 5 T for the starting temperature of 149 K. Figure adapted from Ref. [41], used with permission. Original Figure ©AIP Publishing.

ture change under magnetic field cycling is only 10% of the ΔT_{ad} value for a full transformation.

An additional option to tune the structural transition temperature T_t and the Curie Temperature T_c is by substituting carbon with nitrogen to form a $Mn_3Ga(C_{1-x}N_x)$ compound.[167] For the composition $Mn_3Ga(C_{0.85}N_{0.15})$, the thermal hysteresis vanishes and a phase transition from an AF state to an enhanced paramagnetic state is observed. The enhanced paramagnetic phase shows no strong FM ordering (see Section 3.2). An external magnetic field induces FM correlations and shifts the transition temperature of the magnetostructural transition at a rate of $-2.5\,K\,T^{-1}$.[172] In the absence of thermal hysteresis, a completely reversible magnetocaloric effect can be induced by magnetic field changes, which is proven by direct measurements of the adiabatic temperature change. The measurements show a fully reversible ΔT_{ad} of 3 K for the first field application as well as for further field cycling at 3 T.[172]

4.4. Fe_2P compounds

Fe_2P-type alloys represent a promising class of materials that show a sharp first-order phase transition.[196,197] The most promising material compositions to this point are based on Mn, Fe, P, and Si.[5,198–200] A sample of $Mn_{1.32}Fe_{0.71}P_{0.5}Si_{0.56}$ with a phase purity of 95 wt% was produced by a powder-metallurgical route as described in Ref. [59].

The magnetization curves of this compound at 0.2 and 2 T are shown in Figure 22a. The thermal hysteresis is determined from both inflection points of the heating and cooling curves and corresponds to approximately 7 K with a magnetization of 115 $A\,m^{-2}\,kg^{-1}$ under a field of 2 T, which agrees well with literature values.[201] The thermal hysteresis in this material is assumed to be related to the anisotropic lattice volume change of the sample, thereby resulting in only a minimal volume change.[56] In Figure 22b the temperature-dependent adiabatic temperature change is shown for a field change of 1.9 T, which results in a maximum ΔT_{ad} of 2.35 K measured on the cooling branch. To judge the cyclic magnetocaloric effect, the temperature change of the material is plotted versus time in the inset of Figure 22b, undergoing a field cycle from 0 to 1.9 T to 0 to −1.9 T and back to 0 T, mimicking an application-relevant cooling cycle. Due to the effect of thermal hysteresis explained above, the cyclic and reversible adiabatic temperature change ΔT_{ad}^{rev} at a peak temperature of 268 K is reduced by 24% to only 1.9 K.

This analysis of the influence of thermal hysteresis on the reversible magnetocaloric properties of field-induced phase transitions shows that it is crucial to determine the important aspects of reversibility from direct ΔT_{ad} measurements. Even though it is not easy to access this quantity, the reversible MCE upon magnetic field cycling under application-relevant conditions is crucial to assess the potential of a magnetocaloric material for cooling purposes. For the different material systems discussed here, the direct correlation between thermal hysteresis in combination with the shift of T_t by an applied magnetic field (dT_t/dH) and the reversible ΔT_{ad} is

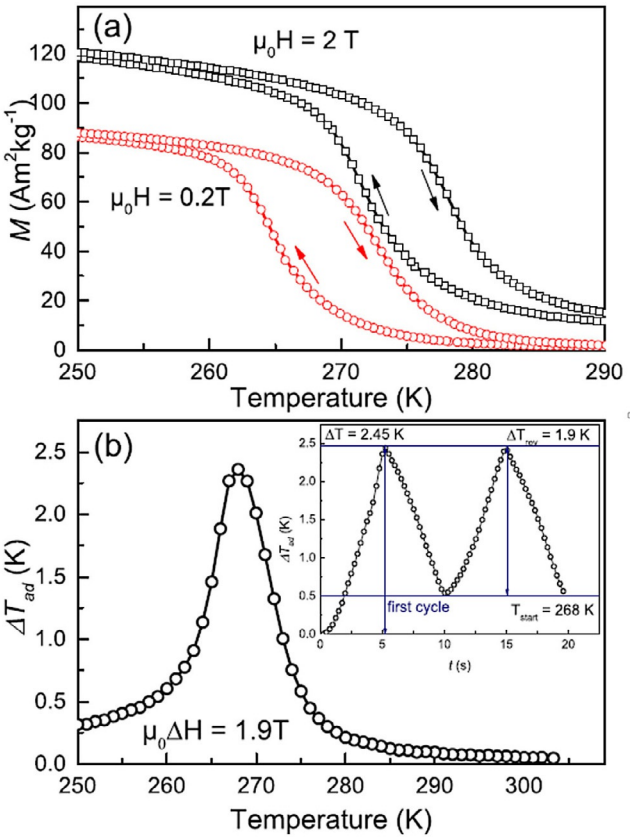

Figure 22. (a) Temperature-dependent magnetization at fields of 0.2 and 2 T measured upon cooling and heating of $Mn_{1.32}Fe_{0.71}P_{0.5}Si_{0.56}$. In panel (b) the adiabatic temperature change ΔT_{ad} is shown measured on the cooling branch in a field change of 1.9 T. The inset shows the time-dependent, cyclic MCE measured at a peak temperature of 268 K. Figure adapted from Ref. [59], used with permission. Original Figure ©Elsevier.

apparent. Even though Heusler alloys show a large MCE upon first field application, which can be in the range of those of La–Fe–Si alloys, in addition to a large field sensitivity, the thermal hysteresis is larger than 10 K, which highly diminishes the cyclic effect. However, the narrow thermal hysteresis of La–Fe–Si alloys allows for a larger reversible temperature change, which highly favors the development of this alloy system towards cooling applications. Similarly, high reversibility ratios on a smaller absolute temperature scale can be obtained for the systems of Fe_2P and Mn_3GaC with narrow thermal hysteresis. An effective tuning of the phase transition towards second order reduces the thermal hysteresis to a minimum and therefore enables a fully reversible field-induced MCE.

5. Size-Dependence of Magnetocaloric Particles on the Magnetocaloric Effect

The material size is an essential issue in terms of its application in a magnetic refrigerator. To provide an efficient magnetocaloric regenerator operating at several Hertz, the surface of the material needs to be very large such that good heat transfer between the material and the exchange fluid is

possible. This can be achieved by creating fine structures with well-organized micro-channels, for instance by selective laser melting.[202] It is also possible to build a regenerator from magnetocaloric plates. These plates should have a thickness of no more than 300 μm, because otherwise the heat transfer would not be efficient.[203] The most straightforward way to obtain a good magnetocaloric heat exchanger is the use of a powder bed. However, it has the drawback that the pressure drop can be significantly higher in a powder-based regenerator in comparison to a plate geometry, which becomes relevant especially at higher operation frequencies.[204] For both the bonded plates and the powder bed, a base material with a particle size of less than 300 μm is required. For this reason, it is a crucial question how the magnetostructural transition takes place in small particles. This aspect can be clarified through magnetic measurements of single fragments with different sizes, which were performed for the Heusler compound $Ni_{45.7}Mn_{36.6}In_{13.5}Co_{4.2}$, $LaFe_{11.8}Si_{1.2}$ and $Mn_{1.2}Fe_{0.68}P_{0.5}Si_{0.6}$.[205]

In Figure 23, the magnetic moment of the bulk Heusler sample (upper curve) and of different single particles in a magnetic field of 1 T are plotted as a function of temperature. To characterize the transformation properties of micrometer-sized particles, small fragments of the material were isolated under a light microscope and subsequently fixed to the sample holder with Kapton tape. The diameter was determined by relating the change of the magnetic moment during the transformation to that of the bulk sample to obtain the mass of the fragment. By using the density of 8 g cm^{-3}, the volume can be approximated and is represented by the diameter of a spherical particle of the same volume.

As presented in Figure 23, the transition width of the 250 μm particle is several times broader than in the bulk sample. Also the thermal hysteresis is approximately twice as large. Furthermore, the transformation from martensite to austenite starts at approximtely 285 K, which is 10 K higher than in the bulk material. This size-dependent behavior becomes even more pronounced for smaller particles. For instance, a particle with a diameter of approximately 100 μm shows a tremendously increased transition width from austenite to martensite, spanning over more than 50 K. The study of more than ten single fragments revealed that the transition is scattered. This is mainly related to the variation of the chemical composition of the alloy, which strongly influences the transition temperature.[43]

During the melting and heat treatment of the alloy, slight inhomogeneities in the local composition are unavoidable that affect the transition temperature of the particles. However, the origin for the broadening of the transition and the increase in hysteresis could not be definitively identified. In fact, the martensite structures in millimeter-sized samples, as observed by optical microscopy for instance in Ref. [185], are also in the millimeter range. However, in thin films, the martensite features are much smaller.[206] This is due to the formation of martensite nuclei which have an uneven aspect ratio.[207] These needle-like structures somehow must fit into the small fragments. This process becomes exceedingly difficult the smaller the samples get. Also the role of defects and the increasing importance of the surface, which creates stresses, could be related to the observed size effects.[193]

Magnetic measurements of bulk $LaFe_{11.8}Si_{1.2}$ and of small single particles are shown in Figure 24. In this compound, the sharp first-order transition takes place below 200 K. The thermal hysteresis of the bulk sample is very narrow, which is apparent in the upper curve. Four different particles with sizes of 400 down to 20 μm are plotted in Figure 24 as well. The transformation of small fragments is always jump-like, at least within the measurement resolution. Furthermore, it is clear that the thermal hysteresis also increases in comparison to the bulk material. In La–Fe–Si, a distribution of the transition temperature is visible, but it is not as pronounced as in the Heusler sample. This could be related to the fixed 1:13 stoichiometry between La and (Fe,Si) so that only the Fe-to-Si ratio can, in principle, change locally. In contrast to that, in the Ni–Mn–In-based Heusler sample all elements are mixable in a large composition range of the Heusler phase without the formation of secondary phases.[208] The reduced varia-

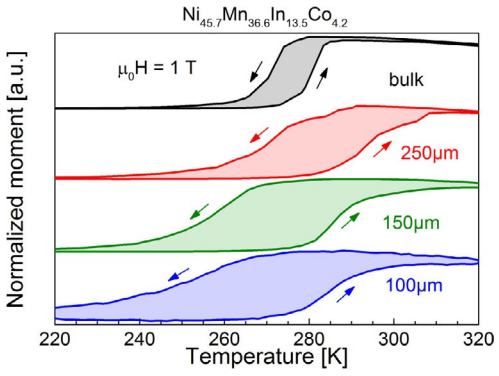

Figure 23. Comparison of the magnetic behavior of a bulk sample and differently sized fragments of $Ni_{45.7}Mn_{36.6}In_{13.5}Co_{4.2}$ in a magnetic field of 1 T. Figure adapted from Ref. [205], used with permission. Original Figure ©Wiley-VCH.

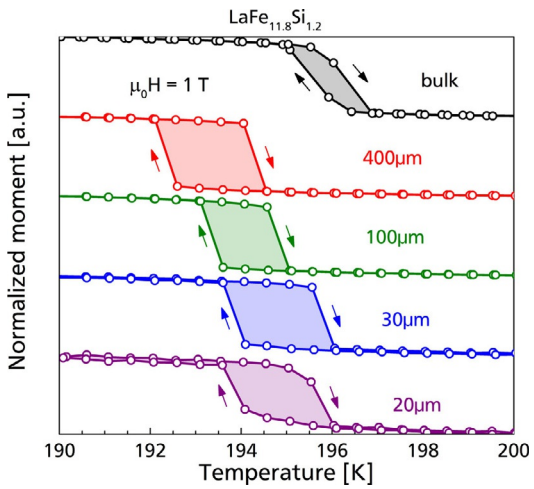

Figure 24. Comparison of the magnetic behavior of a bulk sample and differently sized fragments of $LaFe_{11.8}Si_{1.2}$ in a magnetic field of 1 T. Figure adapted from Ref. [205], used with permission. Original Figure ©Wiley-VCH.

tion of the transition temperature could also originate from the typically much longer heat treatment of La–Fe–Si compounds. This is required because the 1:13 phase forms in a peritectic reaction.[209] It is likely that the local chemical composition does not change much because of the special formation character of the magnetocaloric phase.

As a third material example, the results for the Fe_2P-type compound $Mn_{1.2}Fe_{0.68}P_{0.5}Si_{0.6}$ are plotted in Figure 25. This particular alloy transforms near room temperature. Starting at 300 K, two cooling and heating sequences have been performed on the fresh material to study the so-called virgin effect.[210] The largest particle with a size of approximately 300 μm shows an increasing magnetization just below 270 K in the first cooling of the fresh material. Upon repeating the sequence, the transition takes place at approximately 10 K higher than before. However, the virgin effect vanishes for single particles with sizes below 60 μm. This behavior was also observed in the La–Fe–Si sample, where the transformation of small fragments proceeds with a jump-like transition; a slight increase of the thermal hysteresis was also observed along with a distribution of the transition temperature.

In conclusion, we have identified important aspects of the magnetostructural transition in a Heusler compound as well as in La–Fe–Si and Fe_2P-type samples from magnetic measurements of single particles. It became obvious that a reduction of the size can lead to a significant obstruction of the martensitic transition in the Heusler alloy. This implies that Heusler compounds might not be used as a powder bed magnetocaloric regenerator with a particle size in the sub-micrometer range because both the transition width and the thermal hysteresis would increase. However, for plate geometries cut from bulk material, this is probably not so critical, as also in thin films it is possible to obtain relatively sharp transitions with modest thermal hysteresis.[211] For the two other materials, such a broadening of the transition was not observed in small fragments in the size range relevant for application. Consequently, $LaFe_{11.8}Si_{1.2}$ and $Mn_{1.2}Fe_{0.68}P_{0.5}Si_{0.6}$ can be used efficiently, also in form of a fine powder. However, an increased distribution of transition temperatures was observed in all three materials, even larger than the transition width of the bulk sample. This raises the question of how the transformation can be made sharper in a material of larger size that is built from particles with a spread in their transition temperatures.

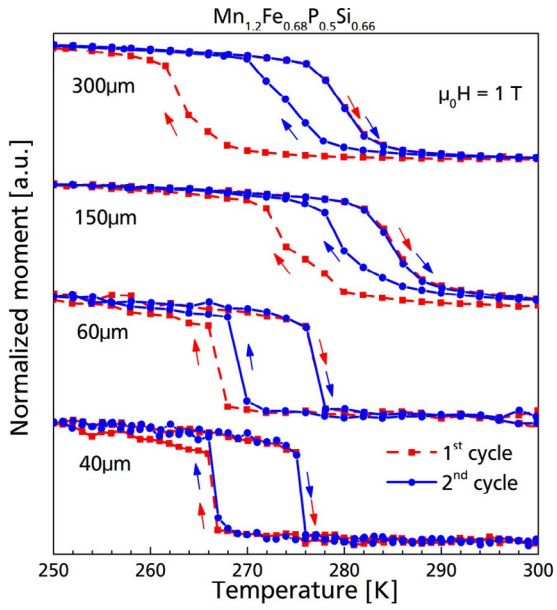

Figure 25. Comparison of the magnetic behavior of differently sized fragments of $Mn_{1.2}Fe_{0.68}P_{0.5}Si_{0.6}$ in a magnetic field of 1 T. The first and the second cooling and heating cycles are plotted in red and blue, respectively.

Modeling of magnetostructural transitions

The magnetostructural transition in magnetocaloric materials can be influenced by the application of hydrostatic pressure. The reason for this behavior is the volume change of the unit cell, which is related to the martensitic transformation. For Heusler alloys, the transition is shifted to higher temperatures because pressure stabilizes the phase with the smaller volume, which is the martensite phase (conventional barocaloric effect). From XRD measurements, the volume change during the transition was determined to be in the range of 1 %.[212] For La–Fe–Si, similar volume changes were observed.[176] However, the substitution of Fe by Co leads to an increase of the transition temperature and a reduction of ΔV. This is accompanied by a change of the transition type from a first- to second-order transformation.[176]

Furthermore, it was demonstrated in the literature that, for instance in $LaFe_{11.8}Si_{1.2}$, a rather large sample of 0.12 mm^3 (effective radius ≈300 μm) has a sharp transition based on magnetization measurements, whereas the crushed powder from the precursor particle resulted in a broad transition.[213] This behavior is in agreement with the results from the single-particle measurements in the previous section. Due to inevitable chemical inhomogeneity, the transition temperature of each fragment varies to some extent. However, when those fragments are connected, the transition is much sharper than the average of the particle ensemble. To understand this mechanism, finite-element simulations were performed, which suggested that the coupling of individual fragments by mechanical stress, together with the sensitivity of the transition temperature to stress and pressure, form the origin for the sharpening effect of the transition in bulk materials.[205]

The simplest problem is the two-cube scenario. For the simulation, an artificial material with the following properties is postulated. The material is constructed from two individual cubic elements, as illustrated in Figure 26a. The two elements have slightly different fictitious transition temperatures and their transformations start at 300 and 305 K, respectively. During the transformation from the low- to the high-temperature phase, the individual blocks expand. The length change is 0.33 %, which results in a volume change of approximately 1 %. It is assumed that the transition takes place continuously over a certain temperature interval of 15 K in this example. The high-temperature phase fraction of the individual elements is illustrated in Figure 26b. It is fur-

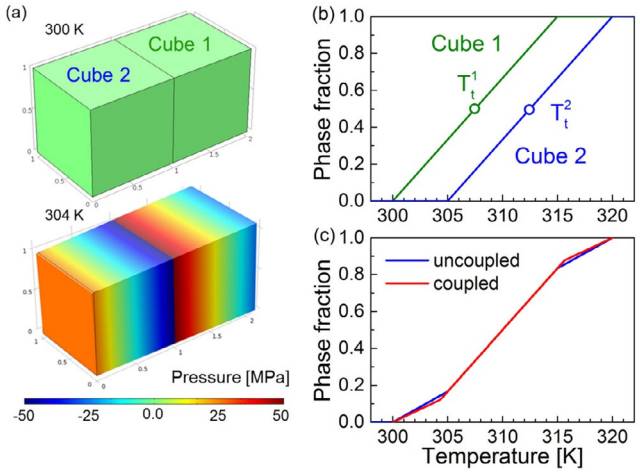

Figure 26. (a) Stress evolution in the two-cube problem. (b) Individual transition temperature of the two cubes. (c) Coupled (red) and uncoupled (blue) situation of the two-cube problem. The inset shows a zoomed in view of the critical region.

thermore assumed that the elastic properties (the Young's modulus $E = 100$ GPa and the Poisson's ratio $\eta = 0.3$) do not change during the transition.

If there was no coupling by stress, the transition temperature of the two-block ensemble and would just be the average of the two individuals (uncoupled curve in Figure 26c). Between 300 and 305 K only cube 1 transforms, but at higher temperatures both elements transform and a larger slope is observed. Above 315 K, cube 1 is already in the pure high-temperature phase, but cube 2 transforms further.

The situation changes when the coupling by stress is considered (coupled curve in Figure 26c). At 300 K, the ensemble is in the stress-free state as is shown in Figure 26a. However, increasing the temperature leads to an expansion of cube 1. Since it is connected to the second element, both elements are deformed and a stress field evolves. These stresses can be significant, as for instance shown for the state at 304 K, reaching values up to 50 MPa. Therefore, a compressive stress acts on cube 1, which shifts the transition temperature upwards. This coupling to stress is considered in the simulation by the following equation:

$$x_t = \left(T - T_t + \frac{\sigma_{xx} + \sigma_{yy} + \sigma_{zz}}{3} \cdot \frac{dT_t}{dp}\right)\frac{1}{\omega} + 0.5 \quad (10)$$

with $x_t \in [0,1]$

The parameter x_t describes the phase fraction of the individual element. It depends on the elemental transition temperature T_t, defined by the middle position of the transformation, the transition width ω, the coupling constant dT_t/dp and the normal stresses σ_{xx}, σ_{yy}, and σ_{zz}. The shift of the transition temperature by stress dT_t/dp was selected to be 50 K GPa^{-1} according to pressure-dependent magnetization measurements from the literature.[11,43,178]

In the stress-free case, Equation (10) simply results in a linear transformation shape of the individual element. However, to quantify the stress coupling, the local stress field must be calculated. For larger problems, this optimization procedure can be very time-consuming and even lead to instability in the simulation. The solution of the stress-coupled problem is shown in Figure 26c as well. In fact, there is no big difference between the coupled and the uncoupled situation, but in the temperature range of 300–305 K one can clearly see that the transformation of cube 1 is suppressed, which is indicated by a smaller slope. At approximately 304.3 K, cube 2 also starts to transform and both elements continue together. This result is nothing else than a sharpening of the ensemble transition even though it is not very pronounced.

In the following, an artificial first-order magnetocaloric material consisting of 1000 individual blocks with randomly distributed transition temperatures is considered. To simulate a certain variation of the local transition temperature due to chemical inhomogeneity, a Gaussian distribution with a standard deviation of 2 K or a full width at half maximum (FWHM) = 4.3 K was used. The peak position of the distribution was set to a fictitious temperature of 305 K. In the uncoupled case, the transformation character of the ensemble is described by the average of all individual particles and should therefore be similar to the transition of a loose powder composed of the different fragments. An image sequence of this transition is illustrated in Figure 27a. In the pictures, only elements that are at least half transformed are visible, from which the arbitrary nature of the uncoupled transformation is obvious.

The situation changes drastically when the stress-coupling mechanism is active, as illustrated in Figure 27b. One can see that the transformation is preferentially initiated in the corners of the finite-element mesh because elements on the sur-

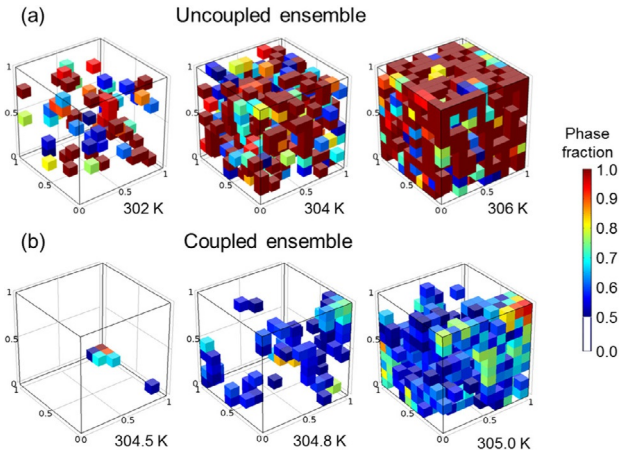

Figure 27. Image sequence of the transformation of an ensemble of 1000 elements in the uncouple case (a) and when being coupled by stress with $dT_t/dp = 50$ K GPa^{-1}. The transition width of the individual elements is $\omega = 1$ K. The elemental transition temperature is randomly distributed by means of a Gaussian distribution with a standard deviation $\sigma = 2$ K and the peak transition temperature of 305 K. Figure adapted from Ref. [205], used with permission. Original Figure ©Wiley-VCH.

face are not as restricted as elements inside the body. Surface blocks, and especially blocks in the corners, can expand more easily. Once initiated, the furthest-transformed elements apply tensile stresses to their neighbors, which lowers their transition temperature and forces them to convert as well. As a consequence, an avalanche progresses through the mesh and the material transforms together. This result is rather interesting as this transformation behavior can be understood as a nucleation and growth process, even though no such feature was implemented in the FEM study. The only mechanism that drives this combined ensemble transition is the stress coupling of neighboring blocks due to the volume change during the first-order transition and the sensitivity of the transition to external pressure and stress.

Figure 28 illustrates the influence of the coupling constant dT_t/dp on the ensemble transition. The individual transition of each element has a width of 1 K, which is illustrated in the inset. In the uncoupled case (black curve), the ensemble transition is simply the average of the individual transition temperatures, which is similar to an error function of the Gaussian distribution.

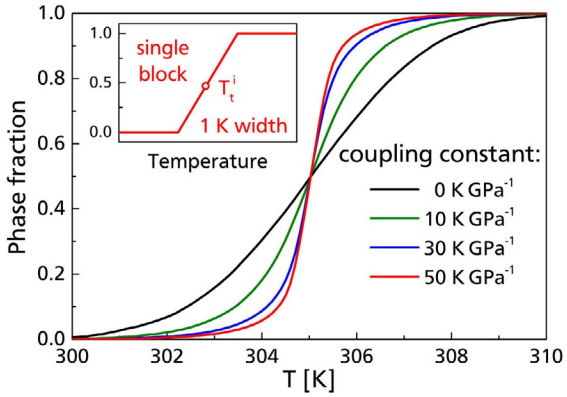

Figure 28. Transformation of an ensemble of 1000 elements for different coupling constants dT_t/dp. The standard deviation σ of the Gaussian distribution is 2 K and the individual transition width $\omega = 1$ K. The inset schematically illustrates the transformation of an individual block. Figure adapted from Ref. [205], used with permission. Original Figure ©Wiley-VCH.

A small coupling constant of only 10 K GPa^{-1} already has a strong influence on the properties of the ensemble. The transformation is completed in a much smaller temperature window. This trend continues for higher values of dT_t/dp. In real materials, a coupling constant in the range of 50 K GPa^{-1} was measured. For this strong coupling, the ensemble transition becomes even sharper. In fact, the transition approaches the transition width of a single block ($\omega = 1$ K), or in other words the ensemble behaves as one.

Such a behavior is for instance observed in the La–Fe–Si particles shown in Figure 24. Despite the distinct distribution of the transition temperature of individual elements, a sharp transformation can be obtained in bulk form. This finding is also in agreement with the single-particle measurements of the Heusler compound, which show a large scattering of the transition in different fragments. Although the results from the stress-coupling simulations are promising, one needs to consider that a real material is much more complicated than can be described by the simulations scheme.

So far, an artificial material with a cubic–cubic transition with a volume expansion of 1 % has been considered in the finite-element simulation. This is a suitable model, for instance, for La–Fe–Si, thereby leading to a sharpening of the transition due to the stress-coupling mechanism. However, for Fe_2P-type materials, this is not a useful description. In this material family, an isostructural hexagonal–hexagonal transformation is observed. The change in the lattice parameters is highly anisotropic as the crystal is shrinking along the *c*-direction but expanding along the *a*-axis. This change of the lattice parameters does not necessarily lead to a net volume change. It can be compensated, as for instance reported by Guillou et al.[200] It is worth noting that even in the case of $\Delta V/V = 0$, large stresses evolve during the transformation, which will be further investigated.

To model such an anisotropic behavior, the individual mesh elements are assumed to be a cubic cutout of the hexagonal cell. The high-temperature phase is considered as the stress-free state. By cooling the material to the low-temperature phase, the single blocks are distorted tetragonal. The specific values of the changing lattice parameters of $\Delta c/c = -1.7$ % and $\Delta a/a = 0.8$ % were selected according to the literature.[214,215] Even though the lattice changes drastically, the volume change is only approximately 0.1 %. To obtain reasonable results in the simulations, it has to be considered that the coupling constant is not equal along the different crystallographic directions. For the sake of simplicity, we assume dT_t/dp to be 50 K GPa^{-1} with positive sign along *c*- but negative sign in *a*-direction. In Figure 29a, the corresponding transformation behavior in the anisotropic case is shown. For the simulation, a standard deviation of the transition temperature σ of 2 K and a transition width of the individual element $\omega = 1$ K was used. It should be pointed out that the high-temperature phase was considered as the stress-free starting state. Therefore, all curves in Figure 29a start at a phase fraction of 0 above 310 K. By cooling the material, the transformation into the low-temperature phase takes place. For the loose powder case, this transition is completed within 10 K.

As a first stress-coupled example, a perfectly textured material will be considered. This means that the *c*-axis of all elements points along the *z*-direction. It is shown in Figure 29a that the transformation under cooling is rather sharp. In fact, the textured problem yields a similar result to that of the cubic–cubic transition shown in Figure 28. Only the length changes of the elements are different between the simulations. In substantial contrast, when the *c*-axis of each mesh element is distributed randomly along the *x*-, *y*-, or *z*-direction, the transition of the ensemble is significantly hindered by itself as plotted by the isotropic curve in Figure 29a. The two small images pointing at 285 K illustrate the result of the anisotropic expansion. Neighboring elements that are aligned differently disturb each other immensely, which results in the

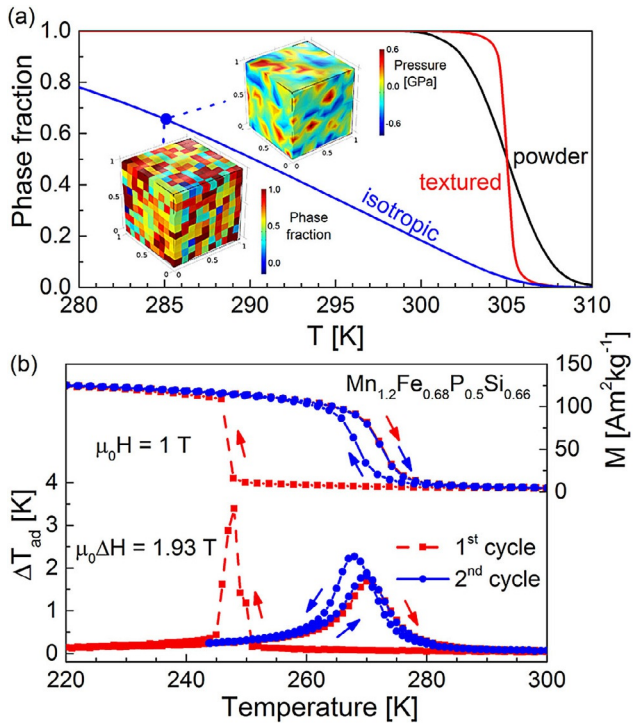

Figure 29. (a) Phase fraction simulation as a function of temperature of a material with anisotropic expansion in powder (black), in textured (red), and in isotropic form (blue). The two images pointing to the blue curve illustrate the evolving stresses and the elemental phase fraction. (b) Magnetization and ΔT_{ad} of $Mn_{1.2}Fe_{0.68}P_{0.5}Si_{0.66}$ as a function of temperature in the first (red) and in the second (blue) cooling and heating cycles. Figure adapted from Ref. [205], used with permission. Original Figure ©Wiley-VCH.

strong deformation of the mesh. The evolving stresses are locally very different, as shown in the second image, reaching values up to 0.6 GPa. These stresses strongly restrict the transformation of the ensemble.

For the anisotropic expansion, the local stress field is so large that a real material cannot bear it and forms cracks (not implemented in the FEM model). The simulation results suggest that the virgin effect in Fe_2P-type materials is due to crack formation in the vicinity of large stresses evolving during the anisotropic expansion in a non-textured material. Recently, the crack formation and propagation was observed by in situ optical microscopy.[59] In Figure 29b, magnetization and direct measurements of ΔT_{ad} in the first and in the second cycles are shown. The magnetic behavior of this sample is comparable to the one of the bulk sample and larger particles shown in Figure 25. Between 245 and 250 K, a sharp jump in the magnetization is observed in the first cooling of the fresh material. In the same temperature range, a large adiabatic temperature change of up to 3.5 K is visible. In the following heating and cooling cycles, the shape of the transformation does not change anymore and it is worth noting that the ΔT_{ad} is much smaller in real operation. In the first cycle, the stresses can be released by the formation of cracks, which takes place both severely and suddenly. Consequently, a large volume fraction of the material transforms in this process, thereby leading to a significant adiabatic temperature change, which we denote as the stress–release caloric effect.[205]

The virgin effect in the material $Mn_{1.2}Fe_{0.68}P_{0.5}Si_{0.66}$ shows impressively the importance of mechanical stress originating in the coupling of neighboring grains through the stresses evolving during the first-order transition. The finite-element-based simulation scheme proved to be a useful tool to deepen the understanding of the interplay between connected fragments of a magnetocaloric material. For cubic–cubic transformations, the sharpening of the transition was clearly demonstrated, which explains the observations obtained in the measurements of single particles in comparison to the bulk material.

6. Dynamical Effects at Magnetostructural Transitions

Using magnetocaloric materials in cooling devices requires that the transformation can follow the field-sweep rate of the device. At the moment, the operating frequency of active magnetic regenerators (AMR) varies between 1–10 Hz.[12] The use of a permanent magnet of 2 T thereby achieves a field-sweep rate between 2 and 20 T s^{-1}.[216,217] In the case of a nonlinear field profile of the cyclic field, it has to be considered that the field-sweep rate can vary across the field profile. Commonly, ΔT_{ad} and ΔS_T are used to assess the suitability of potential magnetocaloric materials. However, these measurements are performed under isothermal, isofield (ΔS_T), or adiabatic (ΔT_{ad}) conditions with slow field-sweep rates of approximately 10 mT s^{-1} and do not show the response under real operating conditions. In the case of second-order magnetic transitions such as in Gd,[218] the spins are aligned along the direction of the applied magnetic fields within the time-range of nanoseconds and can therefore follow the field-sweep rates in real devices. In the case of first-order magnetostructural transitions, the transformation is driven by a nucleation and growth process,[219,220] and the kinetics of these processes can be in the same range or even slower than the operation frequency of the AMR. Therefore, the speed of the transformation can be a critical parameter for the operation frequency. For example, in the elastocaloric material TiNi, Ossmer et al.[221] observed by in situ infrared thermography that the kinetics of the first-order martensite phase transition depend on the applied strain rate. This study therefore shows the importance of investigating the caloric effect under realistic conditions and determining the influence of the field-sweep rate. For the MCE, this is performed by direct ΔT_{ad} measurements with different magnetic-field-sweep rates, which serve to investigate the effect of hysteresis on the dynamical properties of the MCE.

In the following, ΔT_{ad} measurements with field-sweep rates in the range between 10 mT s^{-1} and 1 kT s^{-1} are compared to study the effects of different rates on the MCE in $Ni_{50}Mn_{35}In_{15}$,[43,222] $La(Fe,Si,Co)_{13}$,[223] and Mn_3GaC.[171] The generation of magnetic-field-sweep rates in these ranges requires the use of different devices and magnets. A low field-sweep rate of approximately 10 mT s^{-1} can be generated by

using a superconducting magnet.[16,41,171] For moderate field-sweep rates of approximatey 1 T s^{-1}, either an electromagnet[224,225] or a permanent magnet (nested Halbach magnet)[203] can be used. A rate of about 20 T s^{-1} can be realized by a pneumatic sample holder moving the magnetocaloric material in a static magnetic field.[226] Fast field-sweep rates of up to 1 kT s^{-1} are achieved in pulsed magnetic fields.[222]

The MCE at the martensitic magnetostructural transition in $Ni_{50}Mn_{35}In_{15}$ Heusler alloys is studied by direct ΔT_{ad} measurements at different field-sweep-rates.[227] Figure 30 shows the comparison of ΔT_{ad} as a function of the applied magnetic field. The measurements are performed at about 290 K where most of the sample is in the martensite state and the temperature is close to the transition temperature, so that a field-change of 2 T can induce the transition to the austenite state. A field of 5 T is generated by a pulsed field (1 kT s^{-1}) and a superconducting magnet (11 mT s^{-1}). In the superconducting magnet, the sample cools down immediately after the field is applied, and the cooling rate is almost constant during the entire transformation, which is completed at 3.6 T. In pulsed magnetic fields, a low cooling rate is observed at the beginning of the transformation below 1.2 T. Above 1.2 T, the sample cools down immediately and reaches the same cooling rate as in the superconducting magnet. An immediate cooling with applied field can be also observed in the ΔT_{ad} measurements performed in a nested Halbach magnet, reaching a field of 2 T and a field-sweep rate of 1 T s^{-1}. The cooling rate is the same as in the superconducting magnet. However, the field of 2 T is insufficient to induce a complete transformation to the austenite state, and the sample is in a mixed state at 2 T.

The comparison of the different field-sweep rates shows that in all measurements the same maximum cooling rate is achieved in the middle of the transformation which is therefore independent of the field-sweep rate, at least up to 0.6 kT s^{-1}. However, the lower cooling rate in pulsed fields below 1.2 T compared to the lower field-sweep rate indicates that the cooling behavior at the beginning of the transition is indeed dependent on the field-sweep rate. The transition in Heusler alloys is driven by the nucleation and growth of austenite within the martensite state. Due to the constant cooling rate in the center of the transition, it can be concluded that the growth of the austenite phase by phase-boundary movement is rather fast and can follow the field-sweep rate up to 0.6 kT s^{-1}. But before the growth of the austenite state can progress, new nuclei have to be formed at the beginning of the transformation. Due to the delay of the cooling rate in pulsed magnetic fields, this process seems to be dependent on the field-sweep rate and rather slow compared with the phase-boundary movement. A similar behavior was observed by Xu et al.[228] in a similar Heusler alloy by magnetization measurements in pulsed magnetic fields, showing an increase of the transitional hysteresis with increasing field-sweep rates.

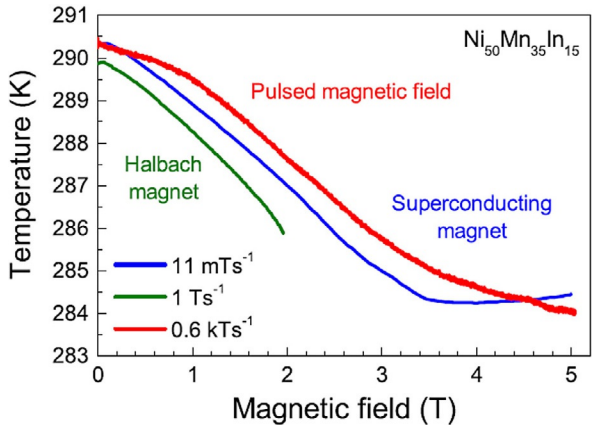

Figure 30. Comparison of ΔT_{ad} as a function of applied magnetic field in $Ni_{50}Mn_{35}In_{15}$ using devices with different field-sweep rates. The measurements are performed in a superconducting magnet (11 mT s^{-1}), a nested Halbach magnet (2 T s^{-1}), and a pulsed field (up to 0.6 kT s^{-1}). Figure adapted from Ref. [227], used with permission. Original Figure ©American Physical Society.

A further increase of the field-sweep rate can be achieved by increasing the magnetic field strength of the pulsed field with constant time duration. Figure 31a shows the field-sweep rate for the pulsed magnetic fields of 2, 5, and 10 T. Due to the constant time duration of the field pulse, the field-sweep rate increases for increasing magnetic field strength. The pulse profile is shown in the inset of Figure 31a. ΔT_{ad} measurements at 286.6 K are performed in field pulses of 2, 5, and 10 T to determine the effect of the field-sweep rate in the range of 0.25 kT s^{-1} (2 T) to 1.5 kT s^{-1} (10 T), and the results are shown in Figure 31b. In all field pulses, cooling is directly observed after applying the field. For the field pulses of 5 and 10 T, a complete transformation to the austenite phase with a ΔT_{ad} of 9 K is observed. However, the field pulse of 2 T is not sufficient to induce a complete transformation and the sample is in a mixed austenite/martensite state at 2 T, leading to a lower ΔT_{ad} compared to the 5 and 10 T pulses. The temperature curves of the 5 and 10 T pulses are equal for field-ranges below 3 T, whereas a deviation of the curves is observed above 3 T. For 5 T the transition is completed at 4.7 T whereas for 10 T the transition finishes at 6 T. The slight warming with a further increase of the magnetic field is related to the conventional MCE of the austenite phase. The effect also leads to slight cooling during the decrease of the field down to 4 T. At approximately 4 T, the reverse transformation to the martensite state starts and the sample heats up again. Due to thermal hysteresis, the transformation is not reversible and the start temperature of 286.6 K cannot be reached. The behaviors of the 5 and 10 T curves are similar for the decreasing field direction whereas a deviation is observed for the increasing field. The different behavior is related to the difference in the field-sweep rates. Figure 31a shows that for the increasing field direction, the 10 T field pulse reaches a much higher field-sweep rate than the 5 T pulse. However, for the decreasing field direction below 4 T the field-sweep rates are the same for both pulses, which explains the coincidence of the temperature curves for the 5 and 10 T for decreasing

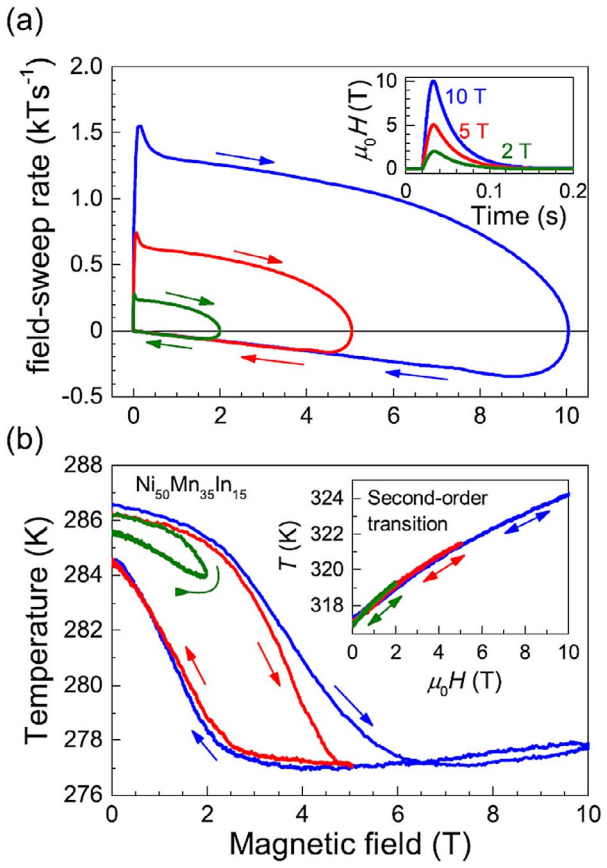

Figure 31. (a) Magnetic-field-sweep rates as a function of magnetic field strength in puled fields. The inset show the field-profile of the field pulse. (b) Field dependence of the absolute temperature for 2, 5, and 10 T field pulses in the vicinity of the first-order transition in $Ni_{50}Mn_{35}In_{15}$. The inset shows the field dependence of the absolute temperature in the vicinity of the second-order transition. Figure adapted from Ref. [227], used with permission. Original Figure ©American Physical Society.

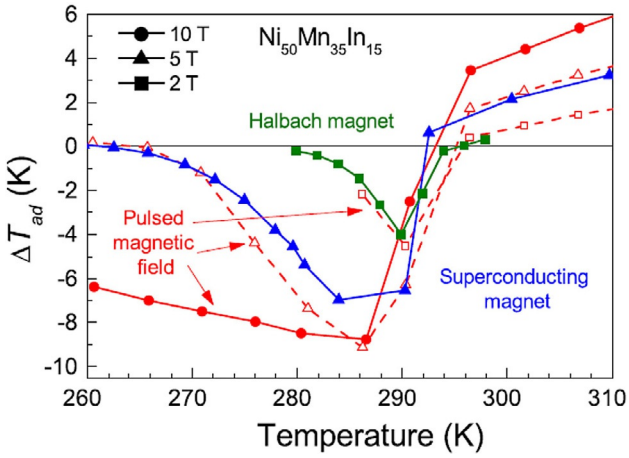

Figure 32. ΔT_{ad} at different target temperatures performed in different experimental setups with different field-sweep rates and maximum field values. Figure adapted from Ref. [227], used with permission. Original Figure ©American Physical Society.

fields. Consequently, the deviation of the two curves for increasing field must be due to kinetic reasons of the martensite-to-austenite transition. The effect is linked to the magnetostructural transition and is absent for the second-order PM-to-FM transition at T_C. This is proven by ΔT_{ad} measurements at 314 K, shown in the inset of Figure 31 b where the temperature curves of decreasing and increasing field coincide.

Figure 32 shows the maximum ΔT_{ad} as a function of temperature measured in the three different experimental setups using magnetic field changes of 2, 5, and 10 T. The field change of 2 T is not sufficient to induce a complete transition, leading to a peak shape of the ΔT_{ad} curve, compared to the plateau-like shape of the ΔT_{ad} curves for higher field change. The measurements in the Halbach magnet coincide with the one performed in pulsed field (2 T). This shows that the maximum ΔT_{ad} value is independent of the field-sweep rate and the transformation can follow the fast rates of the pulsed magnetic field. The field change of 5 T can induce a complete transformation from the martensite to the austenite state, leading to a ΔT_{ad} of 9 K. Due to the complete transformation and the saturation of the MCE, a plateau in the ΔT_{ad} curve is observed. The slight deviation between the measurements in the superconducting magnet and the pulsed magnetic field (5 T) is related to the non-perfect adiabatic conditions in the experiments using the superconducting magnet. The increase of the field change to 10 T enables a field-induced transition even at 260 K and extends the plateau in the ΔT_{ad} curve towards lower temperatures. Since the first-order transition is already completed in 5 T, the maximum ΔT_{ad} cannot be further increased. However, the conventional MCE above 296 K can be improved by increasing the field change.

Despite the slow nucleation process, the martensitic magnetostructural transformation in $Ni_{50}Mn_{35}In_{15}$ Heusler alloys is able to follow even the field-sweep rate of 0.6 kT s^{-1} and can be used in AMR devices with an operation frequency up to 10 Hz. For devices operating at higher frequencies,[229] the kinetics of the first-order transition should be considered. In this case, the performance of a minor loop of the complete transformation can increase the process. In a minor loop, the nucleation of austenite and martensite phases is not required because the sample is at any time in a mixed austenite/martensite state and the transformation can be driven by the rather fast phase-boundary movement.

A slow nucleation process can also be observed in $LaFe_{11.74}Co_{0.13}Si_{1.13}$[223] which has, as with $Ni_{50}Mn_{35}In_{15}$, a first-order transition that can be induced by an external magnetic field. $LaFe_{11.74}Co_{0.13}Si_{1.13}$ shows a transition from a PM to a FM state at 198 K. Field-dependent magnetization measurements under isothermal and adiabatic conditions are performed near the transition temperature. The field-sweep rate of the isothermal measurements is in the range of 5–10 mT s^{-1}, whereas the adiabatic measurements performed in a pulsed field reach a rate up to 8.6 kT s^{-1}.[223] In the case of field-dependent magnetization in pulsed fields, the start of the transition is shifted to higher fields compared to the isothermal measurements. This indicates that the nucleation

process in $LaFe_{11.74}Co_{0.13}Si_{1.13}$ is influenced by the magnetic-field-sweep rate. ΔT_{ad} measurements with field-sweep rates of 2 and 140 T s^{-1} in a 2 T field result in, however, the same maximum ΔT_{ad} showing that the whole transformation process can follow the fast field-sweep rates in pulsed fields. Similar to $Ni_{50}Mn_{35}In_{15}$,[227] the MCE in $LaFe_{11.74}Co_{0.13}Si_{1.13}$ is able to follow a field-sweep-rate of 140 T s^{-1} but a delay of the start of the transformation is observed indicating a slow nucleation process of the first-order transition.

The assumption becomes more evident by comparing isothermal and adiabatic field-dependent magnetization measurements in $LaFe_{11.21}Co_{0.65}Si_{1.11}$. The slight adjustment of the composition leads to a shift of the transition temperature, reaching the critical point where the transition become second order.[230–232] The field-dependent magnetization measurements performed under isothermal and adiabatic conditions show an immediate increase with increasing field. In contrast to the adiabatic measurements in $LaFe_{11.74}Co_{0.13}Si_{1.13}$ with first-order phase transition, no delay of the start of the magnetization is observed. This encourages the assumption that the nucleation process is rather slow compared to the phase-boundary movement. Due to the time-delay, a higher magnetic field in pulsed fields is required to initialize the transformation. In the case of the second-order transition in $LaFe_{11.21}Co_{0.65}Si_{1.11}$, the nucleation process is absent and isothermal and adiabatic measurements show an immediate increase of the magnetization.

A field-sweep rate dependency of the MCE is also observed in Mn_3GaC.[171] The alloy shows an inverse MCE in the vicinity of the isostructural first-order transition at 163 K. Isothermal magnetization measurements are used to calculate a maximum ΔS_T of 14 J kg^{-1} K^{-1} for an applied field of 2 T. Figure 33a shows ΔS_T as a function of the target temperature for a field change of 2 and 5 T. A field change of 2 T is sufficient to induce a complete transformation from the AF to the FM state. The increase of the applied field up to 5 T leads to a shift of the transition towards lower temperatures and enables a complete transformation even at 140 K. The corresponding ΔT_{ad} measurements under adiabatic conditions are shown in Figure 33b. A ΔT_{ad} of −4.7 K is achieved in a field change of 2 T with a field-sweep rate of 700 mT s^{-1}. The plateau of the ΔT_{ad} curve shows that the transformation from the AF to the FM state is complete. A larger field change of 5 T with a field-sweep rate of 11 mT s^{-1} enables a complete transformation at lower temperatures and leads to an extension of the plateau down to 144 K. The maximum value of ΔT_{ad} is similar to the measurements in the setup with 2 T and a field-sweep rate of 700 mT s^{-1} confirming a full AF-to-FM transformation for both field changes. In pulsed magnetic fields of 10 T (1 kT s^{-1}), the plateau is further extended towards lower temperatures but the maximum value of ΔT_{ad} is smaller compared to the measurements with lower field-sweep rates. The reduced MCE in pulsed magnetic fields indicates that the transformation cannot follow the fast field-sweep rate of 1 kT s^{-1}. This can be explained by a slow response-time of the structural transition, which can be related to local strain induced by the coexistence of the AF and the FM phase during the transformation, which differ in their atomic volumes. The presence of local strain is observed by neutron diffraction studies of the magnetic-field-induced transition.[220] Magnetization measurements in the presence of a pressure field show that the pressure is affecting the magnetic transition temperature in Mn_3GaC and can even induce an intermediate magnetic phase, which is not present without pressure.[233,234] This indicates that the first-order phase transition depends on the field-sweep rate of the external magnetic field if the rate is faster than the relaxation time of the material.

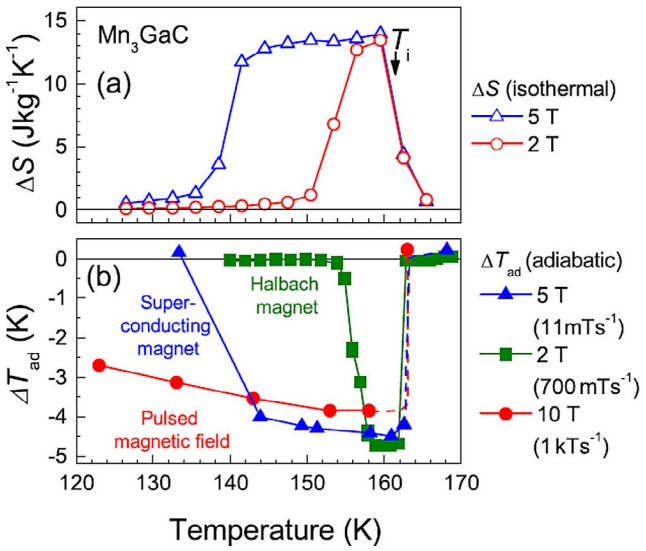

Figure 33. (a) ΔS and (b) ΔT_{ad} at different target temperatures performed under isothermal and adiabatic conditions. The ΔT_{ad} measurements are performed in magnetic fields of 2, 5, and 10 T using different field-sweep rates. Figure adapted from Ref. [171], used with permission. Original Figure ©AIP Publishing.

The comparison of ΔT_{ad} measurements with field-sweep rates in the range from 10 mT s^{-1} to 1 kT s^{-1} have shown that the MCE at first-order transition is indeed affected by the field-sweep rate of the applied magnetic field. However, the effect is different regarding different magnetocaloric materials. In $LaFe_{11.74}Co_{0.13}Si_{1.13}$ and $Ni_{50}Mn_{35}In_{15}$, the dependency on the field-sweep rate is just related to the slow nucleation process. This can be reduced by cycling the transition in a minor loop because the fast phase-boundary movement is able to follow the field-sweep rate up to 1 kT s^{-1}. The maximum ΔT_{ad} in these materials is not affected by the field-sweep rate. In contrast to $LaFe_{11.74}Co_{0.13}Si_{1.13}$ and $Ni_{50}Mn_{35}In_{15}$, the first-order transition in Mn_3GaC is not able to follow the field-sweep rate in pulsed magnetic fields, and the maximum ΔT_{ad} is reduced compared to lower field-sweep rates. The measurements show that the transition process is indeed dependent on the field-sweep rate of the external field. However, the operating frequency of current AMR varies between 1–10 Hz[12] so that the transformation process can follow the field-sweep rate and the maximum ΔT_{ad} is not effected.

7. Conclusions

We have shown that the simple decomposition of the entropy according to contributions from the relevant degrees of freedom yields an essential understanding of their role for the magnetocaloric performance of a material. In particular, for materials, where Fe is an essential component, the combination of experiments (NRIXS) and theory (DFT) has proven to be a perfect couple in resolving element- and site-resolved vibrational properties. In $La(Fe,Si)_{13}$, we could identify that an unexpected strong red-shift of the vibrational density of states VDOS at T_t, which occurs despite the decrease of the lattice constant, is responsible for a significant cooperative vibrational entropy contribution ΔS_{lat} arising from the Fe sites, which has the same sign as ΔS_{el} and ΔS_{mag}. The origin of this favorable coincidence is traced back to the itinerant metamagnetism of the Fe atoms in this compound, which inherently couples all degrees of freedom.

$La(Fe,Si)_{13}$ exhibits a favorably small thermal hysteresis at the phase transition, which however still needs to be better controlled to make the material ready for application. Its origin resides in part in the large volume change ΔV, which causes transformation strain and dissipation. As ΔV is again connected to the itinerant character of the Fe moment, reducing this quantity requires a careful compromise with respect to the intrinsic magnetocaloric properties.

The collaborative interplay of all microscopic degrees of freedom points out the necessity to go beyond the simple decomposition of the entropy change in Equation (2) for a truly quantitative modeling of the magnetocaloric effect in La–Fe–Si-based systems. As the magnetic entropy change calculated in the mean field approximation for a localized spin model with Ising- or Heisenberg-type degrees of freedom already surpasses the total entropy change obtained in experiments,[74] one needs to take into account the itinerant magnetism of Fe explicitly, while including previously neglected cross-coupling terms. Appropriate model descriptions are still to be developed, which require a thorough understanding of the microscopic interactions as laid out in this Review.

The excellent tunability of martensitic Heusler materials offers an interesting perspective for the development of novel inverse magnetocaloric systems. While the structural transformation is essentially determined by the composition through the valence electron concentration e/a, the magnetic properties not only depend on the components but also on the site where a specific element is located. This can be influenced by an appropriate choice of off-stoichiometric compositions or a heat treatment, which influences site disorder. Furthermore, Ni–Mn-based Heusler compounds tend to decompose,[159] which may not be altogether beneficial for a narrow hysteresis. On the other hand, together with the richness in the magnetic exchange coupling between the elements, this gives rise to interesting new phenomena such as shell-ferromagnetism.[235–237] Optimizing the inverse MCE requires painful compromises between a minimized hysteresis, a large magnetization change ΔM, and a large entropy change ΔS, as the magnetic and lattice degrees of freedom work against each other. This is because the low-temperature phase is paramagnetic at the transition point and establishes the dilemma of inverse magnetocaloric Heusler alloys.

Due to the interesting similarities to the Heusler compounds the stoichiometric metamagnetic alloy FeRh may be regarded as a paradigmatic role model for improving inverse magnetocaloric materials. It possesses a very large MCE arising from the cooperative contributions of all degrees of freedom, ΔS_{mag}, ΔS_{lat}, and ΔS_{el}, together with large ΔM and large reversible ΔT_{ad}. The main reason for this is the antiferromagnetic ordered ground state, which has a lower entropy than the FM state at finite temperatures. The essential drawbacks of this system are the large hysteresis, which is again connected to the considerable volume change at the transition and, most importantly, the prohibitively scarce and expensive component Rh. The search for inverse systems with a transition between two ordered phases may, however, result as a promising design goal.

The analysis of the MCE with respect to application-related conditions points out that the evaluation of the reversible temperature and entropy changes upon fast field sweeping is an important issue to be considered for the development of magnetocaloric materials for cooling devices. Even though the reversible entropy and temperature changes can be extracted from $S(T)$ diagrams, the behavior upon fast field cycling can deviate from the predicted values. Therefore, the influence of kinetic effects and microstructural influences on the dynamics of the field-induced phase transition must be considered. Large reversible adiabatic temperature changes can be obtained for the first field application for Heusler alloys. However, the large thermal hysteresis diminishes the reversible effect upon further field cycles drastically. The material families of La–Fe–Si, Fe_2P, and Mn_3GaC are characterized by a narrow thermal hysteresis and show reversible adiabatic temperature changes of 75–90 % for subsequent field cycles compared to the first field application. The partial substitution of C by N for Mn_3GaC shows that a tuning of the phase transition from first- towards second-order character is a way to reduce the thermal hysteresis nearly to zero and enable a completely reversible magnetic field induced phase transition.

As the MCE of a first-order phase transition is connected to a volume change, microstructural stresses and strains occur that can influence the transition behavior for the nucleation and growth process in major as well as minor loops of thermal hysteresis. As the frequencies for an efficiently working magnetocaloric cooling device must be in the range of 1–10 Hz, an analysis of the dynamic characteristics of the phase transition is needed to evaluate its field sweeping rate dependence. For Heusler and first-order La–Fe–Si alloys, the transition can follow even high sweeping rates of pulsed fields up to $1\ kT\,s^{-1}$ as a result of the fast phase boundary movement. As a result, the maximum achievable ΔT_{ad} does not vary for different field rates. However, a dependence of the first nucleation processes on the magnetic field rate can be observed, which is not the case for compositions of La–

Fe–Si showing a second-order transition. On the contrary, the phase transition is kinetically limited in the Mn_3GaC system for fast field-sweep rates and cannot follow the fast-pulsed magnetic field changes. Therefore, the maximum ΔT_{ad} is highly dependent on the sweep rate of the magnetic field. Due to this, it is essential to study the different magnetocaloric materials under realistic conditions of the operating device.

To develop a material system towards applications, also the processing of a magnetocaloric material to be implemented in a working heat exchanger system is a crucial issue. Bonded plates with a thickness well below 300 μm and a large surface area can provide good heat exchange properties. Therefore, the evaluation of the size dependence for several magnetocaloric materials as well as the modeling of the interactions for small particles can provide important information. Stress coupling explains the large width of the transition and the temperature distribution for small Heusler alloy particles, which lead to a sharper phase transition when coupled together in a bulk piece.

To summarize, we achieved a deep understanding of important mechanisms that have significant impact on the performance and hysteresis of magnetocaloric materials. At the same time, it became clear after all these studies that there is still a wealth of fundamental phenomena that remain to be explored and explained. This includes the identification of all relevant intrinsic and extrinsic sources of hysteresis, their microscopic origins, and entanglement on various length (and time) scales. The comprehensive description of these properties will, upon implementation into applications, ultimately lead to efficient magnetic energy conversion materials.

Acknowledgements

This work was supported by DFG (SPP 1599, Grant No. GR3498/3, GU514/6, WE2623/12, AC63/4) and by HLD at HZDR, member of the European Magnetic Field Laboratory (EMFL).

Conflict of interest

The authors declare no conflict of interest.

Keywords: energy conversion · ferroic cooling · magnetocaloric effect · magnetostructural transition · solid-state refrigeration

[1] M. Isaac, D. P. van Vuuren, *Energy Policy* **2009**, *37*, 507–521.
[2] C. Zimm, A. Jastrab, A. Sternberg, V. Pecharsky, K. Geschneidner, Jr, M. Osborne, I. Anderson, *Adv. Cryog. Eng.* **1998**, *43*, 1759.
[3] K. A. Gschneidner, Jr., V. K. Pecharsky, *Annu. Rev. Mater. Sci.* **2000**, *30*, 387.
[4] O. Gutfleisch, M. A. Willard, E. Brück, C. H. Chen, S. G. Sankar, J. P. Liu, *Adv. Mater.* **2011**, *23*, 821.
[5] V. Franco, J. S. Blázquez, J. J. Ipus, J. Y. Law, L. M. Moreno-Ramírez, A. Conde, *Prog, Mater. Sci.* **2018**, *93*, 112.
[6] J. Romero Gómez, R. Ferreiro Garcia, A. De Miguel Catoira, M. Romero Gómez, *Renewable Sustainable Energy Rev.* **2013**, *17*, 74.
[7] G. V. Brown, *J. Appl. Phys.* **1976**, *47*, 3673.
[8] V. K. Pecharsky, K. A. Gschneidner, Jr., *Phys. Rev. Lett.* **1997**, *78*, 4494.
[9] B. F. Yu, Q. Gao, B. Zhang, X. Z. Meng, *Int. J. Refrig.* **2003**, *26*, 622–636.
[10] M. D. Kuz′min, *Phys. Rev. B* **2008**, *77*, 184431.
[11] J. Liu, T. Gottschall, K. P. Skokov, J. D. Moore, O. Gutfleisch, *Nat. Mater.* **2012**, *11*, 620–626.
[12] A. Kitanovski, J. Tušek, U. Tomc, U. Plaznik, M. Ožbolt, A. Poredoš, *Magnetocaloric Energy Conversion—From Theory to Applications*, Springer, Cham, **2014**.
[13] D. Velázquez, C. Estepa, E. Palacios, R. Burriel, *Int. J. Refrig.* **2016**, *63*, 14–24.
[14] V. Provenzano, A. J. Shapiro, R. D. Shull, *Nature* **2004**, *429*, 853.
[15] K. A. Gschneidner, Jr., V. K. Pecharsky, A. O. Tsokol, *Rep. Prog. Phys.* **2005**, *68*, 1479.
[16] I. Titov, M. Acet, M. Farle, D. González-Alonso, L. Mañosa, A. Planes, T. Krenke, *J. Appl. Phys.* **2012**, *112*, 073914.
[17] O. Gutfleisch, T. Gottschall, M. Fries, D. Benke, I. Radulov, K. P. Skokov, H. Wende, M. E. Gruner, M. Acet, P. Entel, M. Farle, *Phil. Trans. R. Soc. A* **2016**, *374*, 20150308.
[18] L. Cohen, *Phys. Status Solidi B* **2018**, *255*, 1700317.
[19] A. M. Tishin, Y. I. Spichkin, *The Magnetocaloric Effect and Its Applications*, Institute of Physics, Bristol, **2003**.
[20] V. I. Zverev, A. M. Tishin, M. D. Kuz′min, *J. Appl. Phys.* **2010**, *107*, 043907.
[21] K. G. Sandeman, *Scr. Mater.* **2012**, *67*, 566.
[22] B. Fultz, *Prog. Mater. Sci.* **2010**, *55*, 247.
[23] M. Wolloch, M. E. Gruner, W. Keune, P. Mohn, J. Redinger, F. Hofer, D. Suess, R. Podloucky, J. Landers, S. Salamon, F. Scheibel, D. Spoddig, R. Witte, B. Roldan Cuenya, O. Gutfeisch, M. Y. Hu, J. Zhao, T. Toellner, E. E. Alp, M. Siewert, P. Entel, R. Pentcheva, H. Wende, *Phys. Rev. B* **2016**, *94*, 174435.
[24] A. Fujita, S. Fujieda, Y. Hasegawa, K. Fukamichi, *Phys. Rev. B* **2003**, *67*, 104416.
[25] M. E. Gruner, W. Keune, B. Roldan Cuenya, C. Weis, J. Landers, S. I. Makarov, D. Klar, M. Y. Hu, E. E. Alp, J. Zhao, M. Krautz, O. Gutfleisch, H. Wende, *Phys. Rev. Lett.* **2015**, *114*, 057202.
[26] Z. Gercsi, N. Fuller, K. G. Sandeman, A. Fujita, *J. Phys. D* **2018**, *51*, 034003.
[27] C. P. Opeil, B. Mihaila, R. K. Schulze, L. Mañosa, A. Planes, W. L. Hults, R. A. Fisher, P. S. Riseborough, P. B. Littlewood, J. L. Smith, J. C. Lashley, *Phys. Rev. Lett.* **2008**, *100*, 165703.
[28] H. Wende, *Rep. Prog. Phys.* **2004**, *67*, 2105–2181.
[29] H. J. Elmers, *Element-Specific Magnetic and Electronic Properties of Epitaxial Heusler Films-Heusler Alloys* (Eds.: C. Felser, A. Hirohata), Springer Series in Materials Science, Cham, **2016**, pp. 353–386.
[30] A. Rogalev, K. Ollefs, F. Wilhelm, *X-Ray Magnetic Circular Dichroism-X-Ray Absorption and X-Ray Emission Spectroscopy: Theory and Applications* (Eds.: J. A. Van Bokhoven, C. Lamberti), Wiley, Chichester, **2016**.
[31] G. van der Laan, A. I. Figueroa, *Coord. Chem. Rev.* **2014**, *277–278*, 95–129.
[32] E. Lovell, L. Ghivelder, A. Nicotina, J. Turcaud, M. Bratko, A. D. Caplin, V. Basso, A. Barcza, M. Katter, L. F. Cohen, *Phys. Rev. B* **2016**, *94*, 134405.
[33] S. Ener, J. Neuhaus, W. Petry, R. Mole, K. Hradil, M. Siewert, M. E. Gruner, P. Entel, I. Titov, M. Acet, *Phys. Rev. B* **2012**, *86*, 144305.
[34] P. J. Stonaha, M. E. Manley, N. M. Bruno, I. Karaman, R. Arroyave, N. Singh, D. L. Abernathy, S. Chi, *Phys. Rev. B* **2015**, *92*, 140406(R).
[35] J. Landers, S. Salamon, W. Keune, M. E. Gruner, M. Krautz, J. Zhao, M. Y. Hu, T. S. Toellner, E. E. Alp, O. Gutfleisch, H. Wende, *Phys. Rev. B* **2018**, *98*, 024417.
[36] M. A. Uijttewaal, T. Hickel, J. Neugebauer, M. E. Gruner, P. Entel, *Phys. Rev. Lett.* **2009**, *102*, 035702.
[37] S. Ener, T. Mehaddene, B. Pedersen, M. Leitner, J. Neuhaus, W. Petry, *New J. Phys.* **2013**, *15*, 123016.
[38] B. Dutta, A. Çakır, C. Giacobbe, A. Al-Zubi, T. Hickel, M. Acet, J. Neugebauer, *Phys. Rev. Lett.* **2016**, *116*, 025503.

[39] M. E. Gruner, W. Keune, J. Landers, S. Salamon, M. Krautz, J. Zhao, M. Y. Hu, T. Toellner, E. E. Alp, O. Gutfleisch, H. Wende, *Phys. Status Solidi B* **2018**, *255*, 1700465.
[40] G. Grimvall, *Thermophysical Properties of Materials, Vol. 18*, North Holland, Amsterdam, **1986**.
[41] Ö. Çakır, M. Acet, *Appl. Phys. Lett.* **2012**, *100*, 202404.
[42] T. Kihara, X. Xu, W. Ito, R. Kainuma, M. Tokunaga, *Phys. Rev. B* **2014**, *90*, 214409.
[43] T. Gottschall, K. P. Skokov, D. Benke, M. E. Gruner, O. Gutfleisch, *Phys. Rev. B* **2016**, *93*, 184431.
[44] V. D. Buchelnikov, P. Entel, S. V. Taskaev, V. V. Sokolovskiy, A. Hucht, M. Ogura, H. Akai, M. E. Gruner, S. K. Nayak, *Phys. Rev. B* **2008**, *78*, 184427.
[45] V. Sokolovskiy, V. Buchelnikov, K. Skokov, O. Gutfleisch, D. Karpenkov, Yu. Koshkid'ko, H. Miki, I. Dubenko, N. Ali, S. Stadler, V. Khovaylo, *J. Appl. Phys.* **2013**, *114*, 183913.
[46] F. Körmann, A. Dick, T. Hickel, J. Neugebauer, *Phys. Rev. B* **2011**, *83*, 165114.
[47] A. Dick, F. Körmann, T. Hickel, J. Neugebauer, *Phys. Rev.* **2011**, 84, 125101.
[48] T. Mukherjee, S. Michalski, R. Skomski, D. J. Sellmyer, C. Binek, *Phys. Rev. B* **2011**, *83*, 214413.
[49] A. Planes, L. Mañosa, M. Acet, *J. Phys. Condens. Matter* **2009**, *21*, 233201.
[50] A. Fujita, S. Fujieda, K. Fukamichi, H. Mitamura, T. Goto, *Phys. Rev. B* **2001**, *65*, 014410.
[51] M. D. Kuz′min, M. Richter, *Phys. Rev. B* **2007**, *76*, 092401.
[52] A. Fujita, H. Yako, *Scr. Mater.* **2012**, *67*, 578.
[53] O. Delaire, M. S. Lucas, J. A. Muñoz, M. Kresch, B. Fultz, *Phys. Rev. Lett.* **2008**, *101*, 105504.
[54] O. Delaire, K. Marty, M. B. Stone, P. R. C. Kent, M. S. Lucas, D. L. Abernathy, D. Mandrus, B. C. Sales, *Proc. Natl. Acad. Sci. USA* **2011**, *108*, 4725.
[55] J. A. Muñoz, M. S. Lucas, O. Delaire, M. L. Winterrose, L. Mauger, C. W. Li, A. O. Sheets, M. B. Stone, D. L. Abernathy, Y. Xiao, P. Chow, B. Fultz, *Phys. Rev. Lett.* **2011**, *107*, 115501.
[56] N. H. Dung, Z. Q. Ou, L. Caron, L. Zhang, D. T. Cam Thanh, G. A. de Wijs, R. A. de Groot, K. H. J. Buschow, E. Brück, *Adv. Energy Mater.* **2011**, *1*, 1215.
[57] M. F. J. Boeije, P. Roy, F. Guillou, H. Yibole, X. Miao, L. Caron, D. Banerjee, N. H. van Dijk, R. A. de Groot, E. Brück, *Chem. Mater.* **2016**, *28*, 4901.
[58] E. Brück, H. Yibole, V. T. Nguyen, X. Miao, M. Boeije, N. van Dijk, *Solid State Phenom.* **2016**, *257*, 129.
[59] M. Fries, L. Pfeuffer, E. Bruder, T. Gottschall, S. Ener, L. V. B. Diop, T. Gröb, K. P. Skokov, O. Gutfleisch, *Acta Mater.* **2017**, *132*, 222.
[60] M. Krautz, K. Skokov, T. Gottschall, C. S. Teixeira, A. Waske, J. Liu, L. Schultz, O. Gutfleisch, *J. Alloys Compd.* **2014**, *598*, 27.
[61] A. Barcza, M. Katter, V. Zellmann, S. Russek, S. Jacobs, C. Zimm, *IEEE Trans. Magn.* **2011**, *47*, 3391.
[62] K. Morrison, J. Lyubina, J. Moore, K. Sandeman, O. Gutfleisch, L. Cohen, A. Caplin, *Philos. Mag.* **2012**, *92*, 292.
[63] R. Gauß, G. Homm, O. Gutfleisch, *J. Ind. Ecol.* **2016**, *21*, 1291–1300.
[64] A. Waske, M. E. Gruner, T. Gottschall, O. Gutfleisch, *MRS Bull.* **2018**, *43*, 269.
[65] H. Chang, J. Linag, B.-G. Shen, L.-T. Yang, F. Wang, N.-X. Chen, G.-H. Rao, *J. Phys. D* **2003**, *36*, 160.
[66] H. H. Hamdeh, H. Al-Ghanem, W. M. Hikal, S. M. Taher, J. C. Ho, D. T. K. Anh, N. P. Thuy, N. H. Duc, P. D. Thang, *J. Magn. Magn. Mater.* **2004**, *269*, 404.
[67] M. Rosca, M. Balli, D. Fruchard, D. Gignoux, E. K. Hlil, S. Miraglia, B. Ouladdiaf, P. Wolfers, *J. Alloys Compd.* **2010**, *490*, 50.
[68] F. - *x.* Hu, B.-g. Shen, J.-r. Sun, Z.-h. Cheng, G.-h. Rao, X.–*x.* Zhang, *Appl. Phys. Lett.* **2001**, *78*, 3675.
[69] A. Fujita, K. Fukamichi, *IEEE Trans. Magn.* **1999**, *35*, 3796.
[70] E. F. Wassermann, *Invar: Moment-Volume Instabilities in Transition Metals and Alloys in: Ferromagnetic Materials, Vol. 5* (Eds.: K. H. J. Buschow, E. P. Wohlfahrt), Elsevier, Amsterdam, **1990**, pp. 237–322.
[71] V. L. Moruzzi, *Phys. Rev. B* **1990**, *41*, 6939.
[72] P. Mohn, K. Schwarz, D. Wagner, *Phys. Rev. B* **1991**, *43*, 3318.
[73] P. Entel, E. Hoffmann, P. Mohn, K. Schwarz, V. L. Moruzzi, *Phys. Rev. B* **1993**, *47*, 8706.
[74] L. Jia, G. J. Liu, J. R. Sun, H. W. Zhang, F. X. Hu, C. Dong, G. H. Rao, B. G. Shen, *J. Appl. Phys.* **2006**, *100*, 123904.
[75] P. J. von Ranke, N. A. de Oliveira, C. Mello, A. Magnus, G. Carvalho, S. Gama, *Phys. Rev. B* **2005**, *71*, 054410.
[76] M. Piazzi, C. Benati, C. Curcio, M. Kuepferling, V. Basso, *J. Magn. Magn. Mater.* **2016**, *400*, 349.
[77] V. Basso, M. Piazzi, C. Bennati, C. Curcio, *Phys. Status Solidi B* **2018**, *255*, 1700278.
[78] T. S. Toellner, *Hyperfine Interact.* **2000**, *125*, 3.
[79] G. Kresse, D. Joubert, *Phys. Rev. B* **1999**, *59*, 1758.
[80] G. Kresse, J. Furthmüller, *Phys. Rev. B* **1996**, *54*, 11169.
[81] D. Alfè, *Comput. Phys. Commun.* **2009**, *180*, 2622.
[82] V. L. Moruzzi, P. M. Marcus, K. Schwarz, P. Mohn, *Phys. Rev. B* **1986**, *34*, 1784.
[83] C. P. Bean, D. S. Rodbell, *Phys. Rev.* **1962**, *126*, 104.
[84] H. Yamada, *Phys. B* **2007**, *391*, 42.
[85] Y. Sutou, Y. Imano, N. Koeda, T. Omori, R. Kainuma, K. Ishida, K. Oikawa, *Appl. Phys. Lett.* **2004**, *85*, 4358.
[86] T. Krenke, E. Duman, M. Acet, E. F. Wassermann, X. Moya, L. Mañosa, A. Planes, *Nat. Mater.* **2005**, *4*, 450.
[87] R. Kainuma, W. Ito, R. Y. Umetsu, K. Oikawa, K. Ishida, *Appl. Phys. Lett.* **2008**, *93*, 091906.
[88] I. Dubenko, M. Khan, A. K. Pathak, B. R. Gautam, S. Stadler, N. Ali, *J. Magn. Magn. Mater.* **2009**, *321*, 754.
[89] P. J. Webster, K. R. A. Ziebeck, S. L. Town, M. S. Peak, *Philos Mag. B* **1984**, *49*, 295.
[90] T. Graf, C. Felser, S. S. Parkin, *Prog. Solid State Chem.* **2011**, *39*, 1.
[91] T. Krenke, M. Acet, E. F. Wassermann, X. Moya, L. Mañosa, A. Planes, *Phys. Rev. B* **2006**, *73*, 174413.
[92] W. Ito, Y. Imano, R. Kainuma, Y. Sutou, K. Oikawa, K. Ishida, *Metall. Mater. Trans.* **2007**, *38*, 759.
[93] J. Enkovaara, A. Ayuela, J. Jalkanen, L. Nordström, R. M. Nieminen, *Phys. Rev. B* **2003**, *67*, 054417.
[94] A. Chirkova, K. Skokov, L. Schultz, N. Baranov, O. Gutfleisch, T. Woodcock, *Acta Mater.* **2016**, *106*, 15.
[95] V. I. Zverev, A. M. Saletsky, R. R. Gimaev, A. M. Tishin, T. Miyanaga, J. B. Staunton, *Appl. Phys. Lett.* **2016**, *108*, 192405.
[96] M. Annaorazov, K. Asatryan, G. Myalikgulyev, S. Nikitin, A. Tishin, A. Tyurin, *Cryogenics* **1992**, *32*, 867.
[97] M. Fallot, *Ann. Phys.* **1938**, *11*, 291.
[98] M. Fallot, R. Hocart, *Rev. Sci. (Paris)* **1939**, *77*, 498.
[99] G. Shirane, C. W. Chen, P. A. Flinn, R. Nathans, *Phys. Rev.* **1963**, *131*, 183.
[100] G. Shirane, R. Nathans, C. W. Chen, *Phys. Rev.* **1964**, *134*, A1547.
[101] L. H. Lewis, C. H. Marrows, S. Langridge, *J. Phys. D* **2016**, *49*, 323002.
[102] U. Aschauer, R. Braddell, S. A. Brechbühl, P. M. Derlet, N. A. Spaldin, *Phys. Rev. B* **2016**, *94*, 014109.
[103] N. A. Zarkevich, D. D. Johnson, *Phys. Rev. B* **2018**, *97*, 014202.
[104] J. Kim, R. Ramesh, N. Kioussis, *Phys. Rev. B* **2016**, *94*, 180407.
[105] A. Zheludev, S. Shapiro, P. Wochner, L. Tanner, *Phys. Rev. B* **1996**, *54*, 15045.
[106] A. T. Zayak, P. Entel, J. Enkovaara, A. Ayuela, R. M. Nieminen, *Phys. Rev. B* **2003**, *68*, 132402.
[107] M. Siewert, M. E. Gruner, A. Hucht, H. C. Herper, A. Dannenberg, A. Chakrabarti, N. Singh, R. Arróyave, P. Entel, *Adv. Eng. Mater.* **2012**, *14*, 530.
[108] T. Hickel, M. Uijttewaal, A. Al-Zubi, B. Dutta, B. Grabowski, J. Neugebauer, *Adv. Eng. Mater.* **2012**, *14*, 547.
[109] R. Niemann, U. K. Rößler, M. E. Gruner, O. Heczko, L. Schultz, S. Fähler, *Adv. Eng. Mater.* **2012**, *14*, 562.
[110] M. E. Gruner, S. Fähler, P. Entel, *Phys. Status Solidi B* **2014**, *251*, 2067.
[111] A. Kundu, M. E. Gruner, M. Siewert, A. Hucht, P. Entel, S. Ghosh, *Phys. Rev. B* **2017**, *96*, 064107.
[112] M. E. Gruner, R. Niemann, P. Entel, R. Pentcheva, U. K. Rößler, K. Nielsch, S. Fähler, *Sci. Rep.* **2018**, *8*, 8489.

[113] R. Witte, R. Kruk, M. E. Gruner, R. A. Brand, D. Wang, S. Schlabach, A. Beck, V. Provenzano, R. Pentcheva, H. Wende, H. Hahn, *Phys. Rev. B* **2016**, *93*, 104416.
[114] S. A. Nikitin, G. Myalikgulyev, A. M. Tishin, M. P. Annaorazov, K. A. Asatryan, A. L. Tyurin, *Phys. Lett. A* **1990**, *148*, 363–366.
[115] M. Manekar, S. B. Roy, *J. Phys. D* **2008**, *41*, 192004.
[116] J. S. Kouvel, *J. Appl. Phys.* **1966**, *37*, 1257.
[117] J. M. Lommel, *J. Appl. Phys.* **1969**, *40*, 3880.
[118] J. B. McKinnon, D. Melville, E. W. Lee, *J. Phys. C* **1970**, *3*, S46.
[119] M. P. Annaorazov, S. A. Nikitin, A. L. Tyurin, K. A. Asatryan, A. K. Dovletov, *J. Appl. Phys.* **1996**, *79*, 1689.
[120] G. Nikitin, S. A. Myalikgulev, M. P. Annaorazon, A. Tyurin, R. W. Myndyev, S. A. Akopyan, *Phys. Lett. A* **1992**, *171*, 234.
[121] E. Stern-Taulats, A. Planes, P. Lloveras, M. Barrio, J.-L. Tamarit, S. Pramanick, S. Majumdar, C. Frontera, L. Mañosa, *Phys. Rev. B* **2014**, *89*, 214105.
[122] E. Stern-Taulats, A. Gracia-Condal, A. Planes, P. Lloveras, M. Barrio, J. Tamarit, S. Pramanick, S. Majumdar, L. Mañosa, *Appl. Phys. Lett.* **2015**, *107*, 152409.
[123] Y. Liu, L. C. Phillips, R. Mattana, M. Bibes, A. Barthélémy, B. Dkhil, *Nat. Commun.* **2016**, *7*, 11614.
[124] P. Tu, A. J. Heeger, J. S. Kouvel, J. B. Comly, *J. Appl. Phys.* **1969**, *40*, 1368.
[125] J. Ivarsson, G. Pickett, J. Tóth, *Phys. Lett. A* **1971**, *35*, 167.
[126] B. Fogarassy, T. Kemény, L. Pál, J. Tóth, *Phys. Rev. Lett.* **1972**, *29*, 288.
[127] D. W. Cooke, F. Hellman, C. Baldasseroni, C. Bordel, S. Moyerman, E. E. Fullerton, *Phys. Rev. Lett.* **2012**, *109*, 255901.
[128] A. Deák, E. Simon, L. Balogh, L. Szunyogh, M. dos Santos Dias, J. B. Staunton, *Phys. Rev. B* **2014**, *89*, 224401.
[129] S. Polesya, S. Mankovsky, D. Ködderitzsch, J. Minár, H. Ebert, *Phys. Rev. B* **2016**, *93*, 024423.
[130] L. M. Sandratskii, P. Mavropoulos, *Phys. Rev. B* **2011**, *83*, 174408.
[131] R. Y. Gu, V. P. Antropov, *Phys. Rev. B* **2005**, *72*, 012403.
[132] M. E. Gruner, E. Hoffmann, P. Entel, *Phys. Rev. B* **2003**, *67*, 064415.
[133] A. I. Zakharov, A. M. Kadomtseva, R. Z. Levitin, E. G. Ponyatovskii, *Sov. Phys. JETP* **1964**, *19*, 1348.
[134] M. Richardson, D. Melville, J. Ricodeau, *Phys. Lett. A* **1973**, *46*, 153 http://www.jetp.ac.ru/cgi-bin/e/index/e/36/1/p105?a=list.
[135] B. K. Ponomarev, *Sov. Phys. JETP* **1973**, *36*, 105 .
[136] K. Uebayashi, H. Shimizu, H. Yamada, *Mater. Trans.* **2006**, *47*, 456.
[137] J. B. Staunton, R. Banerjee, M. dos Santos Dias, A. Deak, L. Szunyogh, *Phys. Rev. B* **2014**, *89*, 054427.
[138] T. Krenke, M. Acet, E. F. Wassermann, X. Moya, L. Mañosa, A. Planes, *Phys. Rev. B* **2005**, *72*, 014412.
[139] R. Y. Umetsu, R. Kainuma, Y. Amako Y. Taniguchi, T. Kanomata, K. Fukushima, A. Fujita, K. Oikawa, K. Ishida, *Appl. Phys. Lett.* **2008**, *93*, 042509.
[140] V. V. Khovaylo, T. Kanomata, T. Tanaka, M. Nakashima, Y. Amako, R. Kainuma, R. Y. Umetsu, H. Morito, H. Miki, *Phys. Rev. B* **2009**, *80*, 144409.
[141] S. Aksoy, M. Acet, P. P. Deen, L. Manõsa, A. Planes, *Phys. Rev. B* **2009**, *79*, 212401.
[142] S. Aksoy, O. Posth, M. Acet, R. Meckenstock, J. Lindner, M. Farle, E. F. Wassermann, *J. Phys. Conf. Ser.* **2010**, *200*, 092001.
[143] K. Ollefs, C. Schöppner, I. Titov, R. Meckenstock, F. Wilhelm, A. Rogalev, J. Liu, O. Gutfleisch, M. Farle, H. Wende, M. Acet, *Phys. Rev. B* **2015**, *92*, 224429.
[144] A. I. Liechtenstein, M. I. Katsnelson, V. P. Antropov, V. A. Gubanov, *J. Magn. Magn. Mater.* **1987**, *67*, 65.
[145] H. Ebert, *Fully Relativistic Band Structure Calculations for Magnetic Solids—Formalism and Application, in: Electronic Structure and Physical Properties of Solids. Lecture Notes in Physics*, Vol. 535 (Ed.: H Dreyssé), Springer, Berlin, **2000**, p 191.
[146] LMU Munich Department Chemie AK H. Ebert, *Munich SPRKKR band structure program package*, **2017**, http://ebert.cup.uni-muenchen.de/SPRKKR, accessed 11 June 2018.
[147] A. V. Ruban, I. A. Abrikosov, *Rep. Prog. Phys.* **2008**, *71*, 046501.
[148] E. Şaşioğlu, L. M. Sandratskii, P. Bruno, *Phys. Rev. B* **2004**, *70*, 024427.
[149] Y. Kurtulus, R. Dronskowski, G. D. Samolyuk, V. P. Antropov, *Phys. Rev. B* **2005**, *71*, 014425.
[150] E. Şaşıoğlu, L. M. Sandratskii, P. Bruno, I. Galanakis, *Phys. Rev. B* **2005**, *72*, 184415.
[151] J. Rusz, L. Bergqvist, J. Kudrnovský, I. Turek, *Phys. Rev. B* **2006**, *73*, 214412.
[152] E. Şaşıoğlu, L. M. Sandratskii, P. Bruno, *Phys. Rev. B* **2008**, *77*, 064417.
[153] V. V. Sokolovskiy, V. D. Buchelnikov, M. A. Zagrebin, P. Entel, S. Sahoo, M. Ogura, *Phys. Rev. B* **2012**, *86*, 134418.
[154] D. Comtesse, M. E. Gruner, M. Ogura, V. V. Sokolovskiy, V. D. Buchelnikov, A. Grünebohm, R. Arróyave, N. Singh, T. Gottschall, O. Gutfleisch, V. A. Chernenko, F. Albertini, S. Fähler, P. Entel, *Phys. Rev. B* **2014**, *89*, 184403.
[155] V. Sokolovskiy, A. Grünebohm, V. Buchelnikov, P. Entel, *Entropy* **2014**, *16*, 4992–5019.
[156] P. Entel, M. E. Gruner, D. Comtesse, V. V. Sokolovskiy, V. D. Buchelnikov, *Phys. Status Solidi B* **2014**, *251*, 2135–2148.
[157] P. Neibecker, M. E. Gruner, X. Xu, R. Kainuma, W. Petry, R. Pentcheva, M. Leitner, *Phys. Rev. B* **2017**, *96*, 165131.
[158] P. Entel, A. Talapatra, R. Arroyave, N. Singh, M. E. Gruner, R. Dronskowski, D. Bogdanovski, A. Hucht, *Adv. Sci. Technol.* **2017**, *97*, 124–133.
[159] P. Entel, M. E. Gruner, S. Fähler, M. Acet, A. Çakır, R. Arróyave, S. Sahoo, T. C. Duong, A. Talapatra, L. Sandratskii, S. Mankowsky, T. Gottschall, O. Gutfleisch, P. Lázpita, V. A. Chernenko, J. M. Barandiaran, V. V. Sokolovskiy, V. D. Buchelnikov, *Phys. Status Solidi B* **2018**, *255*, 1870108.
[160] B. Schleicher, D. Klar, K. Ollefs, A. Diestel, D. Walecki, E. Weschke, L. Schultz, K. Nielsch, S. Fähler, H. Wende, M. E. Gruner, *J. Phys. D* **2017**, *50*, 465005.
[161] V. D. Buchelnikov, V. V. Sokolovskiy, H. C. Herper, H. Ebert, M. E. Gruner, S. V. Taskaev, V. V. Khovaylo, A. Hucht, A. Dannenberg, M. Ogura, H. Akai, M. Acet, P. Entel, *Phys. Rev. B* **2010**, *81*, 094411.
[162] I. Galanakis, E. Sasioglu, *Appl. Phys. Lett.* **2011**, *98*, 102514.
[163] R. Kainuma, R. Y. Umetsu, *Ni-Mn-X Heusler Materials, in: Disorder and Strain-Induced Complexity in Functional Materials, Springer Series in Materials Science, Vol. 148* (Eds.: T. Kakeshita, T. Fukuda, A. Saxena, A. Planes), **2012**, Springer, Heidelberg, p. 49–65.
[164] B. Dutta, F. Körmann, T. Hickel, J. Neugebauer, *Phys. Status Solidi B* **2018**, *255*, 1700455.
[165] J.-P. Bouchaud, R. Fruchart, R. Pauthenet, M. Cuillot, H. Bartholin, F. Chaissé, *J. Appl. Phys.* **1966**, *37*, 971.
[166] D. Fruchart, E. F. Bertaut, *J. Phys. Soc. Jpn.* **1978**, *44*, 781.
[167] P. l'Heritier, D. Boursier, R. Fruchart, D. Fruchart, *Mater. Res. Bull.* **1979**, *14*, 1203.
[168] T. Tohei, H. Wada, T. Kanomata, *J. Magn. Magn. Mater.* **2004**, *272–276*, E585–E586.
[169] B. S. Wang, P. Tong, Y. P. Sun, W. Tang, L. J. Li, X. B. Zhu, Z. R. Yang, W. H. Song, *Phys. B* **2010**, *405*, 2427.
[170] B. S. Wang, C. C. Li, J. C. Lin, L. J. Li, P. Tong, X. B. Zhu, Z. R. Yang, W. H. Song, J. M. Dai, Y. P. Sun, *J. Magn. Magn. Mater.* **2011**, *323*, 2017.
[171] F. Scheibel, T. Gottschall, K. Skokov, O. Gutfleisch, M. Ghorbani-Zavareh, Y. Skourski, J. Wosnitza, Ö. Çakır, M. Farle, M. Acet, *J. Appl. Phys.* **2015**, *117*, 233902.
[172] Ö. Çakır, M. Acet, *J. Magn. Magn. Mater.* **2013**, *344*, 207.
[173] Ö. Çakır, M. Acet, M. Farle, A. Wildes, *J. Phys. Condens. Matter* **2016**, *28*, 13LT02.
[174] "A green magnetic cooling device built using upcycled NdFeB magnets": D. Benke, J. Wortmann, M. Pabst, T. Gottschall, I. Radulov, K. Skokov, D. Prosperi, A. Bevan, S. Dove, G. Furlan, C. Tudor, P. Afiuny, M. Zakotnik, O. Gutfleisch, *MagNews*, UK Magnetic Society, **2017**, *3*, 24–27.
[175] O. Gutfleisch, A. Yan, K.-H. Müller, *J. Appl. Phys.* **2005**, *97*, 10M305.
[176] J. Liu, J. Moore, K. Skokov, M. Krautz, K. Löwe, A. Barcza, M. Katter, O. Gutfleisch, *Scripta Mater.* **2012**, *67*, 584.
[177] K. P. Skokov, K. H. Müller, J. D. Moore, J. Liu, A. Y. Karpenkov, M. Krautz, O. Gutfleisch, *J. Alloys Compd.* **2013**, *552*, 310.

[178] L. Mañosa, D. Gonzáles-Alonso, A. Planes, M. Barrio, J.-L. Tamarit, I. S. Titov, M. Acet, A. Bhattacharyya, S. Majumdar, *Nat. Commun.* **2011**, *2*, 595.
[179] H. Sepehri-Amin, A. Taubel, T. Ohkubo, K. P. Skokov, O. Gutfleisch, K. Hono, *Acta Mater.* **2018**, *147*, 342–349.
[180] S. Aksoy, T. Krenke, M. Acet, E. F. Wassermann, X. Moya, L. Mañosa, A. Planes, *Appl. Phys. Lett.* **2007**, *91*, 241916.
[181] X. Moya, L. Mañosa, A. Planes, S. Aksoy, M. Acet, E. F. Wassermann, T. Krenke, *Phys. Rev. B* **2007**, *75*, 184412.
[182] V. V. Khovaylo, K. P. Skokov, O. Gutfleisch, H. Miki, R. Kainuma, T. Kanomata, *Appl. Phys. Lett.* **2010**, *97*, 052503.
[183] K. P. Skokov, V. V. Khovaylo, K.-H. Müller, J. D. Moore, J. Liu, O. Gutfleisch, *J. Appl. Phys.* **2012**, *111*, 07A910.
[184] V. Khovaylo, M. Lyange, K. Skokov, O. Gutfleisch, R. Chatterjee, X. Xu, R. Kainuma, *Mater. Sci. Forum* **2013**, *738–739*, 446–450.
[185] T. Gottschall, K. P. Skokov, B. Frincu, O. Gutfleisch, *Appl. Phys. Lett.* **2015**, *106*, 021901.
[186] A. Taubel, T. Gottschall, M. Fries, S. Riegg, C. Soon, K. P. Skokov, O. Gutfleisch, *Phys. Status Solidi B* **2018**, *255*, 1700331.
[187] P. J. Shamberger, F. S. Ohuchi, *Phys. Rev. B* **2009**, *79*, 144407.
[188] V. V. Khovaylo, K. Skokov, O. Gutfleisch, H. Miki, T. Takagi, T. Kanomata, V. V. Koledov, V. G. Shavrov, G. Wang, E. Palacios, J. Bartolomé, R. Burriel, *Phys. Rev. B* **2010**, *81*, 214406.
[189] V. Basso, C. P. Sasso, K. P. Skokov, O. Gutfleisch, V. V. Khovaylo, *Phys. Rev. B* **2012**, *85*, 014430.
[190] T. Gottschall, E. Stern-Taulats, L. Mañosa, A. Planes, K. P. Skokov, O. Gutfleisch, *Appl. Phys. Lett.* **2017**, *110*, 223904.
[191] T. Gottschall, K. P. Skokov, R. Burriel, O. Gutfleisch, *Acta Mater.* **2016**, *107*, 1.
[192] E. Stern-Taulats, A. Planes, P. Lloveras, M. Barrio, J.-L. Tamarit, S. Pramanick, S. Majumdar, S. Yüce, B. Emre, C. Frontera, L. Mañosa, *Acta Mater.* **2015**, *96*, 324.
[193] R. Niemann, S. Hahn, A. Diestel, A. Backen, L. Schultz, K. Nielsch, M. F.-X. Wagner, S. Fähler, *APL Mater.* **2016**, *4*, 064101.
[194] T. Kanomata, H. Yasui, T. Kaneko, *Phys. Status Solidi* **1991**, *126*, K83.
[195] K. Kamishima, T. Goto, T. Kanomata, M. I. Bartashevich, *J. Magn. Magn. Mater.* **1998**, *177*, 587.
[196] H. Fujii, T. Hokabe, T. Kamigaichi, T. Okamoto, *J. Phys. Soc. Jpn.* **1977**, *43*, 41.
[197] O. Beckman, L. Lundgren, P. Nordblad, P. Svedlindh, A. Törne, Y. Andersson, S. Rundqvist, *Phys. Scr.* **1982**, *25*, 679.
[198] A. Yan, K. H. Müller, L. Schultz, O. Gutfleisch, *J. Appl. Phys.* **2006**, *99*, 08K903.
[199] H. Yibole, F. Guillou, L. Zhang, N. H. van Dijk, E. Brück, *J. Phys. D* **2014**, *47*, 075002.
[200] F. Guillou, G. Porcari, H. Yibole, N. van Dijk, E. Brück, *Adv. Mater.* **2014**, *26*, 2671.
[201] A. Bartok, M. Kustov, L. F. Cohen, A. Pasko, K. Zehani, L. Bessais, F. Mazaleyrat, M. LoBue, *J. Magn. Magn. Mater.* **2016**, *400*, 333.
[202] J. D. Moore, D. Klemm, D. Lindackers, S. Grasemann, R. Träger, J. Eckert, L. Löber, S. Scudino, M. Katter, A. Barcza, K. P. Skokov, O. Gutfleisch, *J. Appl. Phys.* **2013**, *114*, 043907.
[203] K. P. Skokov, D. Yu. Karpenkov, M. D. Kuz′min, I. A. Radulov, T. Gottschall, B. Kaeswurm, M. Fries, O. Gutfleisch, *J. Appl. Phys.* **2014**, *115*, 17A941.
[204] M. D. Kuz′min, *Appl. Phys. Lett.* **2007**, *90*, 251916.
[205] T. Gottschall, D. Benke, M. Fries, A. Taubel, I. A. Radulov, K. P. Skokov, O. Gutfleisch, *Adv. Funct. Mater.* **2017**, *27*, 1606735.
[206] N. Teichert, D. Kucza, O. Yildirim, E. Yuzuak, I. Dincer, A. Behler, B. Weise, L. Helmich, A. Boehnke, S. Klimova, A. Waske, Y. Elerman, A. Hütten, *Phys. Rev. B* **2015**, *91*, 184405.
[207] R. Niemann, *Nukleation und Wachstum des adaptiven Martensits in epitaktischen Schichten der Form-gedächtnislegierung Ni–Mn–Ga*, Ph.D. thesis, Technical University of Dresden (Germany), **2015**.
[208] T. Krenke, X. Moya, S. Aksoy, M. Acet, P. Entel, L. Mañosa, A. Planes, Y. Elerman, A. Yücel, E. Wassermann, *J. Magn. Magn. Mater.* **2007**, *310*, 2788.
[209] J. Liu, M. Krautz, K. P. Skokov, T. G. Woodcock, O. Gutfleisch, *Acta Mater.* **2011**, *59*, 3602.
[210] D. T. Cam Thanh, E. Brück, O. Tegus, J. C. P. Klaasse, T. J. Gortenmulder, K. H. J. Buschow, *J. Appl. Phys.* **2006**, *99*, 08Q107.
[211] A. Diestel, R. Niemann, B. Schleicher, S. Schwabe, L. Schultz, S. Fähler, *J. Appl. Phys.* **2015**, *118*, 023908.
[212] B. Li, W. J. Ren, Q. Zhang, X. K. Lv, X. G. Liu, H. Meng, J. Li, D. Li, Z. D. Zhang, *Appl. Phys. Lett.* **2009**, *95*, 172506.
[213] A. Waske, L. Giebeler, B. Weise, A. Funk, M. Hinterstein, M. Herklotz, K. Skokov, S. Fähler, O. Gutfleisch, J. Eckert, *Phys. Status Solidi RRL* **2015**, *9*, 136.
[214] N. H. Dung, L. Zhang, Z. Q. Ou, E. Brück, *Scripta Mater.* **2012**, *67*, 975.
[215] N. H. Dung, L. Zhang, Z. Q. Ou, L. Zhao, L. van Eijck, A. M. Mulders, M. Avdeev, E. Suard, N. H. van Dijk, E. Brück, *Phys. Rev. B* **2012**, *86*, 045134.
[216] B. Yu, M. Liu, P. W. Egolf, A. Kitanovski, *Int. J. Refrig.* **2010**, *33*, 1029.
[217] J. A. Lozano, K. Engelbrecht, C. R. H. Bahl, K. K. Nielsen, J. R. Barbosa, A. T. Prata, N. Pryds, *Int. J. Refrig.* **2014**, *37*, 92.
[218] S. Yu. Dan′kov, A. M. Tishin, V. K. Pecharsky, K. A. Gschneidner, Jr., *Rev. Sci. Instrum.* **1997**, *68*, 2432.
[219] F. Casanova, A. Labarta, X. Batlle, E. Vives, J. Marcos, L. Mañosa, A. Planes, *Eur. Phys. J. B* **2004**, *40*, 427.
[220] Ö. Çakır, M. Acet, M. Farle, A. Senyshyn, *J. Appl. Phys.* **2014**, *115*, 043913.
[221] H. Ossmer, C. Chluba, M. Gueltig, E. Quandt, M. Kohl, *Shape Mem. Superelasticity* **2015**, *1*, 142.
[222] M. Ghorbani Zavareh, C. Salazar Meja, A. K. Nayak, Y. Skourski, J. Wosnitza, C. Felser, M. Nicklas, *Appl. Phys. Lett.* **2015**, *106*, 071904.
[223] M. Ghorbani Zavareh, Y. Skourski, K. P. Skokov, D. Yu. Karpenkov, L. Zvyagina, A. Waske, D. Haskel, M. Zhernenkov, J. Wosnitza, O. Gutfleisch, *Phys. Rev. Appl.* **2017**, *8*, 014037.
[224] S. M. Benford, V. G. Brown, *J. Appl. Phys.* **1981**, *52*, 2110.
[225] F. Canepa, S. Cirafici, M. Napoletano, C. Ciccarelli, C. Belfortini, *Solid State Commun.* **2005**, *133*, 241.
[226] G. Porcari, M. Buzzi, F. Cugini, R. Pellicelli, C. Pernechele, L. Caron, E. Brück, M. Solzi, *Rev. Sci. Instrum.* **2013**, *84*, 073907.
[227] T. Gottschall, K. P. Skokov, F. Scheibel, M. Acet, M. Ghorbani Zavareh, Y. Skourski, J. Wosnitza, M. Farle, O. Gutfleisch, *Phys. Rev. Appl.* **2016**, *5*, 024013.
[228] X. Xu, T. Kihara, M. Tokunaga, A. Matsuo, W. Ito, R. Y. Umetsu, K. Kindo, R. Kainuma, *Appl. Phys. Lett.* **2013**, *103*, 122406.
[229] A. Kitanovski, P. W. Egolf, *Int. J. Refrig.* **2010**, *33*, 449.
[230] L. Morellon, Z. Arnold, C. Magen, C. Ritter, O. Prokhnenko, Y. Skorokhod, P. A. Algarabel, M. R. Ibarra, J. Kamarad, *Phys. Rev. Lett.* **2004**, *93*, 137201.
[231] K. Morrison, J. D. Moore, K. G. Sandeman, A. D. Caplin, L. F. Cohen, *Phys. Rev. B* **2009**, *79*, 134408.
[232] V. Franco, J. Y. Law, A. Conde, v. Brabänder, D. Y. Karpenkov, I. Radulov, K. P. Skokov, O. Gutfleisch, *J. Phys. D* **2017**, *50*, 414004.
[233] T. Kaneko, T. Kanomata, K. Shirakawa, *J. Phys. Soc. Jpn.* **1987**, *56*, 4047.
[234] K. Kamishima, M. I. Bartashevich, T. Goto, M. Kikuchi, T. Kanomata, *J. Phys. Soc. Jpn.* **1998**, *67*, 1748.
[235] A. Çakır, M. Acet, M. Farle, *Sci. Rep.* **2016**, *6*, 28931.
[236] T. Krenke, A. Çakır, F. Scheibel, M. Acet, M. Farle, *J. Appl. Phys.* **2016**, *120*, 243904.
[237] F. Scheibel, D. Spoddig, R. Meckenstock, T. Gottschall, A. Çakır, T. Krenke, M. Farle, O. Gutfleisch, M. Acet, *Appl. Phys. Lett.* **2017**, *110*, 192406.

Manuscript received: March 28, 2018
Revised manuscript received: June 8, 2018
Accepted manuscript online: June 14, 2018
Version of record online: August 13, 2018

